EXPERIMENTS ON TURBULENT MIXING AND CHEMICAL REACTIONS IN A LIQUID MIXING LAYER

Thesis by
Manoochehr Mohseni Koochesfahani

In Partial Fulfillment
of the Requirements for the Degree of
Doctor of Philosophy

California Institute of Technology
Pasadena, California

1984
(Submitted November 7, 1983)

© 1983

Manoochehr Mohseni Koochesfahani

All Rights Reserved

Dedicated to my parents,

Akhtar and Yousef Mohseni Koochesfahani

تقدیم به پدر و مادر عزیزم

یوسف و اختر محسنی کوچصفهانی

ACKNOWLEDGEMENTS

I am grateful to my advisor Professor Paul Dimotakis for years of inspiration, advice, patience and above all for being a friend. Also I would like to thank Mr. Rick Roberts for his competent teamwork in running the experiments and numerous productive discussions. My thanks go to Mr. Dan Lang who was always there to help. Many a time his electronics genius brought dead equipment back to life. I would like to extend my appreciation to the whole GALCIT family for supporting me throughout the project. Particularly, I thank Mrs. Linda Malaby for assistance in preparing the figures, Mrs. Betty Wood for her draftsmanship and Mr. Harry Hamaguchi for his photographic expertise. The financial support by the California Institute of Technology is gratefully acknowledged. This research was sponsored by AFOSR Contract Nos. F44620-76-C-0046, F49620-79-C-0159 and Grant No. AFOSR-83-0213.

ABSTRACT

The processes of entrainment and mixing are investigated in reacting and non-reacting, uniform density, liquid mixing layers over a wide range of Reynolds numbers. In non-reacting cases, a passive scalar technique is used to measure the probability density function (*pdf*) of the composition field. Chemically reacting experiments employ a diffusion-limited acid-base reaction to directly measure the extent of mixing. The diagnostics are based entirely on the laser induced fluorescence technique. The fluorescence signal is measured by self-scanning linear photodiode arrays using high speed, real-time computer data acquisition. The system is capable of yielding species concentration data with a spatial resolution of $100\,\mu m$ and a temporal resolution of $0.8\,msec$.

Results show that the vortical structures in the mixing layer initially roll up with a large excess of high speed fluid in the cores. During the mixing transition, not only does the *amount* of mixed fluid increase, but the *composition* also changes. It is found that the *pdf* of the mixed fluid, above the mixing transition, is quite uniform across the entire transverse extent of the layer. Furthermore, it is asymmetric and biased toward the high speed fluid. Experimental evidence indicates that the turbulent transport, in the cases studied, is dominated by large scale structures and is not adequately described by standard gradient-diffusion models. The fluid composition in the mixing layer, suggested by the present results, is in qualitative agreement with many aspects of the recent theoretical model of Broadwell and Breidenthal. The amount of product formed in the layer is compared to Mungal's measurements in gas, and, it is observed that the liquid layer has about 50% less product. The mean concentration of the mixed fluid, for a mixing layer at a velocity ratio of 0.38, becomes constant at

0.57 above the mixing transition. This corresponds to an entrainment ratio of 1.32, in agreement with the gaseous result of Konrad at the same velocity ratio.

TABLE OF CONTENTS

LIST OF FIGURES

LIST OF SYMBOLS

Symbol	Description
A	reactant
B	reactant
C_{1_o}	free stream molar concentration of high speed reactant
C_{2_o}	free stream molar concentration of low speed reactant
C_d	dye concentration
C_{d_o}	free stream dye concentration
C_E	$\frac{E}{1+E}$
C_m	average mixed fluid concentration, equations (D.6) & (D.18)
C_M	total mean mixed fluid concentration, equations (D.8) & (D.19)
C_p	product concentration, equation (D.14)
$\overline{C_p}$	average product concentration, equation (D.15)
C_{p_s}	stoichiometric product concentration, equation (D.13)
D	mass diffusion coefficient
D	dark response, equation (C.1)
E	entrainment ratio
g	gravitational acceleration
I	laser intensity
I_f	fluorescence intensity
I_o	laser intensity in the absence of attenuation, equation (C.2)
k	chemical reaction rate constant, Appendix A
n	number of dye molecules, § A.4
n_o	number of dye molecules at $t = 0$, § A.4
n_A	moles of reactant A in the sampling volume

n_B	moles of reactant B in the sampling volume
p	probability density function, equation (D.2)
$\bar{p}$	average *pdf*, equation (D.7)
P	product
P	total mixed fluid probability, equations (D.5) & (D.17)
Q	quantum yield, equation (A.1)
Q_b	bleaching quantum efficiency, § A.4
r	velocity ratio, U_2/U_1
R	pixel sensitivity, equation (C.1)
Ri	Richardson number, $\frac{\Delta\rho\, g\, \delta}{\bar{\rho}\,(\Delta U)^2}$, Appendix A
Re_δ	Reynolds number, $\Delta U\ \delta/\nu$
Re_{δ_1}	Reynolds number, $\Delta U\ \delta_1/\nu$
$\mathrm{Re}_{\delta_{vis}}$	Reynolds number, $\Delta U\ \delta_{vis}/\nu$
s	density ratio, ρ_2/ρ_1
Sc	Schmidt number, ν/D
t	time
T_s	array scan time, equation (C.1)
U_1	high speed free stream velocity, Figure 1
U_2	low speed free stream velocity, Figure 1
v_1	volume of H.S. fluid in the sampling volume
v_2	volume of L.S. fluid in the sampling volume
v_a	volume of acid solution in the sampling volume
v_b	volume of base solution in the sampling volume
V	output voltage, equation (C.1)
x	streamwise coordinate, Figure 1
x_o	virtual origin
y	transverse coordinate, Figure 1

z	spanwise coordinate
β	parameter, equation (C.3)
δ	shear layer vorticity thickness, equation (4.2b)
δ_1	shear layer 1% thickness, Chapters 4 & 5
δ_{vis}	shear layer visual thickness, equation (4.2a)
δ_{p_1}	product thickness, equation (D.16a)
δ_{p_2}	product thickness, equation (D.16b)
Δx	resolution in the flow direction, § B.1.2
Δy	resolution in the transverse direction, § B.1.2
Δz	resolution in the spanwise direction, § B.1.2
$\Delta\rho$	density difference, $\rho_1 - \rho_2$
ΔU	velocity difference, $U_1 - U_2$
ε	small number, Appendix D
ε_o	dye molar absorption coefficient, equation (A.1)
η	optics collection efficiency, equation (C.1)
λ_D	diffusion scale, equation (4.5) and § A.3
λ_ν	viscous (Kolmogorov) scale, § A.3
ν	kinematic viscosity
ξ	H.S. fluid volume fraction, equation (D.1)
ξ_s	stoichiometric concentration, equation (D.12)
ρ_1	high speed side density
ρ_2	low speed side density
$\bar{\rho}$	average density, $(\rho_1 + \rho_2)/2$
σ	dye absorption cross section, § A.4
τ_b	photobleaching time constant, § A.4
τ_{chem}	chemical time, § A.3
τ_δ	large scale mixing time, § A.4

τ_{λ_D}	time to diffuse across diffusion scale, § A.4
τ_{λ_ν}	time to diffuse across viscous scale, § A.4
φ	equivalence ratio, C_{2_0}/C_{1_0}, equation (D.10)
Φ	laser photon flux, § A.4
Ω	solid angle, equation (C.1)
Ω	vorticity, Figure 17

pdf, PDF	probability density function
H.S.	high speed
L.S.	low speed
[ ]	molar concentration, Appendix A

Chapter 1

INTRODUCTION

1.1. Background

Understanding chemically reacting turbulent flows is of importance in a variety of engineering and technological applications. For non-premixed reactants in the limit of fast chemistry, the chemical reaction rate is diffusion limited and, therefore, the chemical production rate cannot exceed the rate of mixing of the reactants (Burke & Schumann 1928 and Hawthorne et al. 1949). It is in this context that understanding the mechanisms governing turbulent transport and mixing becomes an important issue.

An important approach to the solution of chemically reacting flows has been formulated in terms of the probability density function (*pdf*) of a passive scalar (or contaminant) in the non-reacting flow. This has been the result of the work of Toor (1962) who first related the behavior of the reacting system, under certain conditions, to that of the non-reacting case. The prediction of the *pdf*s from fundamental principles has met with various degrees of success, however.

Virtually all the classical turbulent theories model turbulent transport of a passive contaminant by linear mean gradient models and usually incorporate an ad hoc estimate of the proportionality coefficient, the eddy diffusivity (Sreenivasan et al. 1981). With the discovery of large structures in various shear flows of interest, the applicability of these models to such flows has been questioned. Recent studies by Walker (1979) and Sreenivasan et al. (1981), in comparing the predictions of different turbulent mixing models with experimental results, have concluded that the dominance of the large structures in the transport process

is an essential element that is missing in the models.

A recent attempt that does not employ the concept of gradient diffusion has been the model of Broadwell & Breidenthal (1982) for mixing and chemical reaction in a turbulent shear layer. They idealize the fluid states in the mixing layer to be in one of three states : (i) unmixed, (ii) a homogeneous mixture at the entrainment ratio, and (iii) in strained laminar diffusion layers between the free stream fluids. Furthermore, their model provides a formalism which can address the results for gases and liquids (i.e. fluids of differing Schmidt number) by a single theory. Schmidt number $Sc = \nu/D$ is the ratio of the diffusion coefficient of momentum to that of mass. Similar ideas have been later proposed, in terms of a model for the *pdf* of a passive scalar, by Effelsberg & Peters (1983). At this stage, there is need for quantitative experimental verification of the new models especially as regards the mechanisms of turbulent mixing. Reliable measurements of the fluid composition in turbulent flows are necessary to provide guidance for more sophisticated theoretical models.

The two-dimensional turbulent shear layer between two streams of different velocities, see Figure 1, has played an important role in understanding of turbulent shear flows in general. It is one of the simpler turbulent flows and is well documented. The study of mixing in this flow which is a more recent focus of attention has, however, been mostly directed toward the gaseous phase. Some of the contributions in this area, in both reacting and non-reacting cases, are represented by the work of Brown & Roshko (1974), Fiedler (1975), Konrad (1976), Batt (1977), Wallace (1981) and Mungal (1983). Of particular interest is the experiment of Konrad who measured the *pdf* of one of the mixing species in a non-reacting gaseous layer using the passive scalar technique. His results provided an upper bound for the amount of chemical product for a low Schmidt number fluid (gas $Sc \approx 0.7$). Recent measurements of Mungal, in a chemically

reacting layer, gave a direct estimate of the amount of chemical product.

Studies of mixing in liquid mixing layers are few. Dimotakis & Brown (1976) qualitatively studied the mixing process in a very high Reynolds number flow. Breidenthal (1978) made the first quantitative measurement of the extent of mixing and the total amount of chemical product using an attenuation technique in a chemically reacting layer. Comparison of his findings with the results of Konrad, and later Mungal, showed that the amount of product in a liquid (in this case water, $Sc \approx 600$) is less than in a gas. This effect of Schmidt number on the amount of mixing, not accounted for in the standard turbulent mixing models, is included in the Broadwell- Breidenthal model. Breidenthal's results provided information on the integrated amount of mixing and product in the liquid layer. Quantitative measurements of the fluid composition and the chemical product distribution have not been available. Such information would find special significance in light of the Broadwell-Breidenthal model and would also be expected to increase the present understanding of the processes of turbulent transport and mixing.

The present effort is a continuation of Breidenthal's work and is aimed at a detailed quantitative study of entrainment and mixing in a liquid shear layer. The primary objective is to measure the *pdf* of the composition field over a range of Reynolds numbers covering the extent of the mixing transition. This is done using a passive scalar technique in a non-reacting layer (dilution experiments) and is equivalent to Konrad's experiment for a liquid. The dilution measurements are complemented by chemically reacting experiments which, besides serving as the testing ground for the ideas developed based on the non-reacting results, allow the direct determination of the extent of mixing. These measurements would be the equivalent of Mungal's experiment for a liquid. The merits of the passive scalar and chemical reaction techniques will be discussed later in

this chapter. The diagnostics are based entirely on laser induced fluorescence (LIF). The fluorescence signal is measured by self-scanning linear photodiode arrays using high speed, real-time computer data acquisition. A summary of previous work using LIF is presented in the next section. The details of this technique are given in Appendix A.

1.2. Laser Induced Fluorescence (LIF)

The LIF technique has proven to be a very powerful tool in the study of mixing and reacting flows. It is non-intrusive and capable of yielding detailed quantitative, time and space resolved, measurements of species concentration with temporal and spatial resolution not achievable by conventional means. Its development at GALCIT, by P.E. Dimotakis, has been directed mainly toward reacting and non-reacting liquid phase flows.

Non-reacting flow applications generally employ premixing of a fluorescent organic dye with one of the mixing species which then becomes visible, in a spatially-controlled manner, by a laser illuminated field (point, line or sheet). Recording the fluorescence intensity allows a quantitative measurement of the concentration of the mixing species, labeled by the dye, in the field of illumination since the fluorescence intensity is linearly proportional to the dye concentration (Appendix A). Reacting flows use dyes whose fluorescence can be suppressed or induced by a particular chemical environment. Fluorescein, whose fluorescence is pH sensitive, has often been used in our laboratory (Appendix A). Note that since the fluorescence behavior of this dye depends on its local chemical environment, mixing can be monitored down to the molecular scale.

Most of the available LIF data are of two types. Some have used sheet illumination and recorded the fluorescence on photographic film. These include

works of Dewey (1976), Liu et al. (1977), Bernal (1981), Dimotakis et al. (1982, 1983) and Koochesfahani et al. (1983). Others have used point illumination and recorded the fluorescence intensity by a photomultiplier tube (Robben et al. 1976, Dewey 1976 and Liu et al. 1977). Whereas point measurements have offered quantitative results, they are not as useful as field measurements in the flows dominated by large scale patterns. Even though it is certainly possible to calibrate the photographic film as a quantitative recording medium, problems of response nonlinearity, emulsion nonuniformity and reproducibility of a difficult calibration procedure have limited its usage.

The alternative is provided by electronic, self-scanning, linear or 2-D image arrays which allow the photographic film to be by-passed altogether. A first step in this direction was the work of Dimotakis et al. (1982) who used line illumination and recorded the fluorescence data by a linear self-scanning photodiode array. The output of the array was used to modulate an oscilloscope beam driven synchronously in a raster scan fashion to produce an $x-t$ diagram. Kychakoff et al. (1983) have recently reported single-frame results of sheet illumination. They detected the LIF signal using an image-intensified 2-D photodiode array camera (100 x 100 elements). Their multiple-frame capability, however, was limited to 26 frames of data.

In the present study, both line and sheet illumination were used. Sheet illumination data were recorded photographically. Line illumination data were recorded using a linear photodiode array. In this manner, real time, digital concentration data were measured across the field of illumination with a spatial resolution of $100\,\mu m$ and a temporal resolution of $0.8\,msec$. The computer-based data acquisition system was capable of acquiring multi-frame data. For example, when recording 64 out of 512 pixels per frame, 38,400 consecutive frames at 1,250 frames/sec were routinely acquired.

1.3. Passive Scalar vs Chemical Reactions

It was pointed out by Breidenthal (1978) that the passive scalar technique always yields an upper bound to the actual molecular mixing. In using this technique (also referred to as dilution in this work), a passive scalar contaminant, such as dye, is premixed with one of the streams. The concentration of dye within a small sampling volume, determined by the resolution characteristics of the measuring apparatus, is then recorded as a function of time. The difficulty arises if the sampling volume is larger than the smallest mixing scales, as is usually the case. As Figure 2 illustrates, within the resolution of the measurement device, it is impossible to determine whether the two fluids are mixed or not. Breidenthal further points out that the problem of the finite probe sampling volume can be solved by using a fast and irreversible chemical reaction of the type $A + B \rightarrow P$. If dilute reactant A is added to one stream and B to the other, then the amount of product formed is equal to the amount of molecular scale mixing between the two streams at the reaction equivalence ratio.

With all the drawbacks associated with the passive scalar method in determining the true extent of molecular mixing, it nevertheless is the fastest way to get an estimate of the composition field (i.e. the *pdf*). A dilution measurement, in one single experiment, yields information about mixing at all mixture ratios. It is certainly possible to determine the *pdf* from chemically reacting data with much better accuracy in representing true mixing (see Wallace 1981), but that would require many experiments at different reaction equivalence ratios. In view of this discussion, dilution was used to estimate the *pdf*s. Chemically reacting measurements were also conducted, however, to insure the integrity of the conclusions reached on the basis of the dilution data.

Chapter 2

EXPERIMENTAL FACILITY AND INSTRUMENTATION

Three sets of experiments were performed in two shear layer facilities. The first set was qualitative in nature and is here referred to as the " sheet illumination " experiment. The last two sets were detailed and quantitative and are here named the " line illumination " experiments. The apparatus used for each set of experiments and the corresponding instrumentation and data acquisition are described below.

2.1. Sheet Illumination

This experiment was aimed to study some implications of the entrainment asymmetry in a chemically reacting mixing layer. A small short flow time setup was used to observe the fluorescing chemical product in a region of the flow illuminated by a laser sheet.

2.1.1. *Shear Layer Apparatus.* The shear layer was produced in a small blow-down facility, in which the chemical composition of each of the two free streams could be prepared to any concentration. This apparatus is the result of the work of many people with the latest modifications incorporated by P. E. Dimotakis and the author. A gaseous nitrogen supply system, regulated through separate sonic orifice metering valves, maintained the free stream flow velocities nearly constant. Transients and possible U-tube oscillations were minimized by placing two large vessels in the gas supply route. The effective capacitance of these vessels in conjunction with the resistance in the supply tube allowed for adequate damping of the whole system (see Figure 3). Free stream velocities were determined by measuring the rate of drop of free

surfaces of the two reservoirs. Dimensions of the test section were 3.5 cm in width and 23.5 cm in span.

2.1.2. *Optical Setup & Data Acquisition.* The schematic of the optical setup is shown on Figure 4. A 3 W argon ion laser (Coherent Radiation $CR-3$) beam was passed through a combination of spherical and cylindrical lenses to produce a sheet, about 1 mm in thickness, illuminating a portion of the test section. All lines of the laser were used in this experiment. A motor driven 35 mm camera was used to photograph the resulting fluorescent chemical product on normally developed Kodak $TRI-X$ film.

2.1.3. *Free Stream Fluid Preparation.* The base solution was prepared by adding concentrated sodium hydroxide ($NaOH$) of technical grade to soft water and the acid solution by adding pure sulfuric acid (H_2SO_4) to water. Fluorescein dye was added to the acid to a concentration of about 25×10^{-7} M and both solutions were thoroughly mixed. For these experiments the concentrations of the acid and base solutions were selected in such a way so as to require 1.8 part (in volume) of the basic solution to titrate one part of the acid solution and cross the threshold for fluorescence (see Appendix A for a sample titration curve). This ratio was checked visually. The fluorescence *on/off* transition was very sharp in this case and was of the order of one part per mil, based on the mixture volume ratio (Koochesfahani et al. 1983).

2.2. Line Illumination; Dilution

This experiment forms the major portion of this work. It was aimed at measuring the concentration field and its probability density function (*pdf*). The flow time required to collect sufficient amount of data for reliable statistics was longer than that offered by the small facility used in § 2.1. Breidenthal's shear layer apparatus was found suitable for this purpose and was used instead.

2.2.1. *Shear Layer Apparatus.* Experiments were conducted in the water mixing layer facility designed by Breidenthal (1978). It is a gravity driven apparatus in which the free stream fluids are supplied from two independent reservoirs. A schematic of this apparatus is shown on Figure 5. Desired flow speeds were achieved by adjusting the throttling valves and test section free stream velocities were calculated from total and static pressure measurements as described by Breidenthal (1978).

2.2.2. *Optical Setup.* The beam of a 3 W argon ion laser (Coherent Radiation $CR-3$) was passed through a converging lens to produce a thin beam (diameter in the range 0.5 to 1 mm) coincident with the transverse direction of the mixing layer at the mid-span position. Variations of the beam diameter along the 7 cm width of the test section were minimized by using a long focal length lens. The schematic of the optical arrangement is shown on Figure 6. The titration-reference chamber on this figure was a necessary addition for the chemically reacting runs and was not used in dilution experiments.

The fluorescence intensity along the beam was measured by a 1024 element linear photodiode array (Reticon, $RL-1024G$). Characteristics of this array are described in Appendix B. The array and its supporting electronics were configured in such a manner as to allow their usage similar to an ordinary camera, with the exception that the photographic film in the film plane was replaced by the photodiode array (see Figure 7). This configuration was originally designed and built by R. Miake-Lye (Dimotakis et al. 1982) with subsequent refinements incorporated by the author in collaboration with D. Lang.

High temporal and spatial resolution require fast scanning rates of the array at low magnification ratios, whereas to image the entire width of the layer with sufficient output signal level asks for higher magnification ratios and slower scan rates. To satisfy these conflicting requirements, a magnification ratio of

about 1/4 was used for which only half of the array was needed to view the visual width of the layer. The array was short cycled to operate as a 512 element array, thereby also increasing the scan rate by a factor of 2.

A Nikon lens (f/1.2, 50 mm $f.l.$) was chosen as the imaging lens. This choice was dictated by the need to maximize the amount of collected light. At the low conjugate ratio of 1/4, however, severe image nonuniformity was observed since this lens is optimized for infinite conjugate ratio. The image could not be focused uniformly all across the array. This problem was solved by placing in front of the Nikon lens a copy lens (Bausch & Lomb f/4.5, 209 mm $f.l.$), matched to the Nikon to give the required magnification ratio, such that both lenses were working at near infinite conjugate ratio in the modified arrangement. This lens combination resulted also in a slight increase in the amount of light collected and was used in all the dilution experiments. The actual magnification ratio in these experiments turned out to be 1/3.9 resulting in a spatial resolution of about 100 μm × 100 μm (see Appendix B for a short discussion on resolution).

Even though the reservoir fluids were filtered, scattering of the laser light, mainly at 4880 and 5145 Å, by unwanted particles was observed. This could potentially cause erroneous results, because software identification and removal of scattering signal from fluorescence data are not particularly easy. Using an orange photographic filter (Hoya No.15) effectively blocked any scattered light below 5200 Å.

2.2.3. *Data Acquisition.* Data acquisition support was provided by the HYDRA-1 computer of the HYDRA system which was designed and configured by P. E. Dimotakis and D. B. Lang. HYDRA-1 is based on a PDP-11/23 CPU with a Floating Point Accelerator, 1/4 *Mbyte* of main memory and 80 *Mbytes* of high speed (1 *Mbyte/sec*, Winchester) disk storage. It is also equipped with a variety

of multi-channel input/output devices for data acquisition and control purposes. Reticon array data were acquired by the ADC board which is a single channel A/D system capable of performing 8-bit conversions at a rate of 10^7 conversions/sec. A more detailed description of this device can be found in Appendix B.

The array was clocked at 640 *KHz* corresponding to a scan time (or temporal resolution) of 800 μsec, or a scan rate of 1250 scans/sec. Only one case was run at 8 *msec* scan time (64 *KHz* clock) to investigate the effects of poor temporal resolution. Sharing the computer bus cycle time between the ADC board and the disc controller allowed a maximum data rate of 150 *Kbytes/sec* at the time these experiments were being performed. This rate was the fastest at which large amounts of data could be digitized and transferred to the disk continuously. A data record of a length equal to the system memory could, however, be acquired and transferred to memory at 1.2 *Mbytes/sec* (see Appendix B).

Slowing down the array to accommodate the maximum data rate, discussed above, would compromise the temporal resolution. We decided, instead, to digitize 1 out of every 8 pixels. This, in effect, reduced the data rate to 80 *KHz* without compromising the intended spatial and temporal resolution of each pixel. The array was clocked by a master function generator, whereas the ADC board was run by a clock obtained from the master clock by a divide by 8 circuit. With this arrangement, we could obtain large (up to the disc capacity) amounts of concentration data, continuously, at 64 points across the layer essentially simultaneously. The amount of data taken per run typically corresponded to the passage of about 100 structures or approximately 2.5×10^6 numbers (pixels). Some data were also taken at the array clocking rate which corresponded to 384 successive scans, each at 512 points across the layer, for a total of 196,608 measurements of point concentration. These, however,

corresponded to a flow time of about 300 *msec* (time to fill the system memory at 640 *KHz*) or the passage of at most a few structures. The large amounts of data generated by this technique were stored on hard disc and magnetic tape for further processing.

2.2.4. *Free Stream Fluid Preparation.* Preparing the free streams was quite easy in these experiments since there was no chemistry involved. The low speed free stream fluid was prepared by adding fluorescein dye to water to a concentration of about 5×10^{-7} *M*, whereas the high speed free stream was pure water. Both solutions were run through a filter for about an hour to remove any scattering particles.

2.3. Line Illumination; Chemical Reaction

This experiment was performed to measure space and time resolved product concentration in a chemically reacting shear layer in order to examine some of the ideas developed based on the dilution results.

2.3.1. *Shear Layer Apparatus.* Breidenthal's facility was used for this work also. The apparatus was modified by R. Roberts to include a titration-reference chamber (see Figure 6). Whereas the reference dye concentration in the dilution experiments was available from the low speed free stream, no such information could easily be obtained from within the layer in the chemically reacting case. The reference information was provided in the titration-reference chamber, which contained, for each run, the titrated acid-base solution corresponding to the maximum possible product concentration for that run (see Appendices A, C and D).

The free stream velocities were measured by a single channel laser Doppler velocimeter (LDV). The LDV apparatus was built and operated by R. Roberts.

2.3.2. *Optical Setup & Data Acquisition.* Optical and data acquisition arrangements were essentially the same as that described in § 2.2 with some minor differences. A Lexel (model 95) ion laser was used at the single 5145 Å line (2 W maximum power). A single Macro lens (Vivitar, $f/2.8$, $90\,mm$ $f.l.$) imaged the test section and the titration-reference chamber onto the 1024 element Reticon array, all of which was utilized for these experiments. The image ratio was measured to be 1/3.68, which corresponded to a spatial resolution of approximately $90\,\mu m \times 90\,\mu m$.

The array was clocked at $512\,KHz$ corresponding to a scan time (or temporal resolution) of $2\,msec$. With the technique described earlier, 1 out of every 4 pixels were digitized to put the effective data rate well within the maximum for continuous recording which, by this time, had reached 300 $Kbytes/sec$. This arrangement allowed us to record large (as limited by the disc's capacity) amounts of product concentration data, continuously, at 256 points across the layer simultaneously. The amount of data taken for each run corresponded, as before, to the passage of roughly 100 structures.

2.3.3. *Free Stream Fluid Preparation.* The free streams were prepared in essentially the same manner as that described in § 2.1.3. The highest dye concentration used was $10^{-5}\,M$. The equivalence ratio for fluorescence "turn-on" was determined by measuring the titration curve of fluorescence intensity versus base mixture fraction by the Reticon array. One such curve is shown on Figure A.2 of Appendix A. The titrated solution remained in the titration-reference chamber during the course of the run and provided the reference product concentration. Densities of the two sides were matched, when necessary, by adding a sufficient amount of sodium sulfate (Na_2SO_4) salt to the acid/dye solution (see § A.3.1).

Chapter 3

CHEMICALLY REACTING EXPERIMENTS ; SHEET ILLUMINATION

Work of Konrad (1976), in a gaseous mixing layer, suggests that the entrainment into the layer is asymmetric in favor of the high speed fluid. The experiment decribed in this section was designed to explore the implications of the entrainment asymmetry and to monitor the chemical environment, on a molecular scale, of the mixing fluids in a liquid mixing layer. Results discussed here have been presented elsewhere (Koochesfahani et al. 1983).

3.1. Experimental Conditions

The free stream velocities were set with $U_1 = 42\ cm/sec$ on the high speed side, and a low speed side corresponding to a velocity ratio $U_2/U_1 = 0.45$. Concentrations of the acid and base solutions in the free streams were such that it required mixing 1.8 volumes of base to 1 volume of acid to reach and cross the fluorescence threshold. Two sets of runs were made under identical flow conditions and optical setup. In the first set, the acid solution was placed on the high speed side with the base on the low speed side. For the second set, the chemicals were reversed. Typical results are shown on Figure 8. The visible portion of the apparatus in the photographs corresponds to a downstream region of $10.5\ cm < x < 22.5\ cm$, as measured from the tip of the shear layer splitter plate, and a Reynolds number range of $2130 \lesssim Re_{\delta_{vis}} \lesssim 6100$, based on the velocity difference and the local visual thickness.

3.2. Results and Discussion

Figure 8 shows the regions of mixing and chemical reaction in a thin slice at the mid-span of the shear layer. The fading of the fluorescence intensity toward the left and right edges of the photographs is due to the gaussian distribution of intensity in the laser sheet. With the base on the high speed side (Figure 8b), the equivalence ratio of the experiment is $\varphi = 1.8$ and any fluid that is mixed to a high speed fluid volume fraction of $\xi > \varphi/(1+\varphi) = 0.64$ is visible through its fluorescence (see § D.2.1 and Figure D.3). When the base is on the low speed side (Figure 8a), $\varphi = 1/1.8$ and the mixed fluid in the range $\xi < 0.36$ fluoresces. It is important to keep in mind that the photographs in Figure 8 are of the same flow. One conclusion can readily be made. There is a much higher probability of finding mixed fluid of $\xi > 0.64$ than $\xi < 0.36$. The composition of the mixed fluid, at this Reynolds number, is asymmetric and strongly biased toward the high speed fluid.

It is also instructive to examine Figure 8 in terms of the chemical product. Note that the reaction product is found in regions associated with the large vortical structures in agreement with the observations of Dimotakis & Brown (1976), Breidenthal (1978, 1981) and Mungal (1983). Furthermore, there does not seem to be any significant systematic variation of the fluorescence intensity across the width of the mixing layer in Figure 8b, implying that the mixed fluid composition could be fairly uniform.

Based on the properties of the TRI-X film (approximately 2 decades of latitude for normal development), the amount of chemical product, defined here operationally as the fraction of the fluid whose pH is in excess of the fluorescence threshold, can be estimated. The difference in the amount of product between the two cases is of the order of two orders of magnitude. It should be kept in mind, however, that this is not the amount of product in the usual sense

because only the product corresponding to the mixed fluid in a selected range of compositions has been examined. Similar results have been obtained by R. Roberts in the Breidenthal facility under comparable conditions using phenolphthalein as pH indicator (private communication). The result that the amount of chemical product, in the same flow, depends on which side the reactants are placed (corresponding to runs at φ and $1/\varphi$) is a direct consequence of the asymmetry of the mixed fluid composition. This effect has also been observed by Mungal (1983) in his chemically reacting gaseous mixing layer.

The results can be understood in part in terms of a simple mixing model proposed by Broadwell & Breidenthal (1982). According to this model, the shear layer entrains a certain ratio of high speed fluid to low speed fluid. The entrained fluid from the two sides of the shear layer mixes and homogenizes at a composition corresponding to this entrainment ratio. In addition, there are contributions from the strained 'flame sheets' between the two fluids, which in the case of liquids (high Schmidt number), would be small. Present results agree with these ideas to the extent that the mixed fluid composition is asymmetric in favor of the high speed fluid as Konrad's entrainment result would suggest, and that the reaction occurs more or less uniformly across the shear layer. The photographic evidence presented here, however, implies a much higher degree of asymmetry than that supported by the *pdf* data of Konrad and his entrainment ratio value of 1.3 for a gaseous mixing layer at a velocity ratio of 0.38. The reasons for this will be made clear in the next chapter, but for now, it suffices to say that at low Reynolds numbers the composition of the mixed fluid is affected also by the initial conditions at roll-up and not determined solely by the entrainment ratio.

It should be pointed out that the results presented above cannot be explained by a gradient diffusion model of turbulent transport. Note, for example, that

the reaction zone is not driven from one side of the layer to the other by the change in φ from 1.8 to 1/1.8, as would be expected from such a model (Broadwell & Breidenthal 1982, Koochesfahani et al. 1983).

An experiment of the type described in this chapter which employs switching of the sides of the reactants to achieve equivalence ratios of φ and $1/\varphi$ in the same flow is referred to as a " flip " experiment hereafter in this work.

Chapter 4

DILUTION EXPERIMENTS ; LINE ILLUMINATION

This chapter describes an experimental study of the concentration field in a constant density, aqueous plane mixing layer. All measurements were carried out at a velocity ratio of $r = U_2/U_1 = 0.38$ except for the test case in § 4.1. The fluorescent dye, which was premixed with the low speed free stream fluid and diluted by mixing with the high speed fluid, was used to monitor the relative concentration of high speed to low speed fluid in the layer. No chemistry was involved and the dye acted as a passive scalar. The fluorescence intensity was measured along a laser beam, extending across the width of the shear layer, using a 512 element linear photodiode array. The data reduction steps to calculate the normalized concentration of the high speed fluid, ξ, from fluorescence intensity data are discussed in Appendix C.

The resolution area in each case will be given in the form $\Delta x \times \Delta y$. Δx is the *effective* resolution in the flow direction and is the sum of the static resolution ($100\,\mu m$) and the distance the flow moves during the scan time. The convection velocity, $U_c = (U_1 + U_2)/2$, was used as the reference velocity and the scan time was $0.8\,msec$. The resolution in the transverse direction, Δy, was fixed at $100\,\mu m$ and in the spanwise direction, Δz, was about $500\,\mu m$. See Appendix B for a discussion on resolution. Note that the actual effective resolution varies across the layer, being better on the low speed side, relative to the high speed side.

In the absence of any velocity field measurements, an alternate transverse reference length scale to the conventional vorticity thickness, δ, had to be chosen. A reference thickness, δ_1, was defined as the 1% width of the total mixed

fluid probability, $P(y)$, where P had dropped to 1% of its maximum value. Definition of P and all other statistical quantities used in this chapter are given in Appendix D and are not repeated here. The main motivation for this choice of thickness was that the two points marking the edges of δ_1 generally corresponded to locations in the layer where the probability of finding pure H.S. and L.S. fluids had reached 0.99 and this was thought to be a reasonable way of determining the visible edge of the mixing layer. As a matter of fact, in the cases where the visual thickness, δ_{vis}, of the layer could be directly measured, such as that in § 4.2, excellent agreement between δ_1 and δ_{vis} was obtained. Furthermore, in the high Reynolds number case of § 4.3, it was found that the growth rate of δ_1, $d\delta_1/dx$, agreed with that of the visual thickness, $d\delta_{vis}/dx$, as given given by Brown & Roshko (1974), to about 5%. Brown & Roshko determined a layer width, from their mean density profiles, corresponding to the distance between the points where the mean density was within 1% of the free stream values. They found that this width coincided fairly well with the layer visual thickness. In view of this discussion, δ_1 and δ_{vis} and hence Re_{δ_1} and $Re_{\delta_{vis}}$ have been used interchangeably in this study.

It should be pointed out that the location $y = 0$ is of no particular significance and was arbitrarily chosen to coincide with the point where the total probability of finding mixed fluid was at a maximum (i.e. position of maximum $P(y)$). The *pdf*s reported here are based on data records corresponding to the passage of roughly 100 structures. It is sometimes useful to represent the whole layer by an average *pdf*, $\overline{p}(\xi)$. This quantity has been calculated as an average over approximately 63% of the visual width of the layer (see equation D.7).

The experiments discussed in this chapter were performed in the Breidenthal facility over a range of Reynolds numbers covering the extent of the mixing

transition. The mixing transition, in the shear layer, is a region corresponding to the introduction of small-scale, three-dimensional motions into the layer. It was first observed by Konrad (1976) in a gas flow and later by Breidenthal (1978) in a liquid shear layer, with further work done by Bernal (1981). Breidenthal found that the amount of mixing and hence the amount of chemical product, in the case of a liquid, was very small below the mixing transition. Above the transition, mixing and the amount of chemical product increased dramatically and, furthermore, reached an asymptotic value. In the transition region between these two limits, the amount of mixing increased monotonically. The flow parameters, in the present experiments, were determined on the basis of Breidenthal's data which indicate that the region of transition, in his apparatus at a velocity ratio $r = 0.38$, is confined to a Reynolds number range of $3000 \lesssim \mathrm{Re}_{\delta} \lesssim 8000$, where the Reynolds number is based on the velocity difference and the vorticity thickness. As will be shown later (equation 4.3b), this range corresponds to $6300 \lesssim \mathrm{Re}_{\delta_1} \lesssim 17000$, where the Reynolds number is based on the velocity difference and δ_1.

4.1. A Test Case

A sample run was made at a low Reynolds number in order to evaluate the performance of the technique and data acquisition hardware and software. The data were recorded at $x = 18\ cm$ with $U_1 = 13\ cm/sec$ and $r = 0.46$. The visual thickness of the layer, δ_{vis}, was estimated to be about $25\ mm$, resulting in a Reynolds number $\mathrm{Re}_{\delta_{vis}} \approx 1{,}750$. The effective resolution area, under these conditions, was $176\ \mu m \times 100\ \mu m$.

The raw output of the array for a single scan is shown on Figure 9. This is how the array output would look if it were displayed on an oscilloscope, with each step in the drawing corresponding to an individual pixel. Only 230 pixels

out of 512 are shown, as the pixels outside the range displayed were imaged on the free streams. The output is near zero in the H.S. free stream signifying the absence of any fluorescent dye there. In the L.S. free stream, however, the output is at maximum corresponding to the presence of pure dye solution. In order to see the structure of the flow, consecutive scans of the array were plotted sequentially, in reverse time sequence, and assembled into the picture in Figure 10. This picture represents 384 successive frames in 307 *msec* of flow real time.

Generating flow pictures in the form of Figure 10 is very time-consuming and cumbersome. Digital LIF data can be more readily displayed on image processing monitor screens. Two photographs recorded from such a screen (Conrac Monitor) are shown on Figure 11. Figure 11a is the same as that in Figure 10 except that 400 (out of 512) pixels across the layer are shown and pseudo-color assignment, corresponding to different H.S. fluid concentration levels, was used to assist in the interpretation of the data. It should be emphasized that, technically speaking, these are not " photographs ". The vertical extent maps onto 40 *mm* of the transverse coordinate of the shear layer. The horizontal extent is time (running backwards). The picture was constructed in the computer by transmitting to the image processor, in reverse order, consecutive scans of the array for processing and display. Flow images of the type in Figure 11 are used throughout the rest of this work instead of the more conventional plot of Figure 10. The pseudo-color assignment was standardized to the one shown in Figure 11 with red corresponding to pure L.S. fluid ($\xi = 0$), blue to pure H.S. fluid ($\xi = 1$) and the rest of the rainbow spectrum to the intermediate values of ξ. This color assignment was generated by setting the intensity transformation tables of the red, green and blue guns of the color monitor according to the diagram in Figure 12.

Figures 9, 10 and 11 show that the concentration field in this case is rather simple. It consists of only pure high speed and low speed fluids with very little mixing, if any, at the interfaces separating the two free stream fluids which, under these conditions, may be outside the resolution capabilities of our technique. This is essentially the case of the shear layer before the mixing transition, as defined by Breidenthal (1978). The large excess of high speed fluid in the core of the structures in Figure 11 is noteworthy and will be discussed in more detail in the next section.

4.2. Low Reynolds Number; before the Mixing Transition

Even though the flow images of the previous section show the essential features of the concentration field prior to the mixing transition, a more detailed study of this case was undertaken to map out the *pdf* of the flow. An explanation of the initial composition asymmetry, manifested by the large excess of high speed fluid in the structure cores, is also given.

The experiment was performed at $x = 7\ cm$ with $U_1 = 30\ cm/sec$ and $r = 0.38$. The width of the layer was measured to be $\delta_1 = 14.8\ mm$, resulting in a Reynolds number of $Re_{\delta_1} \approx 2{,}800$. The effective resolution area, under these conditions, was $266\ \mu m \times 100\ \mu m$.

Time traces of relative concentration of H.S. fluid, ξ, are shown at seven locations across the layer in Figure 13. Each time trace is composed of 500 consecutive data points connected by straight lines. The basic feature of the flow in this regime is that any given point in the layer spends most of its time in either pure H.S. or L.S. fluid. There is very little mixing and that occurs at the interfaces between pure fluids from the two sides. These interfaces are buried in the transition regions from $\xi = 0$ to 1 in the time traces. The sharpness of the transition is indicative of the ability (or lack thereof) of the measuring device to

resolve a thin moving interface. The probability density function of the concentration field at selected points in the layer is shown in Figure 14. Any value of probability higher than 25 is not shown. Note that the *pdf*, in this case, is characterized by two delta functions located at $\xi = 0$ and 1, the heights of which depend on the location in the layer, with practically no mixed fluid in between. It is clear that if this shear layer were carrying reactants in its free streams, the amount of chemical product would be very small in agreement with the measurements of Breidenthal (1978).

In order to see the underlying structure of the flow, the picture of the whole layer corresponding to the time interval of the data of Figure 13 was constructed in the manner described in the previous section (see Figure 15). Each strip corresponds to a particular y location, with the ones labeled by the white markers being the specific time traces of Figure 13. The horizontal axis, as before, is time running backwards. For reasons explained in Chapter 2, one out of every eight pixels was digitized for the data of the type described here and therefore the distance between the strips (points) is about $800\,\mu m$. The average *pdf*, $\bar{p}(\xi)$, corresponding to the whole data record is shown below the image. The height of the delta functions representing the free streams are again not drawn to scale. It can be seen that the flow consists of vortical structures at an early stage of roll-up. Previous conclusions can now be better interpreted. As before, the large excess of high speed fluid in the structure cores is quite evident. There is very little mixing and that occurs at the interfaces separating pure high and low speed fluids.

The *pdf* of the composition field across the entire layer, shown in Figure 16, was used to calculate transverse profiles of some quantities of interest (Figure 17). Attention is drawn to the probability of finding pure H.S. fluid defined by the probability of finding fluid of concentration in the range $1-\varepsilon < \xi \leq 1$,

where $\varepsilon = 0.031$ (see Appendix D). It has a distinct " hump " in the middle of the layer which, upon closer inspection, was found to be due to the very large excess of high speed fluid in the cores referred to earlier. In accord with this behavior, the probability of finding pure L.S. fluid, defined by all the fluid in the concentration range $0 \leq \xi < \varepsilon$, has a rather flat region in the center of the layer. The average high speed fluid concentration, $\bar{\xi}$, which is given by equation D.4, is consistent with these observations. The total probability of finding mixed fluid, $P(y)$, is the area under the *pdf*, excluding the free stream delta functions, and in a way represents the amount of mixing in the layer. It should be born in mind that $P(y)$ shown in Figure 17a overestimates the amount of mixing because of the lack of resolution discussed earlier. The average mixed fluid concentration, C_m, is shown for the sake of completeness. It is not believed to be of much value since there is very little mixing in this case and, as might be expected, most of the data that have been labelled as mixed fluid are uniformly distributed between $\xi = 0$ and 1. It should be pointed out that this was the only set of data for which the point $y = 0$ was not chosen to be the location of maximum P, and instead the point at the peak of the " hump " in the pure H.S. probability was used.

4.2.1. *The Initial Composition Asymmetry*. The roll-up of the vortical structures in the mixing layer, subsequent to the exponential growth of disturbances, is not symmetric in y and is such that a much larger amount of H.S. fluid than L.S. is initially entrapped (Figures 11 & 15). Although there is evidence of this behavior in the literature, it seems to have been gone unnoticed. Such evidence can be found, for example, in the smoke pictures of Freymuth (1966) in the shear layer at the exit of a round jet and laser induced fluorescence pictures of Gharib (1983) of the roll-up in the shear layer over a cavity. This initial asymmetry has important implications on how the composition of the mixed fluid evolves during the mixing transition which will be addressed in § 4.5. Note that

if, by some mechanism, the core were to homogenize instantaneously, then the mixed fluid composition would be (less than, but) quite close to unity.

Most temporal calculations of the mixing layer have produced symmetric patterns and cannot explain the observations discussed above. The stability calculations of temporally growing disturbances (Michalke 1965), temporal growth and roll-up of an infinite uniform vortex sheet (Jimenez 1980), as well as the "cat's eye" solution of Corcos & Sherman (1976) fall in this category. The stability calculations of the spatially growing disturbances by Michalke (1965) and Michalke & Freymuth (1966) do, however, contain many of the essential features observed. The streakline pattern during rolling-up calculated by Michalke & Freymuth (1966) is shown in Figure 18a. This calculation was made at maximum amplification for the hyperbolic-tangent velocity profile. Even though the applicability of a velocity profile of this type to the initial region of the mixing layer is questionable, and a profile with a wake component may be more representative, it is nevertheless believed that Figure 18a can be applied to the actual situation. An argument in support of this conjecture is that the natural roll-up wavelengths are long, compared to the transverse extent of the velocity profile, so that the details of the initial velocity profile may not be important. The streakline that starts at the center of vorticity ($y = 0, \Omega = -0.5$) is shown in Figure 18b(I). If it is assumed that this is the dividing streakline that peels off the splitter plate, then this will also be the boundary between pure L.S. and H.S. fluids. The low speed fluid has been cross-hatched and it can be seen that the roll-up process results in an excess of high speed fluid in the core.

An interesting point is that our data (including other records not presented here), those of Freymuth (1966), and Gharib (1983) all show that the actual roll-up dividing streakline resembles Figure 18b(II) much more closely. This is the streakline that originates *below* the center of vorticity. It was suggested by P. E.

Dimotakis that the initial velocity profile of the mixing layer, as it peels off the splitter plate (basically two boundary layer profiles), is such that the center of vorticity is above the splitter plate. In any event, the initial composition asymmetry can be argued for on the basis of the spatial instability of the mixing layer.

4.3. High Reynolds Number; after the Mixing Transition

These measurements were recorded at $x = 25\ cm$ with $U_1 = 70\ cm/sec$ and $r = 0.38$. The shear layer thickness was measured to be $\delta_1 = 52.7\,mm$, resulting in a Reynolds number of $Re_{\delta_1} \approx 23{,}000$. The effective resolution area, under these conditions, was $486\,\mu m \times 100\,\mu m$.

A " photograph " of the composition field is presented in Figure 19. It was prepared in the same fashion as Figure 11. The change in the apparent aspect ratio of the large structures is due to the fixed scanning rate that was used in these measurements and the increase of the free stream velocities in order to raise the Reynolds number. This photograph contains all the essential features of the flow in this regime. The vortical motion of the structure brings in fresh fluid from the H.S. side (blue) all the way down to the L.S. side (red) and vice versa. The most striking result is the rather uniform composition of the fluid inside the structure which is more or less all green. The color has no tendency toward blue as the H.S. side is reached or towards red on the L.S. side. One way to view this uniformity is that the cores of the structures are very efficient mixers. The fluid on top will soon be found on the bottom due to the large circumferential velocities associated with the vortices. As a matter of fact, these velocities could be so high as to cause instantaneous regions of reversed flow (Dimotakis et al. 1981).

Time traces of the high speed fluid concentration and their *pdf*s are shown in Figures 20 and 21. The flow image, Figure 22, shows that these traces (labeled by white markers) correspond to the passage of large scale structures. The average *pdf*, $\bar{p}(\xi)$, is included to aid interpretation of the color assignment to various concentration levels to be found in the layer. The lateral composition uniformity, alluded to earlier qualitatively, can now be examined quantitatively. The most significant feature is that the functional form of the mixed fluid *pdf* changes very little across the mixing layer (Figure 21). This means that a given concentration of mixed fluid has roughly the same probability, relative to other concentrations, of being observed regardless of the position in the layer. Therefore, to the first order, we may think of the mixing layer as composed of structures filled with mixed fluid of spatially uniform composition. The absolute mixed fluid probability, at a given lateral point, would then be proportional to the fraction of time that the observer spends inside the structures. The support for this description may be better seen in Figure 23 where the *pdf*s of all the points are shown. It is interesting to note that it is as a consequence of this uniformity that $\bar{p}(\xi)$ becomes a useful quantity, with which one can characterize the entire layer.

Another notable feature is that the composition is asymmetric and biased toward the high speed fluid. The average concentration of the mixed fluid for the whole layer, C_M, was calculated to be 0.60 indicating a mixture of 1.5 parts of H.S. to 1 part of L.S. fluids. If the notion of entrainment limited mixing above the mixing transition is correct, to the extent that the composition of the mixed fluid is determined by the amounts entrained from the two sides, we would conclude that the entrainment ratio, E, is 1.5. Unfortunately, due to a variety of reasons, it is practically impossible to get the value of E from dilution data. There are two prime reasons for this difficulty. First, the lack of adequate resolution of the measuring device overestimates the value of C_M. Second, C_M may

not have attained its asymptotic value at this Reynolds number, since the mixed fluid composition is in a state of evolution during the mixing transition and it is not clear, from the present dilution data, when the asymptotic value is reached. These issues will be addressed in more detail in subsequent sections.

Certain features of this flow can be better seen in the transverse profiles of Figure 24. The smooth curve through the data points of $P(y)$ is an exponential fit of the type (after Mungal 1983)

$$P(y) = e^{-(c_0 + c_1 y + c_2 y^2 + c_3 y^3 + c_4 y^4)} \tag{4.1}$$

and the curve for pure L.S. and H.S. fluid probability, in the area with no data points, is $1-P(y)$ obtained from the fitted $P(y)$ described above. The fact that the maximum of the total mixed fluid probability is less than unity, indicates that the probability of finding unmixed fluid is never zero, even in the center of the layer. Most of the pure fluid in the center is found in the tongues of fresh fluid taking part in the entrainment process, but there are also small patches of still unmixed material in the cores, as can be seen on the photographs. The average mixed fluid concentration shows little variation in y, consistent with the transverse uniformity of the *pdf*s. Note that the average H.S. fluid concentration, $\overline{\xi}$, has a peculiar shape characterized by three inflexion points. Similar behavior can be found in the average density profiles of Brown & Roshko (1974) in their study of a gas mixing layer with different densities, the average concentration profiles of Konrad (1976) in both equal and unequal density gas shear layers, and the average temperature profiles, in a heated mixing layer, of Rajagopalan & Antonia (1981). Mean temperaure measurements of Fiedler (1975), in his heated mixing layer, have the same structure which, he concluded, suggests a transport mechanism in which large scale motion plays an important part.

4.3.1. *Comparisons.* Two recent theoretical attempts to calculate the probability density function of a passive scalar in turbulent shear flows, at high Reynolds number, are those of Pope (1981) and Kollmann & Janicka (1982). Pope modeled the turbulent transport by simple gradient diffusion and used a Monte Carlo method to simulate and solve the equations. Kollmann & Janicka also used a gradient-flux closure model and complemented it by the standard $k-\varepsilon$ turbulence model to provide turbulent diffusivity and time scale. Results of both of these studies, for the mixing layer, compared well with the measurements of the temperature *pdf* in a gaseous shear layer by Batt (1977). It is believed that these calculations should also be applicable to the present case of a liquid, since they do not explicitly depend on the mass diffusion coefficient, or in the non-dimensional form, the Schmidt number Sc. A comparison between the calculated *pdf* of Kollmann & Janicka and that measured in this investigation is shown in Figure 25. The two essentially point to totally different mechanisms for turbulent transport. The calculated *pdf*s change from point to point across the mixing layer and are more or less centered around the local mean, whereas the functional form of the ones measured remains very much the same all across. Note, for example, the trend of the peaks in the calculations as opposed to their relatively fixed position in the measurements. Our results indicate that turbulent transport, in this flow, is not a diffusive process and hence cannot be adequately decribed by gradient-diffusion models. Comparison with the findings of Pope lead to the same conclusions.

Konrad (1976) measured the probability density function of mixing, in a gaseous shear layer, with a concentration probe (see Brown & Rebollo 1972) using a passive scalar technique. The general structure of his *pdf*s is very similar to those for a liquid (see Figure 26). The average mixed fluid concentration, for the two cases, are shown in Figure 27. There seems to be more transverse variation in the case of the gas. It can not be said with certainty, however, whether

this is a true gas-liquid difference.

The evidence discussed so far, particularly Figure 23 and the photographs, suggests that any point in the mixing layer, in the case of a liquid at least, spends time in one of three regions : unmixed high speed, unmixed low speed and mixed at a composition whose *pdf* is fairly uniform across the layer. It will be shown later that some of the transverse non-uniformity of the composition field, as displayed by the variation of C_m in Figure 24, is artificially caused by the lack of adequate resolution of the measurement device, and that the *pdf*s could be, in fact, even more uniform than implied by the data.

Broadwell & Breidenthal (1982) proposed the following idealization for the fluid states in the turbulent shear layer : (i) unmixed, i.e. pure fluids from the two streams, (ii) a homogeneous mixture at the entrainment ratio, and (iii) strained laminar diffusion layers (flame sheets) between the free stream fluids. In water, which is characterized by a small diffusion coefficient ($Sc \approx 1000$), the contribution from the flame sheets is expected to be relatively small. The description suggested earlier then becomes similar to that of Broadwell & Breidenthal, with the exception that they represent the mixed fluid concentration at any given point by a single value, or a delta function *pdf*. In this connection, the work of Effelsberg & Peters (1983) should be mentioned, who offer a model for the probability density function along similar ideas as those of Broadwell & Breidenthal.

4.4. Calculation of the Amount of Product

The probability density function of mixing presented in the previous section can be used to estimate the amount of chemical product that would have been formed, were the free streams carrying reactants (Toor 1962). This estimate will be an upper bound since the passive scalar technique generally overestimates

the amount of molecular mixing (see § 1.3, 4.5). The central idea is that a particular mixed fluid concentration ξ corresponds to a unique product concentration $C_p(\xi;\varphi)$ which, for a one-step, fast and irreversible reaction of the type $A + B \rightarrow P$, is given by equation (D.14) of Appendix D. The equivalence ratio is defined by $\varphi \equiv C_{2_o}/C_{1_o}$ where C_{1_o} and C_{2_o} are the free stream molar concentrations of the H.S. and L.S. reactants respectively. The average product concentration profile across the layer, for a given φ, is calculated according to equation (D.15). And finally the total amount of product, represented by the product thickness, is found by integrating the average product concentration profile (equation D.16). It should be mentioned that the basic assumption is that the chemical reaction is dynamically passive. This will be true if the reactants are dilute and the reaction releases only small amounts of heat.

The calculated average product concentration, $\overline{C_p}(y;\varphi)$, is shown in Figure 28 for selected values of φ. In the top plot, C_{1_o} was kept constant and φ was changed by varying C_{2_o}. In the bottom plot, C_{2_o} was held fixed and φ was altered by changing C_{1_o}. Each of these curves is the exponential fit of equation (4.1) to 50 data points on the profile, which are not shown since the fit was excellent. It is mentioned, just in passing, that δ_1 agreed very well (within 2%) with a 1% width based on the average product profiles calculated above. Note that a pair of experiments performed at equivalence ratios of φ and $1/\varphi$ would result in two different average product concentration profiles. This effect, which was also observed by Mungal (1983) in his chemically reacting gaseous mixing layer, is a consequence of the mixed fluid composition asymmetry.

A comparison between Mungal's gas results and estimates for a liquid on the basis of the present dilution data, for φ = 1/8 & 8, is made in Figure 29. In this plot, the average product concentration $\overline{C_p}$ is normalized by the maximum possible value C_{p_s} (see equation D.13). $\overline{C_p}/C_{p_s}$ corresponds to $\overline{T}/Tflm$ of Mungal,

where $\overline{T}$ is the mean temperature rise and $Tflm$ is the adiabatic flame temperature. It can be seen that the shift in the peak of the profiles in the case of a liquid is less (by about a factor of two) than that in a gas.

As Mungal had pointed out, two product thicknesses can be defined depending on whether C_{1o} or C_{2o} is used for normalization. The first, δ_{p_1} is the area under $\overline{C_p}/C_{1o}$ and the second, δ_{p_2} is the area under $\overline{C_p}/C_{2o}$. These two thicknesses, normalized by the layer width, δ_1, are plotted in Figure 30. At large φ, δ_{p_1}/δ_1 asymptotes to 0.289 and for large φ^{-1}, δ_{p_2}/δ_1 tends to 0.192. At a φ (and φ^{-1}) of 10 they have already reached 98% of their asymtotic value.

Breidenthal (1978), using a chemical reaction technique, measured a value of 0.38 for $\delta_{p_2}(\varphi \to 0)/\delta$, where δ is the vorticity thickness. In order to compare results, we need to know the relation between δ_1 and δ. Brown & Roshko (1974) give the following relations for a constant density mixing layer

$$\frac{\delta_{vis}}{(x-x_o)} = 0.38\left[\frac{1-r}{1+r}\right] \tag{4.2a}$$

$$\frac{\delta}{(x-x_o)} = 0.18\left[\frac{1-r}{1+r}\right] \tag{4.2b}$$

where x_o is the virtual origin. As a result of these formulas and an earlier discussion showing the good agreement between δ_1 and δ_{vis}, the relations below have been used throughout the rest of this work

$$\frac{\delta_1}{\delta} = \frac{0.38}{0.18} = 2.1 \tag{4.3a}$$

Thus, we also have

$$\frac{Re_{\delta_1}}{Re_{\delta}} = 2.1 \qquad (4.3b)$$

Therefore, the estimate for the amount of product $\delta_{p_2}(\varphi \to 0)/\delta$, from the present data, becomes 0.40. This is in good agreement with the measurement of Breidenthal. Considering the overestimation of the amount of product inherent in the dilution technique, however, it is believed that Breidenthal's value may be too high. A direct measurement of the amount of product, in a chemically reacting layer, will be presented in the next chapter.

In closing this section, a visual demonstration of the effect of the mixed fluid composition asymmetry on the amount of chemical product is displayed in Figure 31. A " flip " experiment, at a pair of equivalence ratios of 1/4 and 4, was performed on the data of Figure 19. The picture corresponds to running two experiments with the same pair of reactants and simply exchanging their sides. This was done by assigning an intensity variation to the data, on the image processing monitor screen, according to $C_p(\xi;\varphi)$, for φ of 1/4 and 4, given by equation (D.14). That the case of $\varphi = 4$ shows more product than $\varphi = 1/4$ is clear.

4.5. Effect of Resolution

A fundamental problem associated with the passive scalar technique, a variation of which is the present dilution experiment, is that it cannot provide information on mixing inside a scale smaller than the resolution volume connected with the measurement apparatus. As was discussed in Chapter 1, in the case of LIF measurements, the technique measures the correct dye concentration inside its sampling volume. It is not known, however, whether this corresponds to any mixing at all (see Figure 2). While we could make sound statements about mixing and species concentration fluctuations down to the resolution scale of the measuring device, the only piece of information about the inside of this volume

is the *average* dye concentration. This is the reason why this technique can only provide an upper limit to the actual amount of molecular mixing. In this regard, it should be mentioned that the smallest diffusion scale, λ_D, is given by

$$\lambda_D \sim Sc^{-1/2}\, \delta_1\, Re_{\delta_1}^{-3/4} \tag{4.4}$$

where $Sc = \nu/D$ is the Schmidt number (for a derivation see Appendix A of Breidenthal 1978). For the experiment of § 4.3, $Sc \approx 600$, $\delta_1 \approx 53\,mm$, $Re_{\delta_1} \approx 23{,}000$ which result in $\lambda_D \approx 1\,\mu m$, well below the effective resolution ($486\,\mu m \times 100\,\mu m$) of the measurement.

It was somewhat difficult to improve the spatial and temporal resolution of the system, but they could very easily be made worse. So in order to address the question of resolution, the array scan time was increased by a factor of 10, resulting in an effective resolution area of $4\,mm \times 100\,\mu m$, and measurements were made on the same flow considered in § 4.3. Note that this increase in the size of the sampling volume should not be expected to answer any questions regarding the scales down to λ_D, since both sampling volumes are so much larger than this scale.

The effect of lowering the resolution on the measurement of the *pdf* is shown in Figure 32. Figure 32a is the contour plot of the original data in Figure 23. It is the view from above. The difference between the low and high resolution *pdf*s is the contour plot of Figure 32b. Solid lines are positive contours. They indicate the areas where the *pdf*s get more populated due to the worse resolution. Broken lines are negative contours. They mark the areas that become less populated. The qualitative result is that toward the H.S. side ($y > 0$) the *pdf*s start gaining on the high values of concentration and loosing on the low concentration values. As the L.S. side is approached ($y < 0$), the trend reverses. It is apparent that the composition field is made to look less uniform across the

layer than it really is. It is interesting to note that the lack of resolution distorts the *pdf*s in a direction that is qualitatively similar to what would be expected from a diffusion process.

More quantitative comparisons are illustrated in Figure 33. The total mixed fluid probability increases everywhere in the layer at the expense of lowering the probabilities of finding pure low and high speed fluids (Figures 33a & b). The measurement indicates more mixed fluid. The variation of the average mixed fluid concentration, across the layer, has increased, consistent with the earlier qualitative discussion, indicating the *pdf*s are getting less uniform. As a matter of fact, if the temporal resolution is reduced to zero by making the array scan time very long, C_m would become equal to the average H.S. fluid concentration $\overline{\xi}$. Lowering the resolution does not affect the $\overline{\xi}$ profile, as expected, since it is based on measuring the correct *average* dye concentration, and not its fluctuations. The total mean mixed fluid concentration, C_M was calculated to be 0.62, higher than the previous value of 0.60.

That the lack of resolution would give results indicating a higher degree of mixing was, of course, already known and mentioned at the beginning of this section. This study has further demonstrated that the lack of adequate resolution can indicate a composition field that is less uniform, across the layer, than it really is (e.g. see the C_m profile in Figure 33c). This brings up the very interesting question of just how uniform is the curve of $C_m(y)$? This issue will be discussed in the next chapter, where a chemical reaction technique is used to get an estimate of C_m that does not suffer from resolution problems.

4.6. Evolution of the PDF during the Mixing Transition

We have so far discussed the composition field in the mixing layer before and after the mixing transition. Breidenthal (1978) showed that the extent of mixing in a liquid layer increased monotonically, during the mixing transition, from a very small value, before the transition, to a higher asymptotic value, above the transition. His study was, however, concerned with the total amount of mixing and did not provide any clue to the actual distribution of the mixed fluid concentration (i.e. the *pdf*). The question still remains as to how the *pdf*s evolve in the region of mixing transition. How does a structure with a very large excess of pure H.S. fluid in its core, prior to the mixing transition, evolve into one with a total mean mixed fluid concentration of 0.60, above the transition ?

To find an answer to this question, measurements were conducted at two Reynolds numbers in the transition region. Both were at $x = 17\ cm$ and $r = 0.38$. For the first set $U_1 = 30\ cm/sec$, $\delta_1 = 38.5\ mm$ ($Re_{\delta_1} \approx 7{,}200$), and the effective resolution area was $266\ \mu m \times 100\ \mu m$. For the second experiment $U_1 = 50\ cm/sec$, $\delta_1 = 38.5\ mm$ ($Re_{\delta_1} \approx 12{,}000$), and the effective resolution area was $376\ \mu m \times 100\ \mu m$.

The average *pdf*s for the four cases studied in this chapter are shown in Figure 34. The amount of product, δ_{p_2}/δ_1, was calculated for each case (for large φ^{-1}) and is compared with the data of Breidenthal in Figure 35. The good agreement between the two, previously commented upon for the highest Reynolds number case, holds for all the points. The most important result is that the composition of the mixed fluid changes continuously in the mean, during the mixing transition (Figure 34). In this region, not only does the *amount* of product change, but also the product is found at a different *composition*. As mixing starts ($Re_{\delta_1} \approx 7{,}200$), the fluid is found mixed mostly at very high values of concentration ξ. The distribution shifts toward lower values as mixing proceeds.

Another way of looking at this evolution is to monitor the average mixed fluid concentration of the entire layer, C_M, which monotonically decreases during the transition (see the values in Figure 34). Even though there is not enough data to confirm this conclusively, the process seems to be one in which the newly entrained fluid continuously mixes with the existing fluid in the core in an essentially a dilution process. Considering that the cores are initially filled with H.S. fluid, the continuous decrease of C_M is explained, at least, qualitatively. The concentration corresponding to the entrainment ratio, E, is $C_E = \frac{E}{1+E}$, where E is the volume ratio of the entrained H.S. to L.S. fluid. If the dilution mechanism, proposed above, is correct, C_M should asymptote to C_E at some high value of Reynolds number. Until this asymptotic state is reached, C_M will necessarily be higher than C_E. In other words, the average composition in the mixing layer would not be determined only by the entrainment ratio. Unfortunately, the present dilution results do not answer the question of what the asymptotic value of C_M is and how high of Reynolds number is required to get to it. The chemically reacting experiments of the next chapter will provide some answers.

We are now in a position to explain why the " flip " experiment of Chapter 3 produced such a large difference in the amount of product. Recall that the experiment accentuated the difference in the amount of mixed fluid to be found in the range $\xi > 0.64$ and $\xi < 0.36$. The Reynolds number of the experiment corresponded to the early stages in the mixing transition. According to the results described in the previous paragraph, the mixed fluid concentration in this regime is asymmetric and strongly biased toward the H.S. fluid. If, just to demonstrate the point, we take the average *pdf* at Reynolds number 7,200 from Figure 34 to represent the composition field of this experiment, we see that all the mixed fluid is essentially at a concentration above 0.5. In view of this, the outcome of that experiment is no longer a mystery.

A comparison of the transverse profiles of the probability of finding pure L.S. and H.S. fluids, $P(y)$, and C_m is shown in Figure 36. Photographs of the flow at the two intermediate Reynolds numbers are displayed in Figure 37 in order to aid in the interpretation of results. The initial large excess of pure H.S. fluid in the layer, still seen at $Re_{\delta_1} \approx 7{,}200$, very quickly diminishes as the introduction of three-dimentionality mixes the core fluid rapidly. Note the regions of still unmixed H.S. fluid in the cores in Figure 37b, and that the color of mixed fluid is tending toward light blue. Since there is originally a small amount of pure L.S. fluid in the cores, the changes in the probability of finding it are not as striking. The evolution of $P(y)$, Figure 36c, illustrates the increase of mixing during transition. And finally the flatness of C_m profile indicates that, even in the transition region, the mixed fluid composition is quite uniform across the width of the layer. Its shifting down to lower values, as Reynolds number increases, is in accord with the evolution of the *pdf* described previously.

Chapter 5

CHEMICALLY REACTING EXPERIMENTS ; LINE ILLUMINATION

The extent of mixing, in a liquid mixing layer, was measured by Breidenthal (1978) in a direct way using a chemical reaction method. He found that the amount of chemical product in the limit of very small equivalence ratio, represented by the product thickness normalized by the layer width $\delta_{p_2}(\varphi \to 0)/\delta_1$, reached a constant value above the mixing transition. Due to the asymmetry of the mixed fluid composition, discussed in the previous chapter, we now know that a second limit must also exist for very large equivalence ratio given by $\delta_{p_1}(\varphi \to \infty)/\delta_1$.

An upper bound for these two product thicknesses was given in Chapter 4. It was found that the estimated value of $\delta_{p_2}(\varphi \to 0)/\delta_1$ agreed well with the measurements of Breidenthal, and hence it is believed that his value could be too high. A direct measurement of the amount of mixing, besides being important in its own right, would allow us to determine the average mixed fluid composition profile, $C_m(y)$, and the mean composition of the mixed fluid of the whole layer, C_M, independent of the resolution of the measuring apparatus. This could be done since $C_m(y)$ and C_M can be calculated from the *average* product concentration profiles using equations (D.18) and (D.19). The product concentration is equal to the fluorescing dye concentration (equation C.7) and it has already been mentioned, in the previous chapter, that the inability to resolve the smallest mixing scales does not affect the true measurement of the mean fluorescent dye concentration.

The specific questions addressed in this chapter are :

1. What are the values of the product thicknesses $\delta_{p_1}(\varphi \to \infty)$ and $\delta_{p_2}(\varphi \to 0)$, for a liquid, above the mixing transition ?

2. Is the variation of $C_m(y)$ profile across the layer, measured by the passive scalar technique in Chapter 4, real or is it simply a result of the lack of adequate resolution of the measurement device ?

3. What is the value of C_M above the mixing transition ?

4. Does C_M remain constant above the mixing transition ? If so, what is the inferred value of the entrainment ratio E ?

In the measurements that are described here, a 1024 element photodiode array was used with a scan time of $2\,msec$. Only one out of every four pixels was digitized (see Chapter 2). The chemical reaction was an acid-base reaction with a negligible amount of heat release. The details of the LIF chemically reacting technique and data processing are covered in Appendices A, C and D. All the experiments were conducted at φ = 1/10 and 10, which are believed to adequately represent the limits of $\varphi \to 0$ and ∞. This is based on the results of Chapter 4, Figure 30, which showed that the amount of product reached its asymptotic value at a rather low value of φ (and φ^{-1}). Another way of expressing this is that there is very little mixed fluid to be found in the ranges $\xi < \varphi/(1+\varphi) = 0.09$ and $\xi > 0.91$. To confirm this, the *pdf* of the high Reynolds number data of §4.3 was used to estimate the amount of product for LIF chemically reacting experiments at φ of 1/10 and 10 according to the procedure described in §D.2. It was found that, at these equivalence ratios, the product thicknesses had attained 95% of their final values. The estimated average product concentration profiles for these two cases will be discussed later.

The width of the mixing layer, δ_1, was defined by the 1% width of the average product concentration profile $\overline{C}_p(y)$. It is the distance between two points where the profile has dropped to 1% of its peak value. The location of $y = 0$ was chosen entirely arbitrarily. In trying to be consistent with its definition in Chapter 4, a function was defined to be equal to the area of the histogram of the time-series data, excluding the data in the lower 3% range. The location of the peak of this function was selected as $y = 0$.

5.1. Flip Experiment, φ = 1/10 & 10

These two runs were made under indentical conditions as the high Reynolds number experiment of Chapter 4. They were recorded at $x = 25\ cm$ with $U_1 = 70\ cm/sec$ and $r = 0.38$. The shear layer thickness was measured to be $\delta_1 = 51.2\,mm$, in very good agreement with the nonreacting case, resulting in a Reynolds number of $Re_{\delta_1} \approx 22{,}200$. The effective resolution area, under these conditions, was $1.1\,mm \times 90\,\mu m$. For the $\varphi = 1/10$ run, the acid solution was on the low speed side with the base on the high speed side. For the $\varphi = 10$ run , the sides of the chemicals were switched.

Time traces of the product concentration, $C_p(t)$, at selected points in the layer, are shown in Figures 38 and 39 for $\varphi = 1/10$ and 10 respectively. Each trace is composed of 512 consecutive data points connected by straight lines. The data are normalized by the maximum attainable product concentration C_{p_s}, which is reached at the stoichiometric conditions for fluorescence " turn-on " (see Appendices C and D). The flow images corresponding to the time interval of Figures 38 and 39 are displayed in Figure 40(a,b). They were constructed from the time-series data at 150 points across the layer in the manner described in the previous chapter. The intensity assignment to the data is according to $C_p(\xi;\varphi)$ described in Appendix D, with a linear variation between the maximum

intensity at $C_p = C_{p_s}$ and zero intensity at $C_p = 0$. This is how the chemical product would look if it were being observed in real time during the experiment. The two horizontal lines mark the width of the layer δ_1. Note that C_p never reaches C_{p_s} in any of the time traces. Figures 38 and 39 show that the product concentration for $\varphi = 10$ reaches higher values than for $\varphi = 1/10$. This can more easily be seen in the different intensities of the images in Figure 40, which also show that it is possible to find instances when there is very little product anywhere across the layer.

The main results are summarized in Figure 41. The average product concentration profiles for both equivalence ratios are plotted along with C_m which was calculated using equation (D.18). There was no need to use a fit to the data as there were at least 150 data points on the profiles. It should be mentioned that δ_1 and the location of $y = 0$ were the same in both cases. The area under each average profile gives the total amount of product for that case and they are

$$\frac{C_{1o}}{C_{p_s}} \frac{\delta_{p_1}(\varphi = 10)}{\delta_1} = 0.182$$

$$\frac{C_{2o}}{C_{p_s}} \frac{\delta_{p_2}(\varphi = 1/10)}{\delta_1} = 0.138$$

But we also have, from Appendix D, that $C_{p_s}/C_{1o} = 0.91$ for $\varphi = 1/10$ and $C_{p_s}/C_{2o} = 0.91$ for $\varphi = 10$. Therefore the final result is

$$\frac{\delta_{p_1}}{\delta_1} = 0.165 \quad \text{for } \varphi = 10$$

$$\frac{\delta_{p_2}}{\delta_1} = 0.125 \quad \text{for } \varphi = 1/10$$

These results show that the previous estimates, based on the dilution data (with the accompanying resolution difficulties), were too high by about 50% for the δ_{p_2} limit and about 75% for the δ_{p_1} limit. Note also that the φ = 10 case has about 32% more product than that for φ = 1/10. The average mixed fluid concentration for the entire layer, C_M, was determined (equation D.19) to be 0.57, lower than the previous value of 0.60 calculated from the dilution data. The present value of C_M corresponds to a mixture of 1.32 parts of H.S. fluid to 1 part of L.S. fluid. If we now invoke the idea of entrainment limited mixing above the mixing transition, we conclude that the entrainment ratio is E = 1.32. This discussion will continue in the next section

It would be instructive to compare the measured average product concentration profiles with the predictions based on the non-reacting results (i.e. the *pdf* of dilution data). This comparison is made in Figure 42. The product profiles at φ = 1/10 & 10, for which $C_p(\xi;\varphi)$ is given in §D.2.1, are estimated from the *pdf*s of the high and low resolution data of Chapter 4 using equation (D.15b). The overestimation of the true extent of molecular mixing by the passive scalar technique, which is due to resolution difficulties, can clearly be seen. A quantity that is closely related to the degree of mixing is the total probability of finding mixed fluid in the layer P (see Appendix D). It can be estimated from the present chemically reacting data according to equation (D.17) and the result is shown in Figure 43. Note that this estimate does not suffer from resolution problems since it is calculated from the *average* product profiles. In comparing with dilution results, Figure 43 again indicates the drawbacks of the passive scalar technique in determining the true extent of mixing. Note that the chemically reacting results indicate that the probability of finding unmixed fluid

(given by 1-P), in the center of the layer, could be as high as 0.45.

The average mixed fluid concentration, C_m, can be estimated from the present chemically reacting data using equation (D.18). To make a fair comparison between this estimate and those obtained by the dilution technique, C_m was recalculated, for the dilution case, using the average product profiles of Figure 42 and equation (D.18). The results are shown in Figure 44. Note that the new calculations of C_m, from the dilution data, are slightly different from those presented earlier in Figure 33c. The difference is caused by the small amount of mixed fluid in the *pdfs* in the range $\xi < 0.09$ and $\xi > 0.91$. The average mixed fluid concentration found from the chemical reaction technique does not suffer from resolution problems and indicates that this quantity is very uniform across the entire width of the layer. It furthermore reveals that a good portion of the variation seen in the estimates from the dilution data is an artifact, and is due to the resolution inadequacy of the measurement technique. Note also that the agreement improves toward the low speed side of the layer. This is partly due to the improvement of the effective resolution as the low speed side is approached as a result of lower local flow speed (see beginning of Chapter 4).

The present direct measurement of the amount of product, for $\varphi \rightarrow 0$, is 30% lower than the previously measured value by Breidenthal (1978). Both measurements were performed in the same facility and utilized the chemical reaction technique. Breidenthal used the attenuation of green light by the red product, which was formed as phenolphthalein reacted with a base, to measure the amount of chemical product. The discrepancy is believed to be associated with the difficulties mentioned below :

1. The equivalence ratio of Breidenthal's experiment is not as low as it was originally assumed and, we believe, it could be as high as 1/4.

2. There is a question concerning the magnitude of dilution in his calibration sample. Any dilution of the sample would result in a low estimate of the normalizing concentration that appears in the denominator of equation (D.16b).

3. Absorption of light by the unreacted phenolphthalein would cause an overestimation of the product.

An accurate assessment of the magnitude of the error caused by these factors cannot, however, be firmly established.

5.1.1. *Comparison with Gaseous Results.* Comparisons are made with Mungal's chemically reacting gaseous results which were recorded at $Re_{\delta_1} \approx 65{,}120$. His data for $\varphi = 1/8$ and 8 have been used, utilizing equation (D.18), to infer the average mixed fluid concentration for the gas case (Mungal, private communication). This is contrasted with the present liquid result ($Re_{\delta_1} \approx 22{,}200$) in Figure 45. It is not clear how the C_m profile of the liquid case would change if the Reynolds number were to increase three-fold. If the effect is negligible, the fact that the gas C_m varies a lot more than its liquid counterpart indicates that the gaseous *pdf*s must be less uniform, across the mixing layer, than those for a liquid. The gas shows more mixed fluid of high ξ on the H.S. side and more of low ξ toward the L.S. side. This would be the type of qualitative result one might expect due to the much larger mass diffusion in a gas ($Sc \sim 1$).

Another comparison concerns the amount of mixing. It has been known, from the work of Konrad, Breidenthal and Mungal, that gases and liquids produce different amounts of product. Mungal puts the limiting values in the gas at $\delta_{p_1}(\varphi \to \infty)/\delta_1 = 0.27$ and $\delta_{p_2}(\varphi \to 0)/\delta_1 = 0.24$. Results of Breidenthal and Mungal had indicated that the amount of product in the gaseous layer was 20% to 25% more than in a liquid. The present data , however, support a larger

difference. The gaseous case, represented by Mungal's data, has 50% more product than the liquid layer investigated here. It is instructive to note that, in the context of the Broadwell-Breidenthal model, this means that the homogeneous region and the flame sheets contribute equally to the product in the gaseous layer. A summary of the data for $\delta_{p_g}(\varphi \to 0)$ is provided in Figure 46.

The validity of the comparison between the liquid and gaseous product measurements, described above, requires some discussion. One issue is that, in the present liquid experiments, a measurement at station $x = x_1$ gives the amount of product formed as a result of the *local* mixture composition at that station. In Mungal's gas experiment, by contrast, the amount of product that is measured at x_1 is the *cumulative* amount of product formed between the splitter plate ($x = 0$) and x_1, a consequence of the irreversibility of $H_2 + F_2$ reaction. Comparing the results of these two types of experiments, however, may not be valid in general. This would be the case when there is a substantial minimum activation energy required for the reaction to proceed, for example, or if the chemistry is slow. In the special case of fast chemistry and spontaneous reactions (i.e. hypergolic reactants) the comparison *is* valid. The reason is that, in this case, no more product can be formed than that dictated by the reactant in short supply (i.e. the lean reactant). Therefore, the total amount of product at x_1 would be the same whether the reactants were to react, irreversibly, starting at $x = 0$, or to mix passively, without any reaction, and then instantaneously react to completion at x_1.

Another aspect of the comparison must also be discussed. In the present experiment, an amount of product corresponding to the range of mixture ratios for which the fluorescence is *off* is missing from the total amount. This contribution, however, was shown to be small for the choice of equivalence ratios used in these experiments.

5.2. Very High Reynolds Number, $\varphi = 10$

This experiment was conducted to determine if the the amount of chemical product found in the previous section remains constant with an increase in the Reynolds number. It was performed at $x = 25\ cm$ with $U_1 = 315\ cm/sec$ and $r = 0.38$. The layer thickness was measured to be $\delta_1 = 40.1\ mm$, resulting in a Reynolds number of $\mathrm{Re}_{\delta_1} \approx 78{,}300$. The effective resolution area, under these conditions, was $4.4\ mm \times 90\ \mu m$.

Time traces of the product concentration and the flow picture corresponding to this time interval are shown in Figures 47 and 48. The apparent change of the aspect ratio of the structures is due to the increase of free stream velocities in order to raise the Reynolds number. The presence of large structures containing the chemical product is clearly seen. We can still find instances when there is very little product anywhere across the whole layer. The average product concentration profile, Figure 49, was integrated and the area was found to be very close to that in the lower Reynolds number case of § 5.1. Note that the area is already normalized by δ_1. Even though the layer is thinner in this case, the product thickness is also smaller just in the right proportion to keep the ratio constant. The measured value of the amount of product is $\delta_{p_1}/\delta_1 = 0.167$.

We are now in a position to answer the last question that was raised at the beginning of this chapter. It was already known, by the work of Breidenthal in a liquid layer, that above the mixing transition $\delta_{p_2}(\varphi \to 0)/\delta_1$ became a constant. We believe that his estimate for that quantity is too high and the correct value is about 0.125 (see discussion in § 5.1.1). With the result of this section, we have shown that the second limit $\delta_{p_1}(\varphi \to \infty)/\delta_1$ also becomes constant above the mixing transition (at least up to Reynolds number of 78,200) with a value of about 0.165. This means that the average mixed fluid concentration of the layer C_M necessarily becomes fixed (equation D.19) at 0.569, which corresponds to a

mixture of 1.32 parts of H.S. fluid to 1 part of L.S. fluid. If the fluids that get entrained into the layer become mixed with the existing mixed fluid some time later, the fact that the average mixed fluid concentration remains constant can only imply a fixed entrainment ratio E such that $C_E = \frac{E}{1+E} = C_M$ and therefore $E = 1.32$. Note also that, in this case, $E = \delta_{p_1}(\varphi \to \infty)/\delta_{p_2}(\varphi \to 0)$ so that the two limiting product thicknesses would become equal only if the entrainment ratio were equal to unity.

The value of the entrainment ratio found above agrees very well with Konrad's value of 1.3 for the gaseous layer at the same velocity ratio. It is interesting that the two agree as well as they do considering that they were measured by totally different techniques. Konrad estimates the entrainment rates using an expression suggested by the earlier work of Brown (1974). The present result is based on the direct measurement of the mixed fluid concentration. The connection between the two has yet to be explored.

5.3. Mixing at Very Low Reynolds Number

This is a short study of mixing just as the mixing transition starts. The experiment was done at $x = 25\,cm$ with $U_1 = 17.4\,cm/sec$, $r = 0.48$ and equivalence ratio $\varphi = 1/10$. The shear layer thickness was $\delta_1 = 42.3\,mm$, corresponding to a Reynolds number of $Re_{\delta_1} \approx 3{,}800$. The effective resolution area was $347\,\mu m \times 90\,\mu m$.

Product concentration traces, Figure 50, show more fluctuations than the higher Reynolds numbers studied before. There are also larger regions where there is no product in the layer. Upon examining the photograph of the flow, Figure 51, it is revealed that most of the product is found on the interfaces and that the cores of the structures are more or less product free. The average

product concentration profile is shown in Figure 52. The integrated amount of product was $\delta_{p_2}/\delta_1 = 0.057$ which, as expected, is less than the value above the mixing transition.

Chapter 6

CONCLUSIONS

The processes of entrainment and mixing have been investigated in a liquid mixing layer using laser induced fluorescence diagnostics and high speed, real-time digital image acquisition techniques. Both reacting and non-reacting layers were studied over a range of Reynolds numbers covering the extent of the mixing transition. The bulk of the experiments have been performed at a velocity ratio of 0.38.

In the non-reacting cases, a passive scalar technique has been used to measure the probability density function (*pdf*) of the composition field of one of the mixing species. Results are used to estimate an upper bound for the amount of chemical product for a one-step, fast and irreversible reaction. Effects of the lack of resolution of the measurement apparatus are also examined.

The chemically reacting cases employ a diffusion-limited acid-base reaction to directly measure the extent of mixing on a molecular level and the amount of chemical product. Results are further utilized to infer the mean composition of the mixed fluid based on which a value for the entrainment ratio is determined.

A summary of the results is presented below.

1. The initial roll-up of the vortical structures in the mixing layer is not symmetric in the lateral direction y and is such that the cores contain a large excess of high speed fluid. This initial asymmetry can be explained on the basis of the spatial instability of the mixing layer.

2. Below the mixing transition, the composition field consists of mainly pure high and low speed fluids. There is very little mixing and that occurs at the interfaces separating the two free stream fluids. Consistent with these observations, the chemical product is found on these interfaces with large areas void of any product.

3. The mixed fluid composition changes continuously in the mean in the course of the mixing transition. In this region, not only does the *amount* of product change, but also its *composition*. As mixing starts, the fluid is found mixed mostly at very high values of concentration. The *pdf* is considerably asymmetric in favor of the high speed side. The distribution shifts toward lower values as mixing proceeds. It is proposed that a dilution mechanism, in which the newly entrained fluid continuously mixes with the existing fluid in the cores, explains this behaviour qualitatively.

4. The average composition of the mixed fluid during the transition is not determined only by the entrainment ratio but also by the initial composition at roll-up.

5. A consequence of the large asymmetry of the mixed fluid composition, in the transition region, is that a chemically reacting " flip " experiment exhibits a great difference in the amount of product formed upon switching the sides of the chemicals.

6. The *pdf* of the mixed fluid, above the mixing transition, is quite uniform across the entire transverse extent of the mixing layer. It is asymmetric and biased toward the high speed fluid. The lateral uniformity of the *pdf* is also observed during the mixing transition.

7. The evidence suggests that a fluid element in the mixing layer is found in one of three types of fluids : unmixed high speed fluid, unmixed low speed

fluid and mixed fluid at a composition whose *pdf* is fairly uniform across the layer. This description of fluid states in the turbulent mixing layer is qualitatively similar to that of Broadwell & Breidenthal, applied to the case of a fluid with a high Schmidt number, with the exception that they represent the mixed fluid concentration at any given point by a single value (delta function *pdf*).

8. The probability of finding unmixed fluid is never zero at any point in the layer, even in the center of the layer. Most of the unmixed fluid is found in the tongues of fresh fluid that are transported across the layer as they take part in the entrainment process. Some contribution also comes, especially in the transition region, from the still unmixed high speed fluid in the cores. Chemically reacting data indicate that the probability of finding unmixed fluid in the center of the layer, above the mixing transition, could be as high as 0.45 (measurement at $Re_{\delta_1} \approx 22{,}200$).

9. Turbulent transport, in the cases studied, is not a diffusive process and cannot be adequately described by gradient-diffusion models. It is dominated, instead, by large scale structures.

10. The inability of the measurement apparatus to resolve the mixed fluid at the diffusion scales overestimates the extent of mixing (already known result). It has also been shown that this lack of resolution can indicate a composition field that is less uniform, across the layer, than it really is. In this regard, care should be taken in interpreting any measured *pdf*s since some of the features may be a result of inadequate measurement capabilities.

11. An upper bound for the amount of chemical product, for a one-step, fast and irreversible reaction, has been calculated based on the measured *pdf*s

above the mixing transition. In the limit of small equivalence ratio ($\varphi \to 0$), the product thickness normalized by the layer thickness has been estimated to be $\delta_{p_2}/\delta_1 = 0.192$. This value compares well with Breidenthal's measurement using a chemical reaction technique. In view of the overestimation of the amount of mixing inherent in the passive scalar technique, it is believed that Breidenthal's value is too high (see also the discussion of § 5.1). The amount of product, in the limit of $\varphi \to \infty$, is calculated to be $\delta_{p_1}/\delta_1 = 0.289$.

12. The amount of chemical product, in the same mixing layer, depends on which side of the layer the reactants are placed (corresponding to runs at φ and $1/\varphi$), even above the mixing transition and at high Reynolds numbers. This is a direct consequence of the asymmetry of the mixed fluid composition.

13. The direct measurement of the amount of product, in a chemically reacting layer, has yielded that $\delta_{p_2}/\delta_1 = 0.125$ for small φ and $\delta_{p_1}/\delta_1 = 0.165$ for large φ. The previous estimates, based on the passive scalar results, have therefore overpredicted the amount of mixing by about 50% and 75% respectively. This is due to the resolution difficulties associated with the passive scalar technique which generally overestimates the extent of mixing.

14. The liquid reacting mixing layer has roughly 50% less product than a gaseous reacting layer, as measured by Mungal. This implies, in the context of the Broadwell-Breidenthal model, that the homogeneous region and the flame sheets contribute equally to the product in the gaseous layer.

15. Chemically reacting data strongly suggest that the average mixed fluid concentration across the layer is essentially constant, at least for the

measurements above the mixing transition at $Re_{\delta_1} \approx 22{,}200$. This indicates that most of the lateral variation of this quantity, seen in the estimates from dilution data, is due to the lack of adequate resolution. It, furthermore, suggests that the functional form of the mixed fluid *pdf* could be the same, exactly, regardless of the position in the layer.

16. The evolution of mixing above the mixing transition has been addressed in terms of the mean composition of the mixed fluid in the layer, C_M, measured using chemical reactions. It is found that increasing the Reynolds number Re_{δ_1} from 22,200 to 78,300 does not change the value of δ_{p_1}/δ_1 (in the limit of large φ). Using Breidenthal's similar result for the constancy of δ_{p_2}/δ_1 (in the limit of small φ) above the transition, and the newly measured value for this quantity, it is shown that C_M is fixed at 0.57 above the mixing transition.

17. The fact that the mean composition of the mixed fluid becomes constant above the mixing transition indicates that mixing has reached an asymptotic stage. The value of the entrainment ratio, defined by the volume of high speed to low speed fluids entrained, corresponding to the measured value of C_M, is 1.32. This number is in agreement with the measurement of Konrad in a gaseous layer at the same velocity ratio.

Appendix A

NOTES ON THE LASER INDUCED FLUORESCENCE TECHNIQUE

Fluorescence is a process in which the molecules of a substance absorb photons from an external energy source, and subsequently, reradiate some of the absorbed energy. Sodium fluorescein, which is a high quantum-yield organic dye, was used in this investigation. When excited with argon ion laser radiation, this dye fluoresces with a very short response time at wavelengths longer than the exciting wavelength. Specific features of this technique that are important for the present work are discussed below.

A.1. Fluorescence-Concentration Relationship

Linearity of the fluorescence intensity in the local dye concentration and laser intensity has been used, throughout this work, to obtain quantitative species concentration information. We now examine the conditions under which the linear relation is applicable.

The fluorescence intensity I_f emitted over a length Δy at a station y along the laser beam is given by

$$I_f(y) = Q \left[1 - e^{-\varepsilon_o \int_y^{y+\Delta y} C_d(y)\, dy}\right] I(y) \qquad (A.1)$$

where

Q = quantum yield

ε_o = dye molar absorption coefficient

C_d = local molar dye concentration

I = local laser intensity

For small values of $\varepsilon_o C_d \Delta y$ and small Δy the above equation can be replaced by

$$I_f = (Q \varepsilon_o \Delta y) C_d I \qquad (A.2)$$

The largest value of $\varepsilon_o C_d \Delta y$ used in these experiments was approximately 0.0016, for $\varepsilon_o C_d \approx 0.16\ cm^{-1}$ (Figure A.1) and $\Delta y \approx 0.01\ cm$ (Appendix B). The quantum yield Q is generally a function of dye concentration. For the dye used in the present work, Q remains nearly constant (less than 1.5% change between C_d of 10^{-5} and $10^{-7}M$) until the critical dye concentration of $5 \times 10^{-4}M$, where a sharp decrease in Q sets in (Figure 116 & Table 64 of Pringsheim 1949). The highest dye concentration used ($10^{-6}M$) was a factor of 50 below this critical concentration. As a consequence, the resulting fluorescence intensity is linearly proportional to the local dye concentration and the local laser intensity. The constant of proportionality is determined by the properties of the dye and the optical setup.

A.2. Fluorescein Dye

The water-soluble organic dye disodium fluorescein (uranin) was used in all the experiments. This dye fluoresces efficiently when excited by an argon ion laser, provided it is in a chemical environment whose pH is above a certain threshold. Generally, the fluorescence is *off* (suppressed) when the pH of the solution is below approximately 4.

In the dilution experiments, both free streams of the shear layer were water with dye premixed with one of the streams. There was no chemistry involved; the dye was always *on* and acted as a tracer. The absorption coefficient of a dye concentration of $10^{-5}M$, needed for data processing (Appendix C), was measured

to be about 0.16 cm^{-1} (Figure A.1). Data of Figure A.1 were obtained by measuring the fluorescence intensity due to a uniform dye concentration along the laser beam by a photodiode array (see Appendix B). The fluorescence intensity along the beam is proportional to the laser intensity for a uniform C_d (see equation A.2).

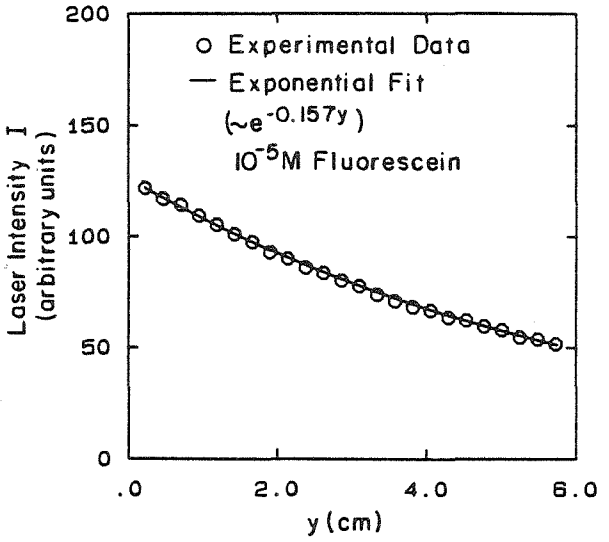

Figure A.1 Beam Attenuation by the Dye

In the chemically reacting experiments, the dye was always premixed with the acid solution so that the fluorescence was *off*. The absorption coefficient of a $10^{-5}M$ dye solution in the *off* condition was measured to be less than 0.01 cm^{-1}. The volume of base, v_b, required to titrate a unit volume, v_a, of the acid/dye solution and cross the pH threshold for fluorescence could be adjusted by the proper choice of the acid and base concentrations. Figure A.2 illustrates the measured fluorescence from the titration of a fixed volume of acid/dye solution. The fluorescence intensity is close to zero at the beginning as the solution is very acidic. As the base is added a point is reached where the pH threshold is crossed and the fluorescence " turns on ". Beyond this mixture ratio (in this case $v_b/v_a = 1/10$), addition of more base merely dilutes the dye. Now the

fluorescence intensity is only proportional to the dye concentration and hence proportional to the acid volume fraction. Note that the fluorescence *on/off* transition can be made very sharp. This transition is reversible in the sense that the fluorescence intensity can be switched *on* and *off* by adding sufficient amounts of base or acid required to cross the pH threshold.

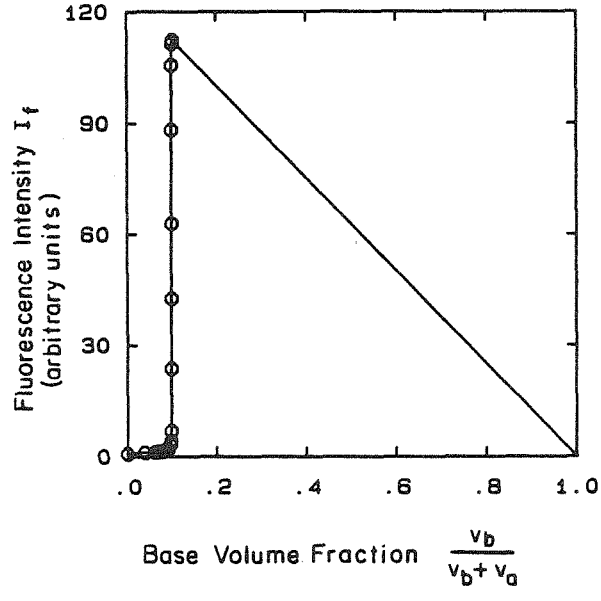

Figure A.2 Fluorescence Intensity vs. Base Volume Fraction

A.3. Chemistry and Time Scales

The chemical reaction used was an acid-base reaction between sulfuric acid (H_2SO_4) and sodium hydroxide ($NaOH$). In acidic solutions, positive florescein ions show very little fluorescence, whereas the negative ions formed in basic solutions exhibit very strong yellow-green fluorescence. The overall reaction can be symbolically written as

$$\text{Fluorescein} + (OH)^- \rightarrow \text{fluorescing product}$$

The association is made that the fluorescence intensity is proportional to the

product concentration C_p (see Appendix D for more detail). This reaction is reversible. The visible fluorescing product can be rendered invisible (i.e. no product) by the change in the local chemical environment. Note, however, that the effect of reversibility is contained in the titration curve of the experiment (for example Figure A.2) in that there is no fluorescence in certain range of mixture composition.

The acid-base reaction is a diffusion-controlled reaction. The rate constant k for combination of H^+ and OH^- ions in solution is $1.3 \times 10^{11}\ M^{-1}\ sec^{-1}$ at 23°C as quoted by Laidler & Meiser (1982). Recent measurements of Gutman et al. (1983) give a range of 18×10^{10} to $1 \times 10^{10}\ M^{-1}\ sec^{-1}$ for k. If we define the chemical time based on the reactant of lowest concentration, then

$$\tau_{chem} \approx \frac{1}{k\ [acid]} \approx 13\ nsec$$

for $0.0075M\ H_2SO_4$ and $k = 1 \times 10^{10}\ M^{-1}\ sec^{-1}$. The time scale for fluorescence is typically a few nanoseconds. Becker (1969) quotes an observed fluorescence life time of $4\ nsec$ for fluorescein. The overall time scale of the reaction is, therefore, dominated by τ_{chem}.

The large scale mixing time, τ_δ, is given by

$$\tau_\delta \approx \frac{\delta}{\Delta U}$$

where δ is the vorticity thickness and $\Delta U = U_1 - U_2$ the velocity difference across the shear layer. The relevant small scale mixing time, τ_{λ_D}, is the time to diffuse across the diffusion scale, λ_D, and is given by

$$\tau_{\lambda_D} \approx \frac{\lambda_D^2}{D} \approx \tau_\delta\, \mathrm{Re}^{-\frac{1}{2}}$$

where D is the mass diffusion coefficient. Note that τ_{λ_ν}, the time to diffuse across the viscous scale (Kolmogorov scale), λ_ν, is given by

$$\tau_{\lambda_\nu} \approx \frac{\lambda_\nu^2}{D} \approx \tau_\delta \, Sc \, \mathrm{Re}^{-\frac{1}{2}}$$

where $Sc = \frac{\nu}{D}$ is the Schmidt number. In the case of gases where Sc is of order unity, τ_{λ_D} and τ_{λ_ν} become essentially identical. For liquids which are characterized by large Sc, the distinction, however, becomes important. The shortest time scales during these experiments were

$$\tau_\delta \approx 10 \, msec$$

$$\tau_{\lambda_D} \approx 50 \, \mu sec .$$

The Damkohler number is the ratio of the mixing to the chemical time. Thus,

$$\tau_\delta / \tau_{chem} \approx 7.7 \times 10^5 \quad \text{for the large scales}$$

and

$$\tau_{\lambda_D} / \tau_{chem} \approx 260 \quad \text{for the small scales}$$

The chemistry is therefore rapid compared to the relevant mixing times.

A.3.1. *Buoyancy and Heat Release.* The densities of the two free streams of the shear layer can be unequal due to addition of acid and base. When deemed necessary, sodium sulfate (Na_2SO_4) was added to the acid/dye solution in order to match the densities. The density difference in these experiments was

$$0.0002 < \Delta\rho/\bar{\rho} < 0.004$$

where $\Delta\rho = \rho_1 - \rho_2$ and $\bar{\rho} = (\rho_1 + \rho_2)/2$.

The effect of buoyancy can be discussed in terms of the Richardson number, Ri, defined by

$$Ri = \frac{\Delta\rho\, g\, \delta}{\bar{\rho}\,(\Delta U)^2}$$

where g is the gravitational acceleration, δ the vorticity thickness, and $\Delta U = U_1 - U_2$. Koop & Browand (1979) found that for $Ri < 0.05$, based on δ at a downstream distance $x = 1\,cm$, the effect of buoyancy became negligible. Our largest Ri was 0.0005 and buoyancy effects could be neglected.

The maximum temperature rise due to the acid-base reaction was estimated to be about 0.5°C for the concentration of chemicals used. This chemical reaction could, therefore, be considered isothermal.

A.4. Thermal Blooming and Photobleaching

Thermal blooming is caused by the localized heating of the dye solution by the laser beam. The index of refraction gradients produced in this way act as a lens causing the laser beam to diverge rapidly, leading to a significant decrease in the fluorescence intensity.

Continuous excitation of organic dyes causes the dye to lose its absorption efficiency over time. The incapacitated (bleached) dye molecules do not absorb and the net effect is as if the dye is simply diluted. The number of active (absorbing) dye molecules, n, as a function of time, is given by

$$n = n_0\, e^{-t/\tau_b}$$

where n_0 is the number of dye molecules at $t = 0$ and

$$\tau_b^{-1} = Q_b \Phi \sigma$$

where

Q_b = bleaching quantum efficiency (probability that a dye molecule will be bleached with the absorption of a single photon)

Φ = laser photon flux

σ = dye absorption cross section

For these experiments $\tau_b \approx 20\ sec$ based on $Q_b = 4 \times 10^{-6}$ (Ippen et al. 1971), $\Phi = 5 \times 10^{20}\ photons/cm^2/sec$, corresponding to 200 $watts/cm^2$ power density at 5145 Å and $\sigma = 0.25 \times 10^{-16} cm^2$ (calculated from attenuation of $10^{-5}\ M$ dye). Note that photobleaching can be very serious for nonflowing systems. Only 37% of molecules will be absorbing after 20 seconds.

Problems of thermal blooming and photobleaching can be alleviated in a flowing system naturally provided by the experiment. The flow system provides rapid removal of heat from the path of the beam and eliminates the blooming problem. Bleaching is overcome if the flow transit time through the beam is much smaller than τ_b. The worst case encountered was $t/\tau_b \approx 5 \times 10^{-4}$. In the titration experiments, which were done in a flowing system with a fixed amount of dye, bleaching was minimized by making the volume of the titration chamber much larger than the volume covered by the beam and continuously circulating the fluid. This precaution resulted in an estimated bleaching loss of 0.5% per hour.

Appendix B

PHOTODIODE ARRAY AND ADC BOARD

Acquisition of fluoresence intensity data was accomplished by a self-scanning linear photodiode array, available from Reticon Corporation, and a very high speed A/D system (ADC board). General characteristics of these two devices are described in this section. More detailed information on Reticon arrays can be found in the Reticon literature and the article by Horlick (1976). Permission to reprint " G " Series, solid state line scanner, data contained in section has been given by EG&G Reticon, (Copyright 1980).

B.1. Reticon Array

The *RL-1024G* array consists of a row of 1024 silicon photodiodes on 25 μm centers. The bar-shaped photodiodes have a photo-sensitive area of 15 μm x 26 μm. Photograph of such an array is shown on Figure B.1. Also shown is the aperture geometry along with an idealized response function which would be obtained by scanning a point source of light along the length of the array.

Photodiodes operate in the charge storage mode and hence are inherently integrating type detectors. Each element (or pixel) of the array has an associated storage capacitor on which to integrate the photocurrent and a multiplex switch for periodic readout via an integrated shift register scanning circuit. A single phase TTL clock drives the scanning circuitry, which is also available from Reticon. During the integration time (or scan time), defined by clock period x number of elements in the array, charge is accumulated by the photocurrent. Since the photocurrent is linearly proportional to the light intensity,

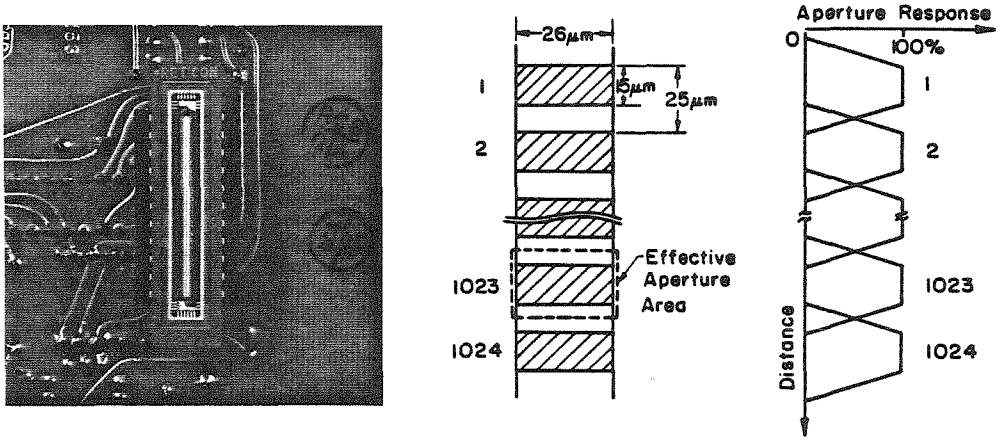

Figure B.1 *RL-1024G* Array, Sensor Geometry and Idealized Aperture Response Function

the charge output of each photodiode (below saturation) is proporational to the light intensity received during the scan time. This array has a typical ± 12% sensitivity nonuniformity which is removable in the subsequent data processing (Appendix C).

B.1.1. *Dynamic Range.* The dynamic range of the array is determined by the dark noise. The contribution from the photon shot noise is negligible (see Appendix C). When the array is in the dark, the output is caused by two main sources. The first source is the integrated dark leakage current produced by thermally generated charge carriers. The dark current increases with temperature and scan time. Generally, a scan time longer than 40 *msec* is not recommended. The longest scan time used in these experiments was 2 *msec* and no attempt was made to decrease the noise by cooling the array. The second source is a fixed pattern noise caused by incomplete cancellation of clock switching transients. This can be removed in processing as discussed in Appendix C. The overall dynamic range, defined by the ratio of the saturation voltage to the peak-to-peak dark noise voltage, was about 200.

B.1.2. *Resolution.* Each pixel receives light from an area in the object plane

that is determined by the effective aperture of the pixel and the magnification ratio of the collecting optics. This area defines the spatial resolution if it is smaller than the area illuminated by the laser beam. If we define the effective aperture of a pixel by the area $25\mu m \times 26\mu m$ (see Figure B.1), the resolution area becomes $\Delta x \times \Delta y = 100\mu m \times 104\mu m$ for a typical magnification ratio of 1/4 in these experiments. The beam diameter was in the range 0.5 to 1 mm. This diameter determines the resolution in the third dimension Δz. See figure below.

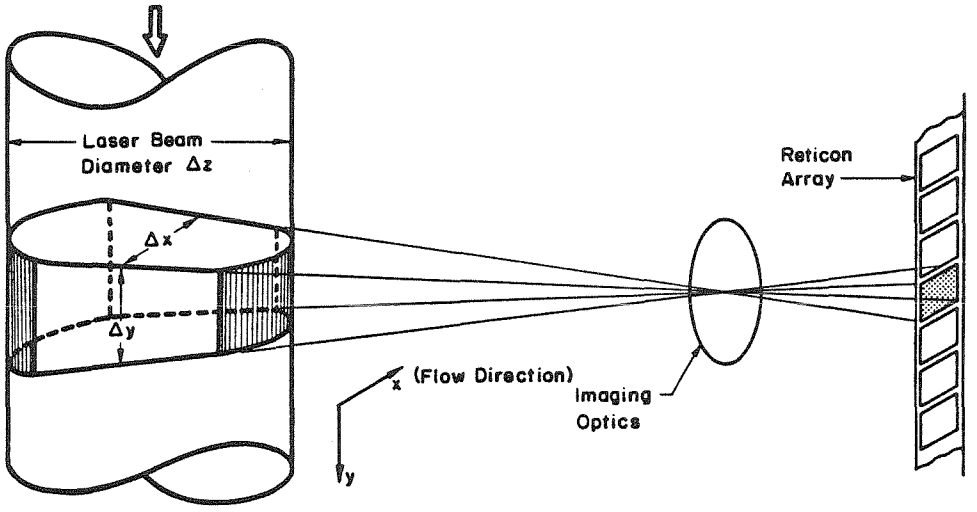

Figure B.2 Schematic of Focussing Arrangement

The discussion above is applicable to static conditions. In a flowing system, the resolution along the flow direction, Δx, is determined by the distance the flow moves during the scan time. This distance could be considerably longer than the static resolution depending on the scan time and the flow speed. The actual dynamic resolution in each experiment is discussed in the main text.

B.2. ADC Board

The ADC board is a unique single channel A/D conversion system capable of performing 8-bit conversions at a rate of up to 10 *MHz*. The design of this system began in 1979 by P.E. Dimotakis and D.B. Lang. It was completed and the system fabricated and tested by D. Kerns in 1982. The present experiments mark the debut of this device.

This board is based on the *TRW TDC1007J* 8-bit A/D flash converter. It features programmable gain, offset, clock frequency, delay and front end real-time data processing capabilities to reduce the transfer rate of the computer bus. The ADC board can gather high speed data from a variety of devices. It is especially designed, however, to accommodate linear and two-dimensional photodiode arrays.

The A/D system communicates with a DEC Q-bus through a synchronous device bus (D-bus) and a direct memory access (DMA) interface. The D-bus is capable of 12 *Mbytes/sec* data rate and was designed by D.B. Lang and P.E. Dimotakis. The DMA interface can handle a data rate of 1.2 *Mbytes/sec*. At present we can sustain this rate only by silencing all other devices on the computer bus. This limits the total amount of data acquired to about 200,000 bytes (equal to the system memory) per run. Large amounts of data can be presently acquired, however, and transferred to a high speed (1 *Mbyte/sec*, Winchester) disk, continuously, at a rate of 300 *Kbytes/sec*.

Appendix C

DATA REDUCTION

C.1. Getting the Correct Dye Concentration

The output of the i^{th} pixel, in response to the fluorescence intensity at point y_i along the beam, may be written as

$$V(i) = R(i)\,\eta\,\frac{\Omega(i)}{4\pi}\,T_s\,I_f(i) + \begin{bmatrix}\text{photon}\\ \text{shot noise}\end{bmatrix} + D(i) \qquad \text{(C.1)}$$

where

$V(i)$ = output voltage

$R(i)$ = pixel sensitivity ($Volt/Joule/cm^2$)

η = optics collection efficiency

$\Omega(i)$ = subtended solid angle

T_s = array scan time

$I_f(i)$ = fluorescence intensity issued from point y_i, given by equation (A.2)

$D(i)$ = dark response

The typical maximum signal amplitude in the present experiments, for the scan times used, corresponded to about 6.5×10^6 photons. The photon shot noise can, therefore, be neglected.

The laser intensity is not uniform along the beam and, at a point y_i, can be written as

$$I(i) = I_o(i)\, e^{-\varepsilon_o \int_1^i C_d\, dy} \tag{C.2}$$

where

I = laser intensity

I_o = laser intensity in the absence of attenuation

ε_o = dye molar absorption coefficient

C_d = local molar dye concentration

The first term is the laser intensity variation established by the focusing lens. The second term accounts for the cumulative absorption.

Combining equations (A.2), (C.1) and (C.2) and lumping all the parameters that are independent of the dye concentration into a single term, $\beta(i)$, we get

$$V(i) = \beta(i)\, e^{-\varepsilon_o \int_1^i C_d\, dy}\; C_d(i) + D(i) \tag{C.3}$$

$\beta(i)$ contains the effects of nonuniformity of imaging and pixel sensitivity, laser beam shape and even slight misalignment of the array with the beam. It is experimentally measured by recording the fluorescence intensity along the beam resulting from a very dilute uniform dye solution in the test section. $D(i)$ is measured by recording the output of the array with the test section filled with clear water (i.e. no dye present). Making the following approximation

$$\int_i^{i+1} C_d\, dy \approx \Delta y\; C_d(i)$$

reduces equation (C.3) to

$$C_d(i) = \prod_{j=1}^{i-1} e^{\varepsilon_o \Delta y\, C_d(j)}\; \frac{V(i) - D(i)}{\beta(i)} \tag{C.4}$$

To get the dye concentration at a given point, the instantaneous laser intensity at that point must be known. The laser beam, however, attenuates in passing through the dye concentration field that is set up by the turbulent flow. As a result, the correct calculation of dye concentration requires the knowledge of the dye field that the beam has passed through to get to the point of interest so that the beam attenuation can be properly accounted for. One advantage of linear arrays now becomes apparent. Each scan of the array contains information at many closely spaced points along the beam essentially simultaneously. This, in effect, allows one to perform the operation indicated by equation (C.4) on the data, on the scan-by-scan basis, and remove the effects of attenuation and various nonuniformities. Data processed by equation (C.4) are on the correct relative scale.

C.2. Dilution Data

The local instantaneous dye concentration, C_d, in a sampling volume is given by

$$C_d = C_{d_o} \frac{v_2}{v_1 + v_2} \tag{C.5}$$

where

C_{d_o} = free stream dye concentration carried by the L.S. fluid

v_2 = volume of L.S. fluid in the sampling volume

v_1 = volume of H.S. fluid in the sampling volume

The normalized concentration of high speed fluid, ξ, is thus equal to

$$\xi = 1 - C_d / C_{d_o} \tag{C.6}$$

(see also Appendix D).

Equations (C.4) and (C.6) are the basis of calculation of local instantaneous concentration. Since the whole width of the shear layer was imaged on the array, C_{d_o} was available in each scan making calculation of equation (C.6) relatively easy. Even though the full equation (C.4) was used, the effect of attenuation turned out to be negligible because of the low dye concentration used in the dilution experiments.

C.3. Chemically Reacting Data

The local instantaneous product concentration, C_p, after the fluorescence threshold has been crossed, is given by (see Appendix D)

$$C_p = C_{d_o} \frac{\upsilon_a}{\upsilon_a + \upsilon_b} = C_d \tag{C.7}$$

where

C_{d_o} = free stream dye concentration carried by the acid solution

υ_a = volume of acid in the sampling volume

υ_b = volume of base in the sampling volume

C_d = dye concentration in the sampling volume

The maximum value of C_p, C_{p_s}, is reached at the threshold condition for fluorescence " turn-on ". The product concentration normalized by the maximum value, is therefore

$$\frac{C_p}{C_{p_s}} = \frac{C_d}{C_{p_s}} \tag{C.8}$$

Equations (C.4) and (C.8) are the basis of calculation of product concentration. The value of C_{p_s} was available in each scan in the titration-reference chamber which was also imaged on the array. The effect of beam attenuation accounted for about 10% of the total product in the worst case.

Appendix D

THE PDF

A major portion of these experiments deals with measuring the probability density function of the concentration field. The interest in the *pdf* stems from the fact that the classical approach to the solution of many problems of practical interest in chemically reacting flows requires the knowledge of the *pdf* for that flow. This approach is discussed in some detail by Bilger (1980).

This section serves to introduce definitions and properties of quantities frequently used in this work, and how they are related to the *pdf*.

D.1. General Considerations

The local instantaneous high speed fluid volume fraction, ξ, in a small sampling volume is given by

$$\xi \equiv \frac{v_1}{v_1 + v_2} \tag{D.1}$$

where

v_1 = volume of H.S. fluid in the sampling volume

v_2 = volume of L.S. fluid in the sampling volume

Note that ξ is the normalized concentration of high speed fluid. This definition is the same as that based on mass fraction for a constant density, incompressible flow. It is also consistent with the definition based on mole fraction, used by Mungal (1983), in the gaseous case.

The probability density function of ξ at a given point, y, in the layer is denoted by $p(\xi,y)$ and is the fraction of time that $\xi(t)$ falls inside the range $(\xi, \xi + \Delta\xi)$. Specifically,

$$p(\xi,y)\,\Delta\xi = \text{Prob}\left\{\xi < \xi(t) \leq \xi + \Delta\xi\right\} \tag{D.2}$$

for small $\Delta\xi$.

Normalization of the *pdf* requires that

$$\int_0^1 p(\xi,y)\,d\xi = 1 \tag{D.3}$$

The average concentration of high speed fluid, $\bar{\xi}$, is then given by

$$\bar{\xi}(y) = \int_0^1 \xi\, p(\xi,y)\,d\xi \tag{D.4}$$

Figure D.1 shows a typical $p(\xi,y)$.

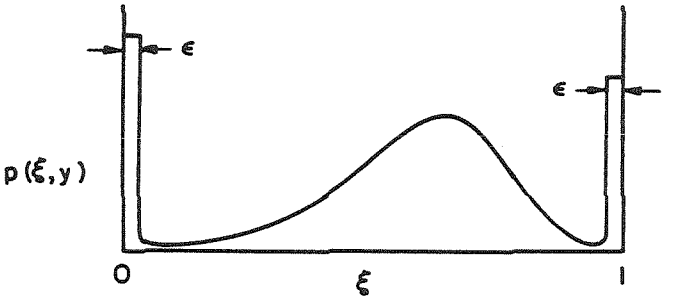

Figure D.1

The two delta functions at $\xi = 0$ and 1 are associated with the pure unmixed fluids of the L.S. and H.S. sides, respectively. Their widths are not zero in practice. Concentrations in the range $0 \leq \xi < \varepsilon$ are assigned to pure (unmixed) L.S. fluid and $1-\varepsilon < \xi \leq 1$ to pure H.S. fluid. The range $\varepsilon \leq \xi \leq 1-\varepsilon$ would, therefore, correspond to mixed fluid. The maximum value of ε used was 0.031. The mixed fluid *pdf* (i.e. excluding the two delta functions) may be characterized

by its area and first moment as defined below.

The area under the mixed fluid *pdf*, P, gives the total probability of finding mixed fluid at *any* concentration. It is given by

$$P(y) = \int_{\varepsilon}^{1-\varepsilon} p(\xi, y)\, d\xi \tag{D.5}$$

This quantity was called intermittency by Konrad (1976). Here, however, no attempt is made to relate mixing regions to turbulent-nonturbulent regions. A value of $P(y)$ less than unity signifies the presence of unmixed fluid.

The first moment of $p(\xi, y)$, otherwise known as the average mixed fluid concentration, is given by

$$C_m(y) = \frac{\int_{\varepsilon}^{1-\varepsilon} \xi\, p(\xi, y)\, d\xi}{\int_{\varepsilon}^{1-\varepsilon} p(\xi, y)\, d\xi} \tag{D.6a}$$

$$= \frac{\int_{\varepsilon}^{1-\varepsilon} \xi\, p(\xi, y)\, d\xi}{P(y)} \tag{D.6b}$$

It is useful to define an average mixed fluid *pdf*, $\bar{p}(\xi)$, that represents the whole layer. We define it by

$$\bar{p}(\xi) = \frac{1}{y_1 - y_2} \int_{y_2}^{y_1} p(\xi, y)\, dy \tag{D.7}$$

y_1 and y_2 would ideally correspond to the high speed and low speed edges of the mixing layer respectively. In some cases, however, measurement of the *pdf* was not available all the way out to the edges of the layer. As a compromise, y_1 and y_2 were chosen to be the points on the high speed and low speed sides of the layer, respectively, where the total mixed fluid probability P (see equation D.5) had dropped to 35% of its maximum value. The distance between these two

points corresponded to approximately 63% of the visual width of the layer.

And finally, a very important quantity, the total mean mixed fluid concentration in the layer, C_M, is defined by

$$C_M = \frac{\int_{-\infty}^{+\infty} P(y)\, C_m(y)\, dy}{\int_{-\infty}^{+\infty} P(y)\, dy} \tag{D.8}$$

D.2. Calculation of Product from the PDF

Consider a small sampling volume at a point in a mixing layer where the instantaneous high speed fluid volume fraction, ξ, has been measured by some means. Suppose that the partial volumes v_1 and v_2 contain n_A and n_B moles of dilute reactants A and B respectively. We define

$$C_{1o} \equiv \frac{n_A}{v_1} \tag{D.9a}$$

$$C_{2o} \equiv \frac{n_B}{v_2} \tag{D.9b}$$

to be the free stream molar concentrations of the H.S. and L.S. sides respectively. Now consider a one-step, fast and irreversible reaction of the type

$$A + B \rightarrow P$$

with unity molar stoichiometric coefficients. We define the equivalence ratio, φ, by

$$\varphi \equiv \frac{(C_{2o} / C_{1o})}{(C_{2o} / C_{1o})_s} = \frac{C_{2o}}{C_{1o}} \tag{D.10}$$

since the stoichiometric molar concentration ratio $(C_{2o} / C_{1o})_s$, for the reaction considered, equals unity. See also Mungal (1983) for a discussion of this choice

of definition for the equivalence ratio instead of the more conventional definition based on mass fractions which is used in combustion research.

Measuring a particular value of ξ implies that n_A moles of A and n_B moles of B are present in the sampling volume. If A and B react to completion, the reactant in short supply will be consumed. Thus, as a result of an irreversible reaction, the concentration of product, C_p, is given by

$$C_p = \begin{cases} \dfrac{n_A}{v_1 + v_2} = C_{1o}\,\xi & \text{for } n_A < n_B \\ \dfrac{n_B}{v_1 + v_2} = C_{2o}\,(1-\xi) & \text{for } n_B < n_A \end{cases} \tag{D.11}$$

The stoichiometric condition occurs at $n_A = n_B$. In this case

$$C_{1o}\,\xi_s = C_{2o}\,(1-\xi_s)$$

$$\xi_s = \frac{C_{2o}}{C_{1o} + C_{2o}} = \frac{\varphi}{1+\varphi} \tag{D.12}$$

and the maximum product concentration is given by

$$C_{p_s} = C_{1o}\,\frac{\varphi}{1+\varphi} = C_{2o}\,\frac{1}{1+\varphi} \tag{D.13}$$

$C_p(\xi)$ is determined by φ. To explicitly indicate this, we rewrite equation (D.11) in the following form

$$C_p(\xi;\varphi) = \begin{cases} C_{1o}\,\xi & \text{for } \xi < \dfrac{\varphi}{1+\varphi} \\ C_{2o}\,(1-\xi) & \text{for } \xi > \dfrac{\varphi}{1+\varphi} \end{cases} \tag{D.14}$$

A sketch of $C_p(\xi;\varphi)$ is shown in Figure D.2.

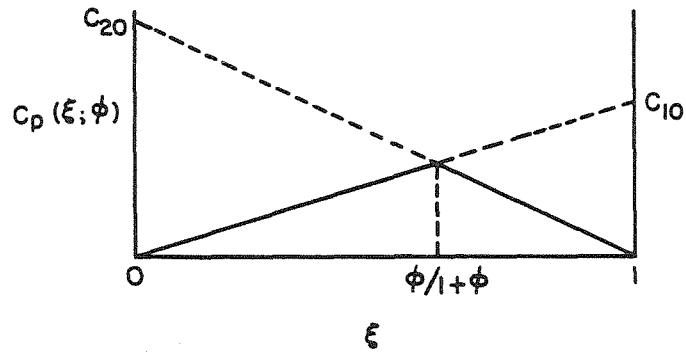

Figure D.2

The average production concentration for a given φ at position y, $\overline{C_p}(y;\varphi)$, is given by

$$\overline{C_p}(y;\varphi) = \int_0^1 C_p(\xi;\varphi)\, p(\xi,y)\, d\xi \qquad \text{(D.15a)}$$

To be consistent with earlier definitions in § D.1, in handling the nonzero width of free stream delta functions, the equation above has been used in the form

$$\overline{C_p}(y;\varphi) = \int_\varepsilon^{1-\varepsilon} C_p(\xi;\varphi)\, p(\xi,y)\, d\xi \qquad \text{(D.15b)}$$

There is no controversy in using equation (D.15b) in place of (D.15a) since free stream delta functions do not contribute to product.

It is customary to represent the total amount of product in the layer by the product thickness. Mungal (1983) pointed out the importance of the choice of the free stream concentration used for normalization. Two product thicknesses can be defined by

$$\delta_{p_1}(\varphi) = \frac{1}{C_{1\sigma}} \int_{-\infty}^{+\infty} \overline{C_p}(y;\varphi)\, dy \qquad \text{(D.16a)}$$

$$\delta_{p_2}(\varphi) = \frac{1}{C_{2o}} \int_{-\infty}^{+\infty} \overline{C_p}(y\,;\varphi)\, dy \qquad \text{(D.16b)}$$

As long as the fluid mechanics of the flow is unaffected by the chemical reactions (e.g. low heat release), the *pdf* of the nonreacting flow may be used to predict the amount of product in the reacting case through equations (D.15) and (D.16). Then, fluid mechanics and mixing determine the *pdf*, $p(\xi, y)$, and chemistry determines the dependence of product concentration on composition namely $C_p(\xi\,;\varphi)$. $C_p(\xi\,;\varphi)$ would be proportional to the temperature rise due to heat release in the case of combustion, and the fluorescence intensity in the case of LIF chemically reacting experiments.

Before we leave this section, it should be pointed out that the total mixed fluid probability, $P(y)$, the average mixed fluid concentration, $C_m(y)$, and the total mean mixed fluid concentration, C_M, can be related to the average product at large and small φ's. In these limits we have

$$\begin{aligned} C_p(\xi\,;\infty) &= C_{1o}\,\xi \qquad \text{for } \varphi \to \infty \\ C_p(\xi\,;0) &= C_{2o}\,(1-\xi) \qquad \text{for } \varphi \to 0 \end{aligned}$$

which result in the following relations

$$P(y) = \frac{\overline{C_p}(y\,;\infty)}{C_{1o}} + \frac{\overline{C_p}(y\,;0)}{C_{2o}} \qquad \text{(D.17)}$$

$$C_m(y) = \frac{\overline{C_p}(y\,;\infty)/C_{1o}}{\overline{C_p}(y\,;\infty)/C_{1o} + \overline{C_p}(y\,;0)/C_{2o}} \qquad \text{(D.18)}$$

$$C_M = \frac{\delta_{p_1}(\infty)}{\delta_{p_1}(\infty) + \delta_{p_2}(0)} \qquad \text{(D.19)}$$

D.2.1. *Product Concentration in LIF Experiments.* Discussion of § A.2 indicates that

$$\text{fluorescence intensity} = \begin{cases} 0 & \text{for } \dfrac{v_b}{v_a + v_b} < \left(\dfrac{v_b}{v_a + v_b}\right)_{thr} \\ C_{d_o}\left(1 - \dfrac{v_b}{v_a + v_b}\right) & \text{for } \dfrac{v_b}{v_a + v_b} > \left(\dfrac{v_b}{v_a + v_b}\right)_{thr} \end{cases} \tag{D.20}$$

where

v_a = volume of acid/dye solution

v_b = volume of base solution

C_{d_o} = free stream dye concentration, premixed with the acid solution

$\left(\dfrac{v_b}{v_a + v_b}\right)_{thr}$ = base volume fraction at the threshold condition for fluorescence turn-on

The product in these experiments is the fluorescence intensity. Two cases can be defined, depending on which chemical is on the high speed side, as follows :

a) base on the H.S., acid/dye on the L.S. side

$$C_p(\xi;\varphi) = \begin{cases} 0 & \text{for } \xi < \dfrac{\varphi}{1+\varphi} \\ C_{d_o}(1-\xi) & \text{for } \xi > \dfrac{\varphi}{1+\varphi} \end{cases} \tag{D.21a}$$

where

$$\frac{\varphi}{1+\varphi} = \left(\frac{v_b}{v_a + v_b}\right)_{thr} \tag{D.21b}$$

or

$$\varphi = \left[\frac{v_b}{v_a}\right]_{thr} \tag{D.21c}$$

b) base on the L.S., acid/dye on the H.S. side

$$C_p(\xi;\varphi) = \begin{cases} C_{d_o}\,\xi & \text{for } \xi < \dfrac{\varphi}{1+\varphi} \\ 0 & \text{for } \xi > \dfrac{\varphi}{1+\varphi} \end{cases} \tag{D.22a}$$

where

$$\frac{\varphi}{1+\varphi} = 1 - \left[\frac{v_b}{v_a + v_b}\right]_{thr} = \left[\frac{v_a}{v_a + v_b}\right]_{thr} \tag{D.22b}$$

or

$$\varphi = \left[\frac{v_a}{v_b}\right]_{thr} \tag{D.22c}$$

Comparing equations (D.21a) and (D.22a) with (D.14) shows that the product concentrations are identical in form with one exception. The product concentration in the LIF experiments is a " one-sided " triangle. This, of course, is the consequence of the chemical environment requirements for fluorescence. A sketch of C_p for the two cases discussed is shown below.

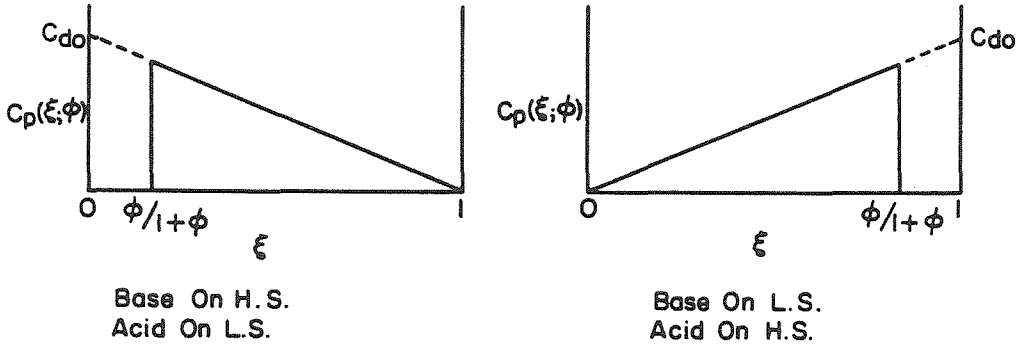

Figure D.3

References

BATT, R. G. 1977 Turbulent mixing of passive and chemically reacting species in a low-speed shear layer. *J. Fluid Mech.* **82**, 53-95.

BECKER, R. S. 1969 *Theory and Interpretation of Fluorescence and Phosphorescence*. Wiley Interscience, 85.

BERNAL, L. P. 1981 The coherent structure of turbulent mixing layers : I. Similarity of the primary vortex structure. II. Secondary streamwise vortex structure. Ph.D. thesis, Caltech.

BILGER, R. W. 1980 Turbulent flows with nonpremixed reactants. In *Turbulent Reacting Flows* (P. A. Libby & F. A. Williams, Eds.), Topics in Applied Physics, **44**, Springer-Verlag, 65-113.

BREIDENTHAL, R. E. 1978 A chemically reacting, turbulent shear layer. Ph.D. thesis, Caltech.

BREIDENTHAL, R. E. 1981 Structure in turbulent mixing layers and wakes using a chemical reaction. *J. Fluid Mech.* **109**, 1-24.

BROADWELL, J. E. & BREIDENTHAL, R. E. 1982 A simple model of mixing and chemical reaction in a turbulent shear layer. *J. Fluid Mech.* **125**, 397-410.

BROWN, G. L. 1974 The entrainment and large structure in turbulent mixing layers. In *Proc. Fifth Australasian Conf. on Hydraulics and Fluid Mechanics*, 352-359.

BROWN, G. L. & REBOLLO, M. R. 1972 A small, fast response probe to measure composition of a binary gas mixture. *AIAA J.* **10(5)**, 649-652.

BROWN, G. L. & ROSHKO, A. 1974 On density effects and large structure in turbulent mixing layers. *J. Fluid Mech.* **64(4)**, 775-816.

BURKE, S. P. & SCHUMANN, T. E. W. 1928 Diffusion flames. *Ind. Eng. Chem.* **20**, 998-1006.

CORCOS, G. M. & SHERMAN, F. S. 1976 Vorticity concentration and the dynamics of unstable free shear layers. *J. Fluid Mech.* **73(2)**, 241-264.

DEWEY, C. F., Jr. .1976 Qualitative and quantitative flow field visualization utilizing laser-induced fluorescence. In *Proc. AGARD Conf. on Applications of Non-Intrusive Instrumentation in Fluid Flow Research*, **AGARD-CP-193**.

DIMOTAKIS, P. E. & BROWN, G. L. 1976 The mixing layer at high Reynolds number : large structure dynamics and entrainment. *J. Fluid Mech.* **78(3)**, 535-560.

DIMOTAKIS, P. E., DEBUSSY, F. D. & KOOCHESFAHANI, M. M. 1981 Particle streak velocity field measurements in a two-dimensional mixing layer. *Phys. Fluids* **24(6)**, 995-999.

DIMOTAKIS, P. E., MIAKE-LYE, R. C. & PAPANTONIOU, D. A. 1982 Structure and dynamics of round turbulent jets. *GALCIT Rep.* **FM82-01**; invited lecture, XV *International Symposium of Fluid Dynamics, Jachranka, Poland*, 7-12

September 1981.

DIMOTAKIS, P. E., BROADWELL, J. E. & HOWARD, R. D. 1983 Chemically reacting turbulent jets. *AIAA Paper* no. 83-0474, 21*st Aerospace Sciences Meeting, January* 1983.

EFFELSBERG, E. & PETERS, N. 1983 A composite model for the conserved scalar PDF. *COMBUSTION AND FLAME* **50**, 351-360.

FIEDLER, H. F. 1975 On turbulence structure and mixing mechanisms in free turbulent shear flows. In *Turbulent Mixing in Nonreactive and Reactive Flows, A Project SQUID Workshop*. Plenum Press, 381-410.

FREYMUTH, P. 1966 On transition in a separated laminar boundary layer. *J. Fluid Mech.* **25(4)**, 683-704.

GHARIB, M. 1983 The effect of flow oscillations on cavity drag, and a technique for their control. Ph.D. thesis, Caltech.

GUTMAN, M., NACHLIEL, E., GERSHON, E., GINGER, R. & PINE, E. 1983 pH Jump: kinetic analysis and determination of the diffusion-controlled rate constants. *J. Am. Chem. Soc.* **108(8)**, 2210-2216.

HAWTHORNE, W. R., WEDDELL, D. S. & HOTTEL, H. C. 1949 Mixing and combustion in turbulent gas jets. In *Proc. Third Symp. on Combustion, Flame and Explosion Phenomena*, 266-288, Williams & Wilkins.

HORLICK, G. 1976 Characteristics of photodiode arrays for spectrochemical measurements. *Appl. Spectosc.* **30(2)**, 113-123.

IPPEN, E. P., SHANK, C. V. & DIENES, A. 1971 Rapid photobleaching of organic laser dyes in continuously operated devices. *IEEE J. Quantum Electron.* **QE-7**, 178-179.

JIMENEZ, J. 1980 On the visual growth of a turbulent mixing layer. *J. Fluid Mech.* **96(3)**, 447-460.

KOLLMANN, W. & JANICKA, J. 1982 The probability density function of a passive scalar in turbulent shear flows. *Phys. Fluids* **25(10)**, 1755-1769.

KONRAD, J. H. 1976 An experimental investigation of mixing in two-dimensional turbulent shear flows with application to diffusion-limited chemical reactions. Ph.D. Thesis, Caltech; and *Project SQUID Tech. Rep.* **CIT-8-PU**.

KOOCHESFAHANI, M. M., DIMOTAKIS, P. E. & BROADWELL, J. E. 1983 Chemically reacting shear layers. *AIAA Paper* no. 83-0475, 21*st Aerospace Sciences Meeting, January* 1983.

KOOP, C. G. & BROWAND, F. K. 1979 Instability and turbulence in stratified fluid with shear. *J. Fluid Mech.* **93(1)**, 135-159.

KYCHAKOFF, G., HOWE, R. D., HANSON, R. K. & KNAPP, K. 1983 Flow visualization in combustion gases. *AIAA Paper* no. 83-0405, 21*st Aerospace Sciences Meeting, January* 1983.

LAIDLER, K. J. & MEISER, J. H. 1982 *Physical Chemistry.* The Benjamin/Cummings Publishing Co. Inc. 392.

LIU, H. T., LIN, J. T., DELISI, D. P. & ROBBEN, F. A. 1977 Application of a fluorescence technique to dye-concentration measurements in a turbulent jet. NBS Special Publication 484, In *Proc. Symp. on Flow in Open Channels and Closed Conduits held at NBS, Gaithersburg, MD, February* 1977.

MICHALKE, A. 1965 Vortex formation in a free boundary layer according to stability theory. *J. Fluid Mech.* **22(2)**, 371-383.

MICHALKE, A. 1965 On spatially growing disturbances in an inviscid shear layer. *J. Fluid Mech.* **23(3)**, 521-544.

MICHALKE, A. & FREYMUTH, P. 1966 The instability and the formation of vortices in a free boundary layer. In *Proc. AGARD Conf. on Separated Flows : Part 2*, **AGARD-CP-4**, 575-595.

MUNGAL, M. G. 1983 Experiments on mixing and combustion with low heat release in a turbulent shear flow. Ph.D. Thesis, Caltech.

MUNGAL, M. G., DIMOTAKIS, P. E. & BROADWELL, J. E. 1983 Turbulent mixing and combustion in a reacting shear layer. *AIAA Paper* no. 83-0473, 21*st Aerospace Sciences Meeting, January* 1983.

POPE, S. B. 1981 A Monte Carlo method for the PDF equations of turbulent reactive flow. *Combustion Science and Technology* **25**, 159-174.

PRINGSHEIM, P. 1949 *Fluorescence and Phosphorescence*. Interscience Publishers, Inc. 348.

RAJAGOPALAN, S. & ANTONIA, R. A. 1981 Properties of the large structure in a slightly heated turbulent mixing layer of a plane jet. *J. Fluid Mech.* **105**, 261-281.

RETICON 1980 G Series solid state line scanner data sheet.

ROBBEN, F. A., LIN, J. T., DELISI, D. P. & LIU, H. T. 1976 Feasibility study of a dye-fluorescence technique for measuring concentrations in fluids. *Flow Research Note* no. 91, Flow Research Company, Kent, Washington.

SREENIVASAN, K. R., TAVOULARIS, S. & CORRSIN, S. 1981 A test of gradient transport and its generalizations. In **Turbulent Shear Flows 3**, *Third International Symp. on Turbulent Shear Flows, September* 1981, Springer-Verlag, 96-112.

TOOR, H. L. 1962 Mass transfer in dilute turbulent and nonturbulent systems with rapid irreversible reactions and equal diffusivities. *AIChE J.* **8(1)**, 70-78.

WALKER, B. J. 1979 Turbulence model comparisons for shear layers and axisymmetric jets. *U. S. Army Missile Command Tech. Rep.* **RD-80-1**.

WALLACE, A. K. 1981 Experimental investigation of the effects of chemical heat release in the reacting turbulent plane shear layer. Ph.D. thesis, The University of Adelaide.

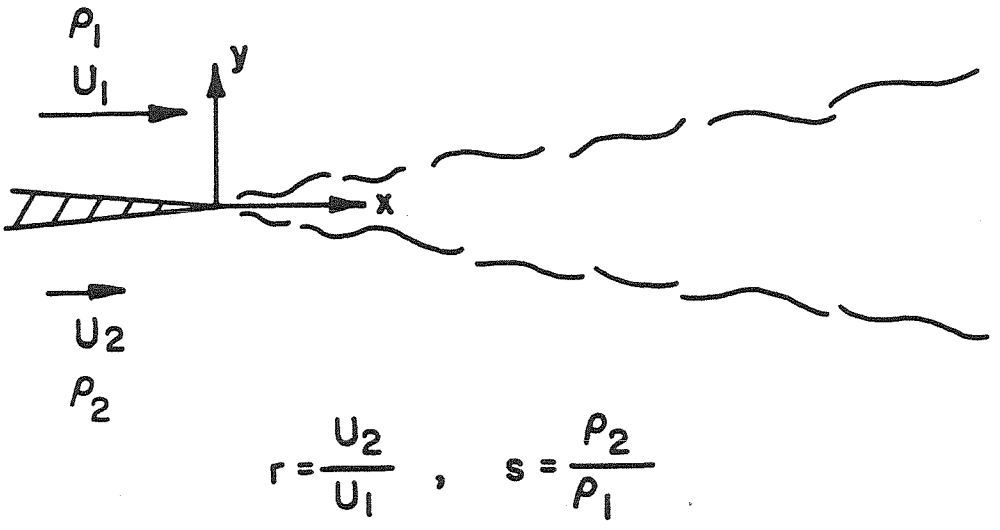

Figure 1 Mixing Layer Flow Geometry

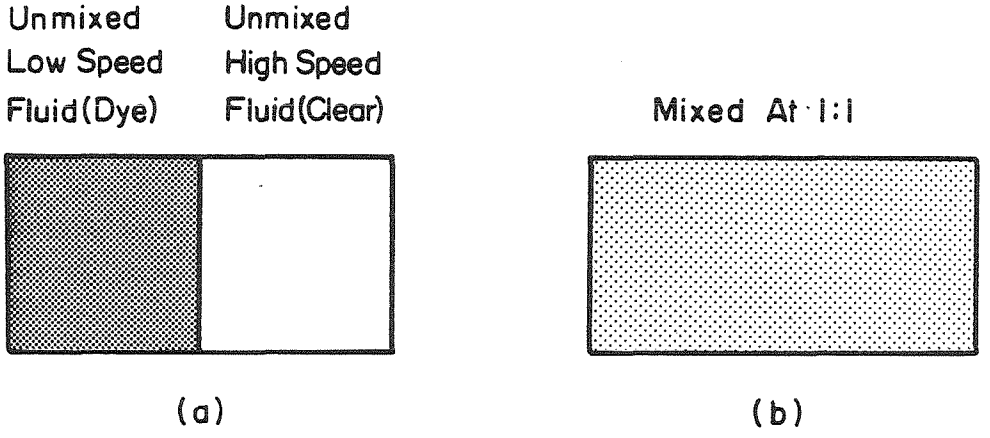

Figure 2 Problem of Finite Probe Sampling Volume

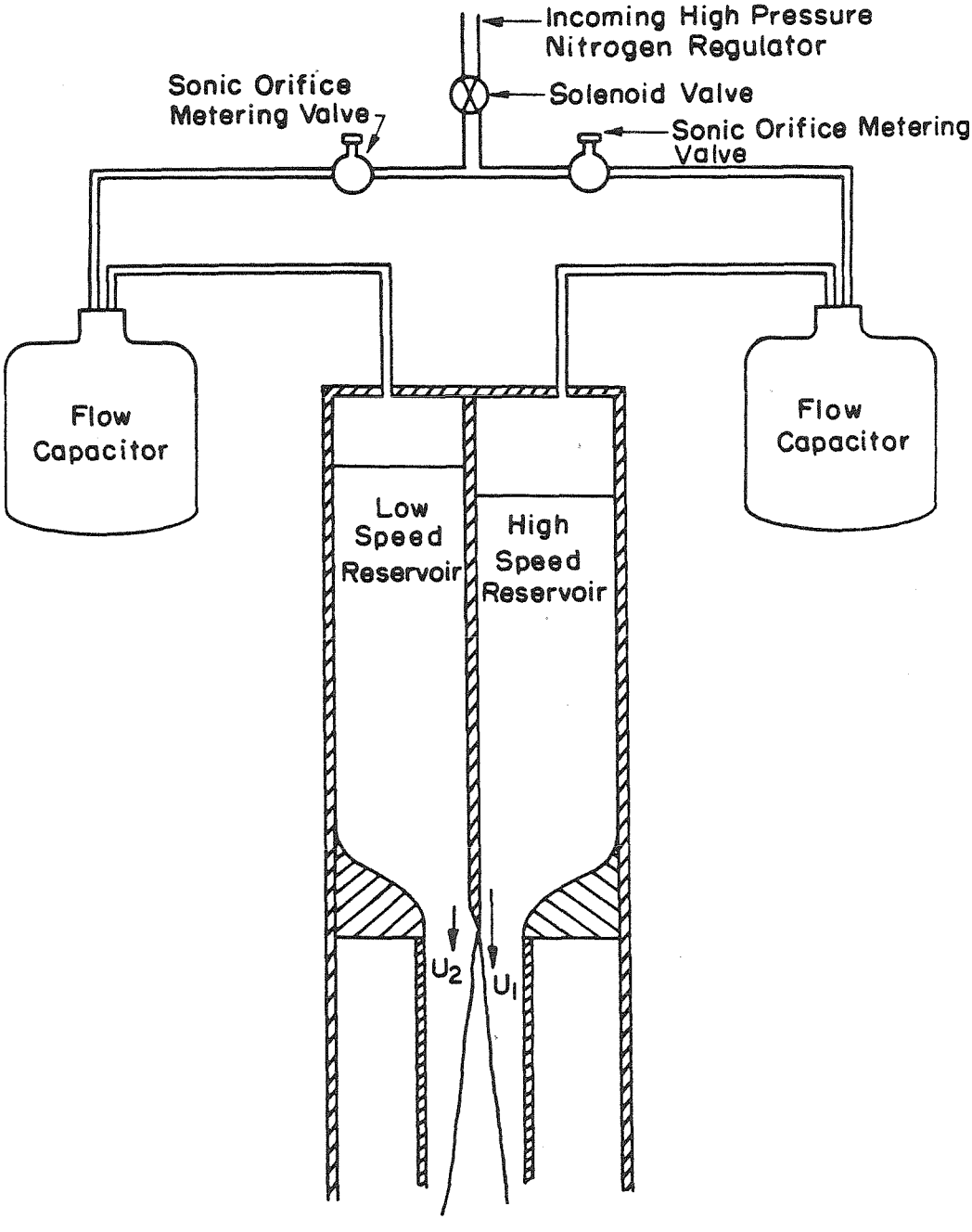

Figure 3 Flow Facility in Sheet Illumination Experiments

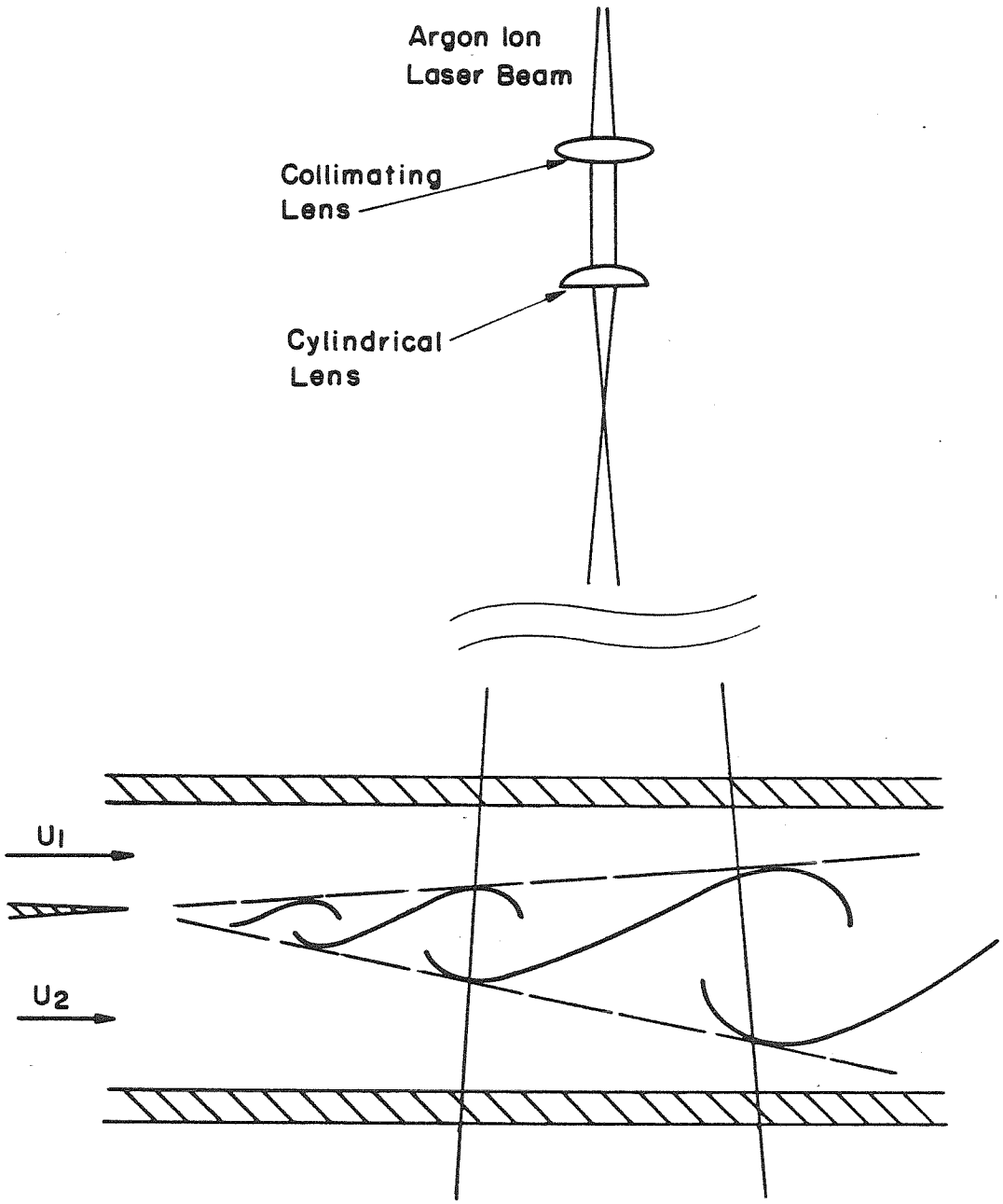

Figure 4 Sheet Illumination Optical Setup

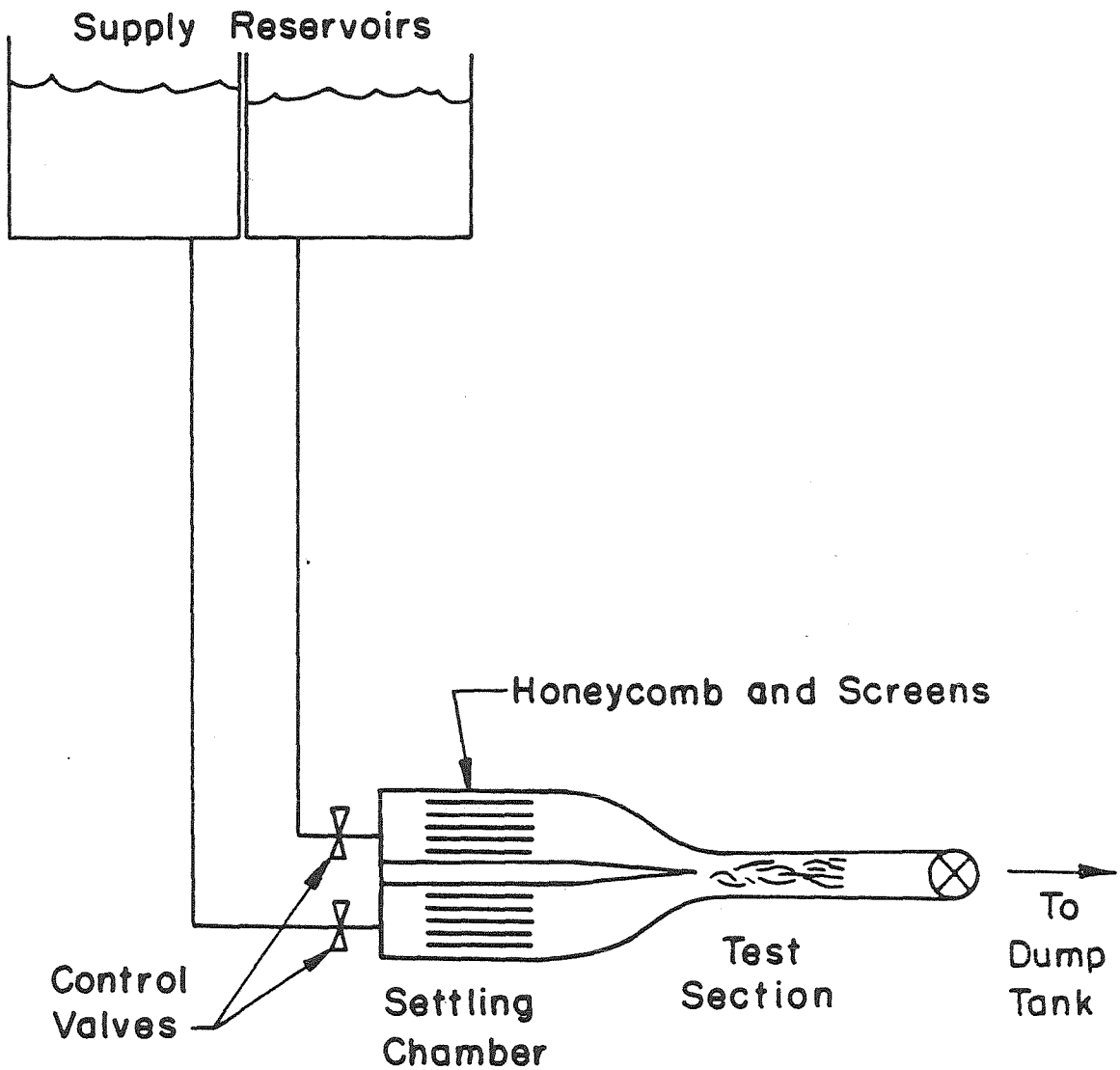

Figure 5 Flow Facility in Line Illumination Experiments

(Breidenthal's Apparatus)

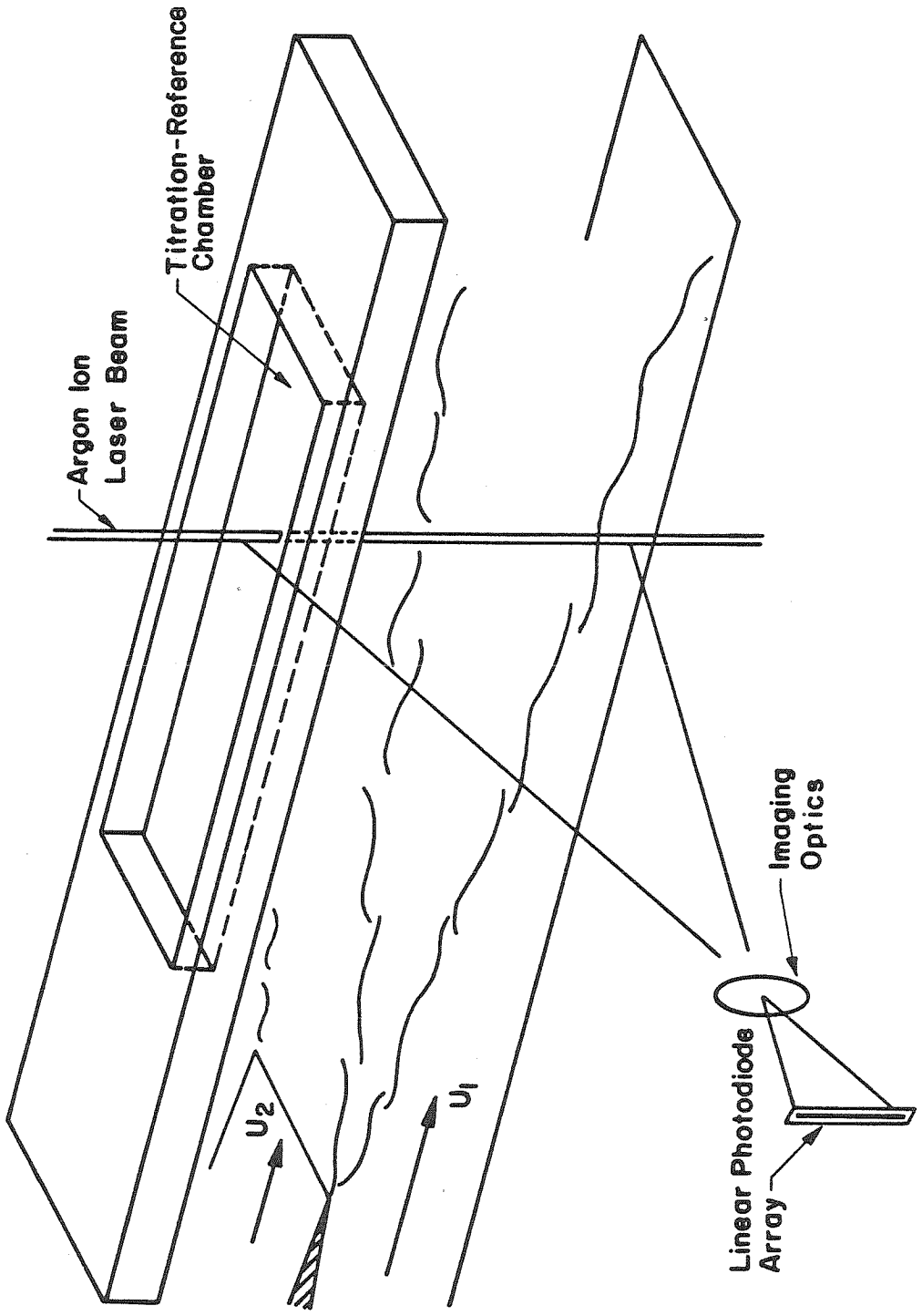

Figure 6 Line Illumination Optical Setup

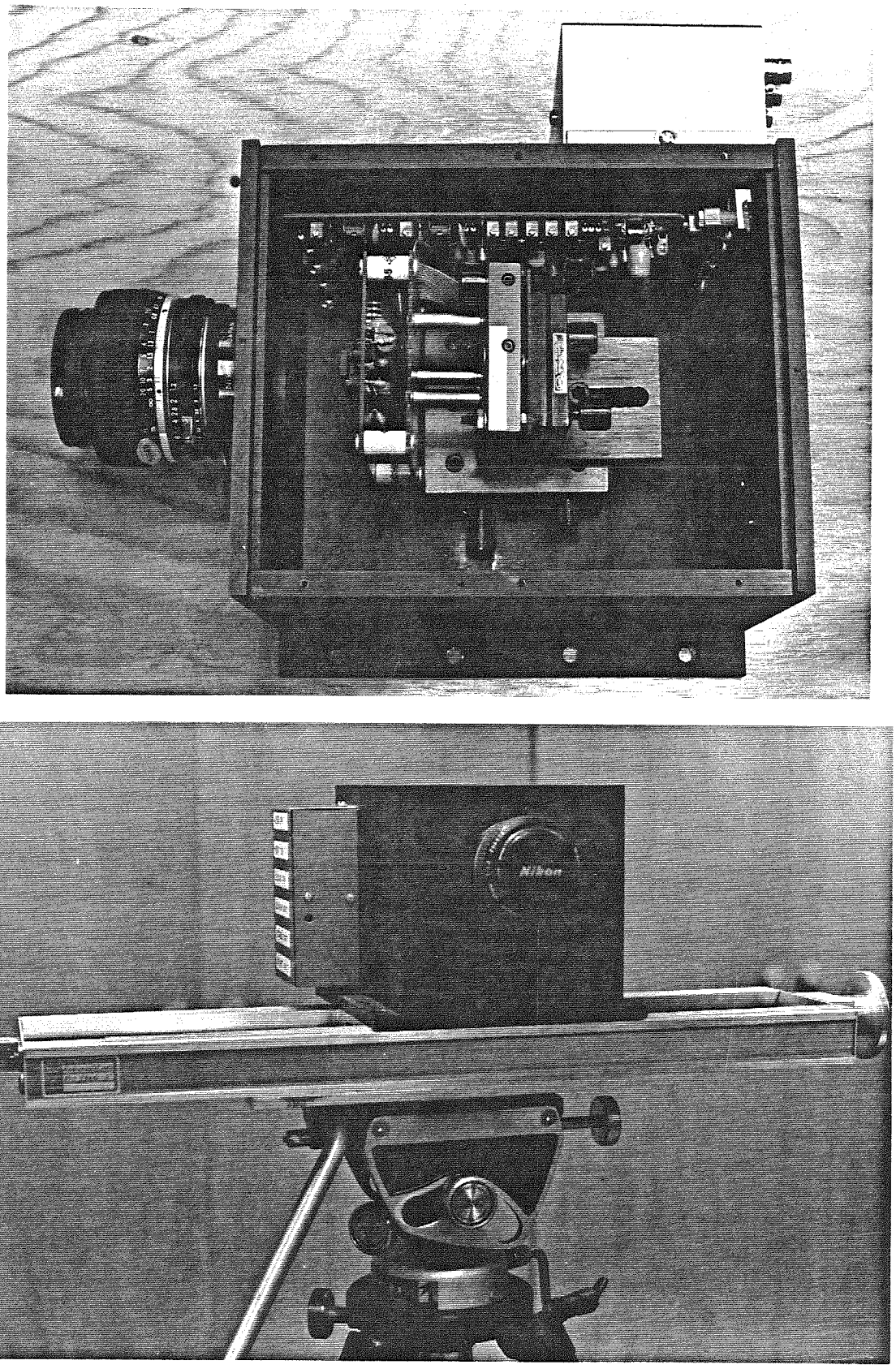

Figure 7 Inside and Outside Views of Reticon Camera

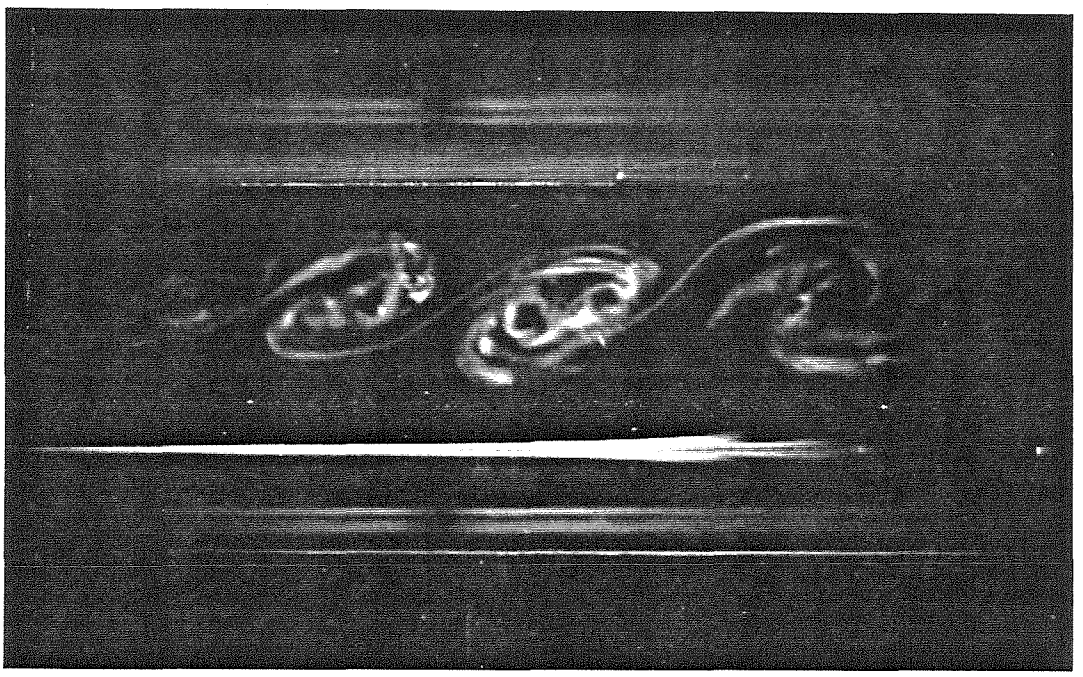

a) ϕ = 1/1.8 Acid/Dye on High Speed and Base on Low Speed

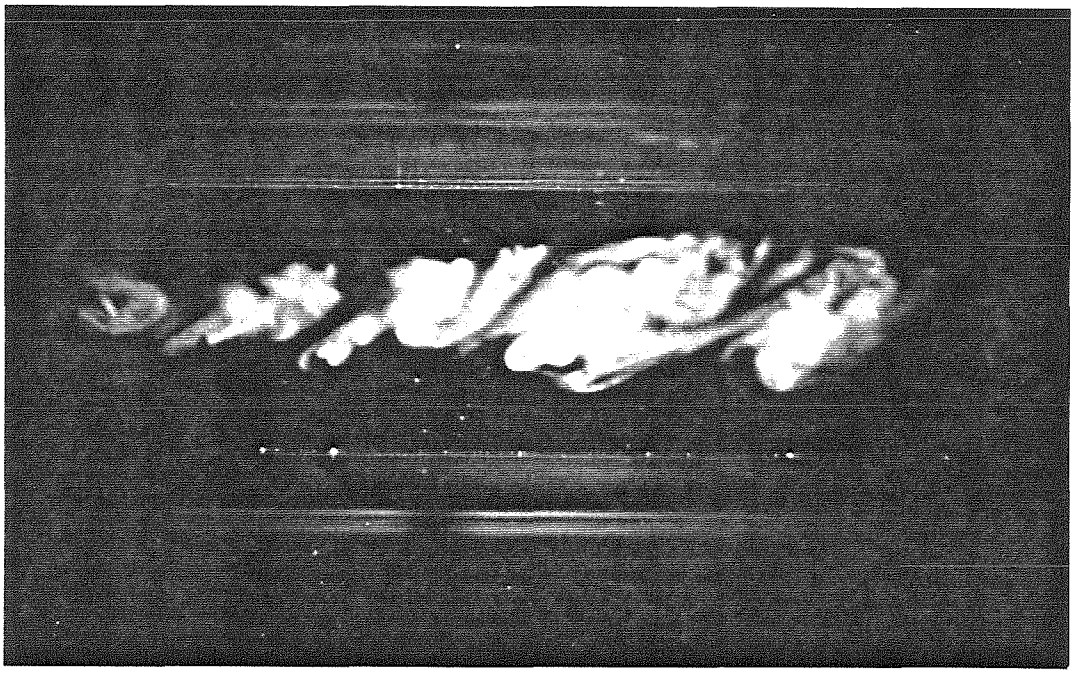

b) ϕ = 1.8 Acid/Dye on Low Speed and Base on High Speed

Figure 8 Photograph of Chemical Reaction in a Shear Layer (f/1.8, 2 msec Exposure), High Speed on Top, U_1 = 42 cm/sec, r = 0.45, Flow from Left to Right

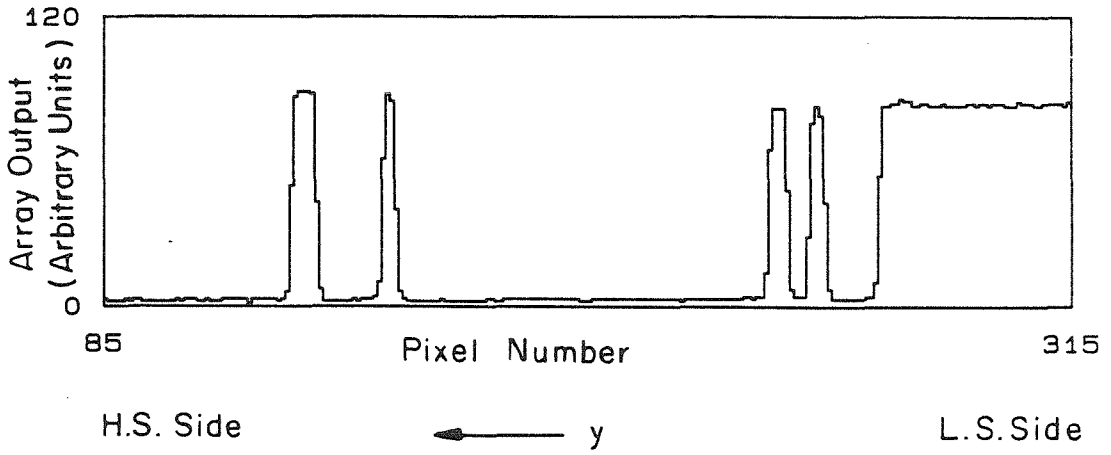

Figure 9 Single Scan Raw Output of Reticon Array

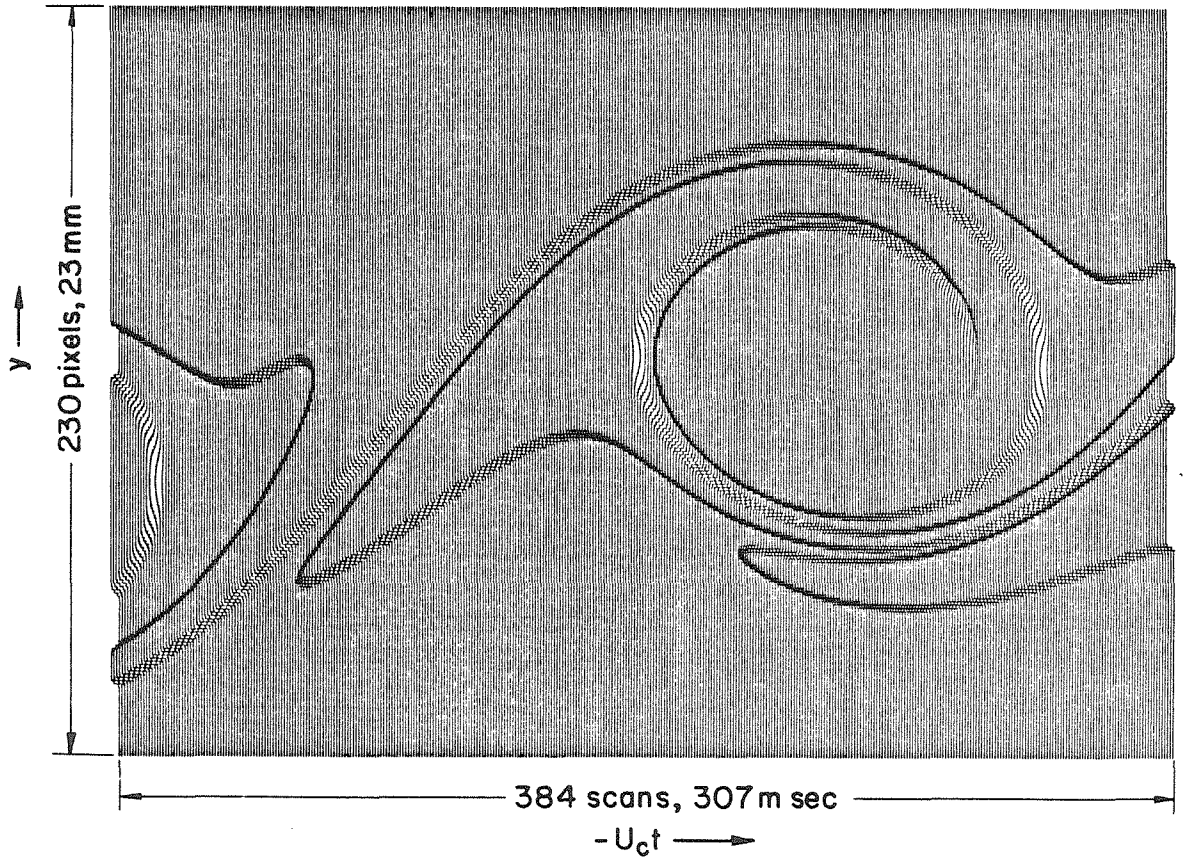

Figure 10 Multiple Scan Raw Output of Reticon Array

a) Single Vortex

b) Pairing Vortices

Figure 11 Flow Images below the Mixing Transition

$r = 0.46$, $Re_{\delta_{vis}} \simeq 1{,}750$

Blue = Pure High Speed Fluid, Red = Pure Low Speed Fluid

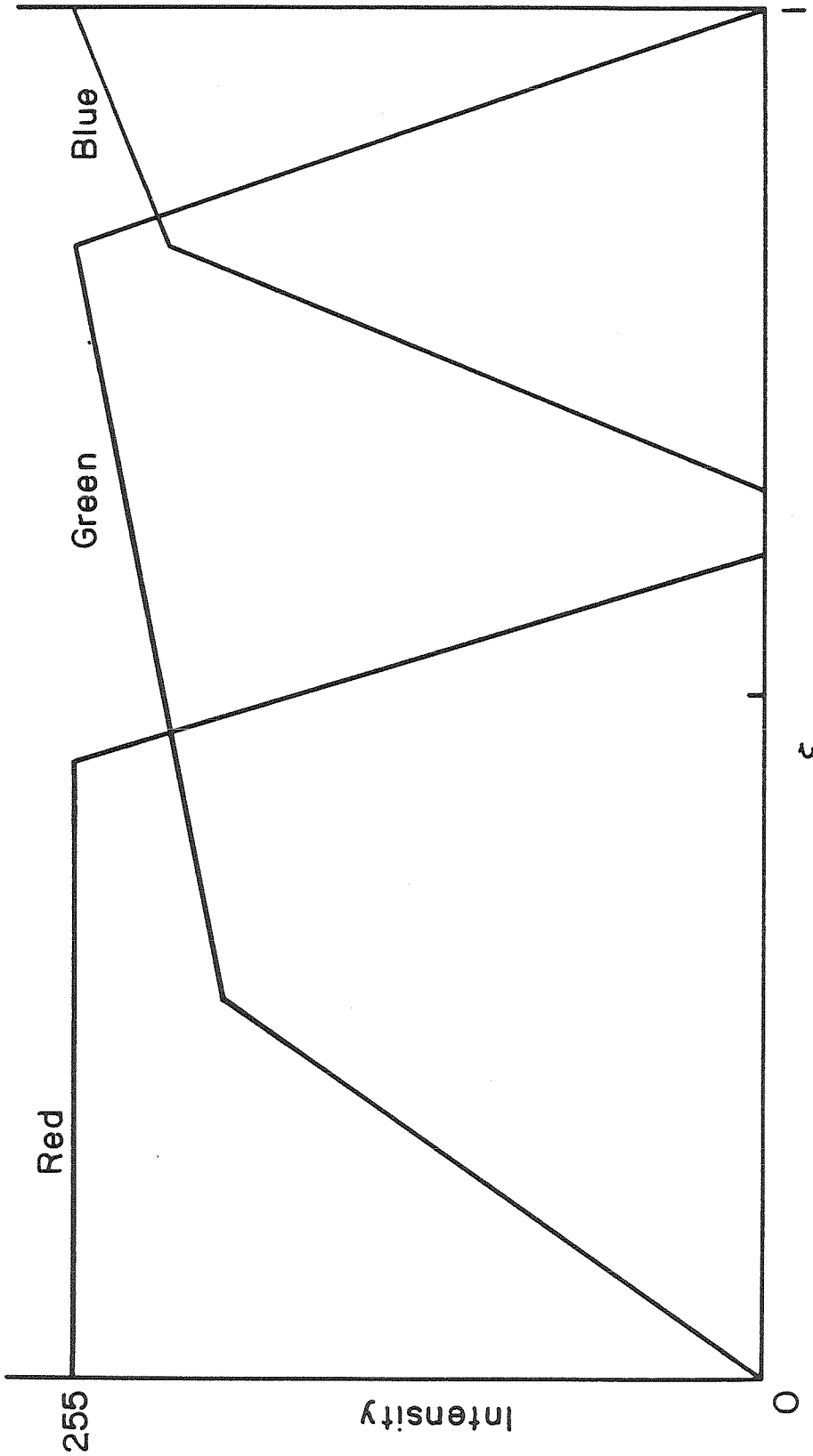

Figure 12 Pseudo-Color Assignment Diagram

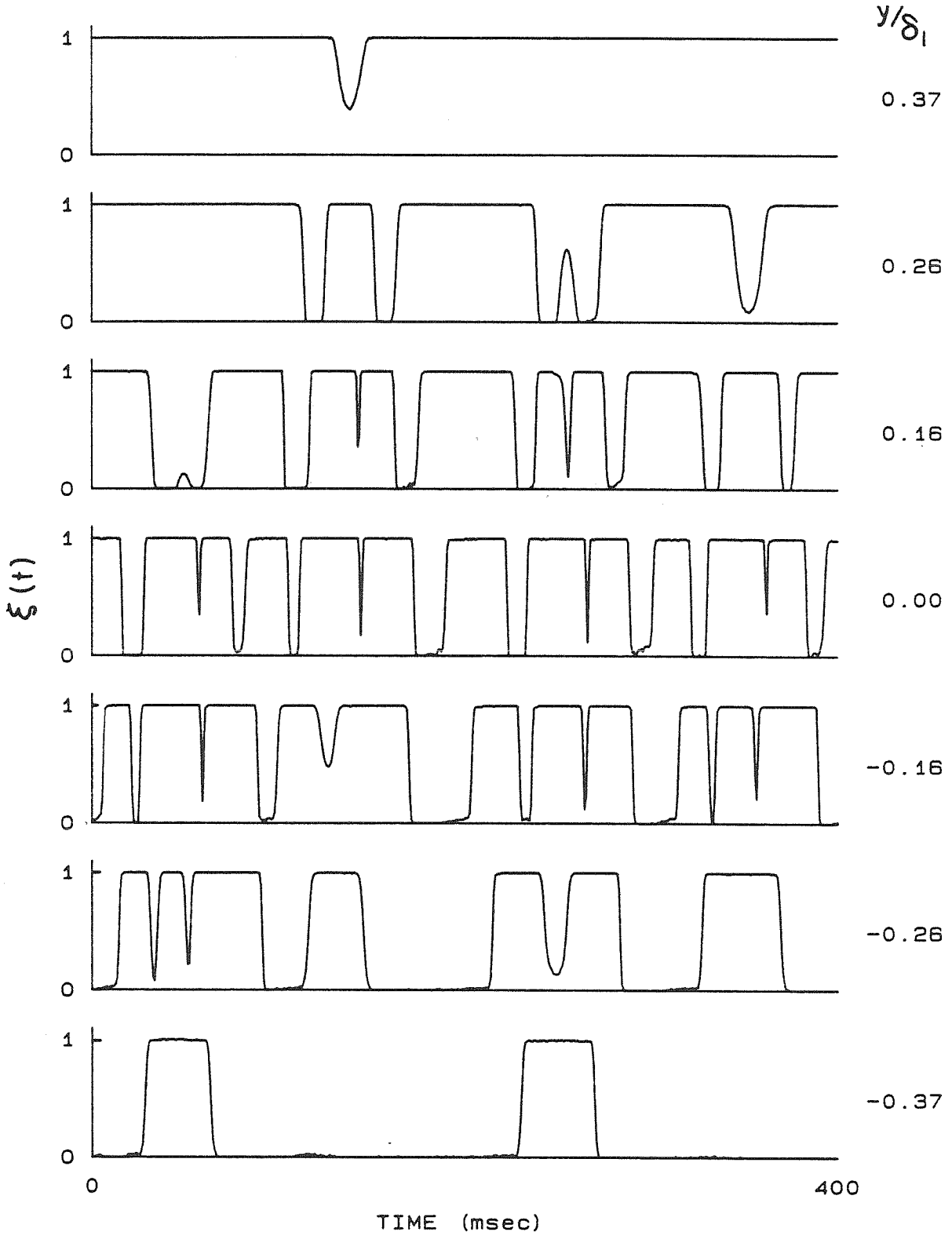

Figure 13 High Speed Fluid Concentration vs Time below the Mixing Transition, r = 0.38, $Re_{\delta_1} \simeq 2,800$

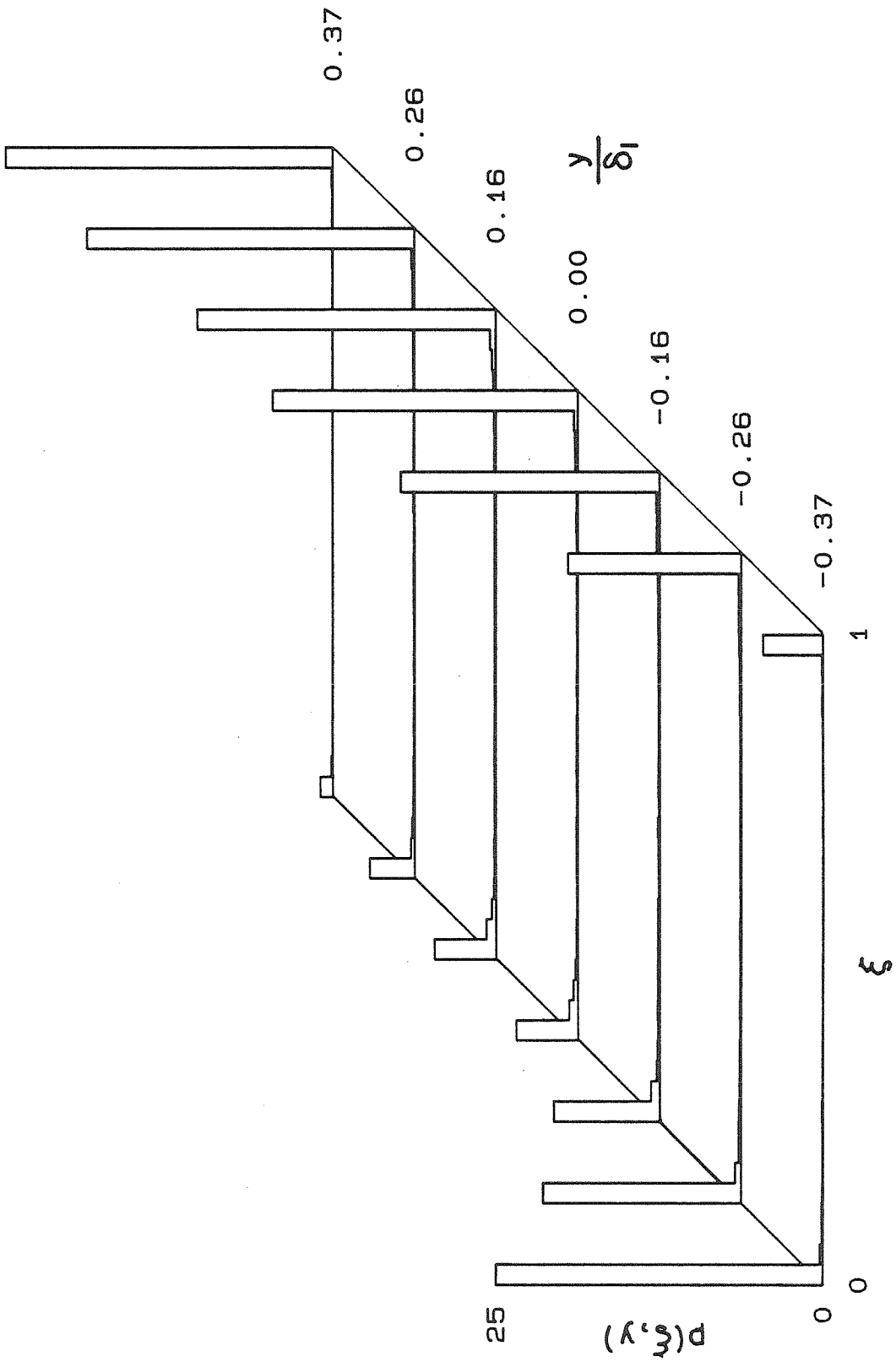

Figure 14 PDF below the Mixing Transition, r = 0.38, $Re_{\delta_1} \simeq 2,800$

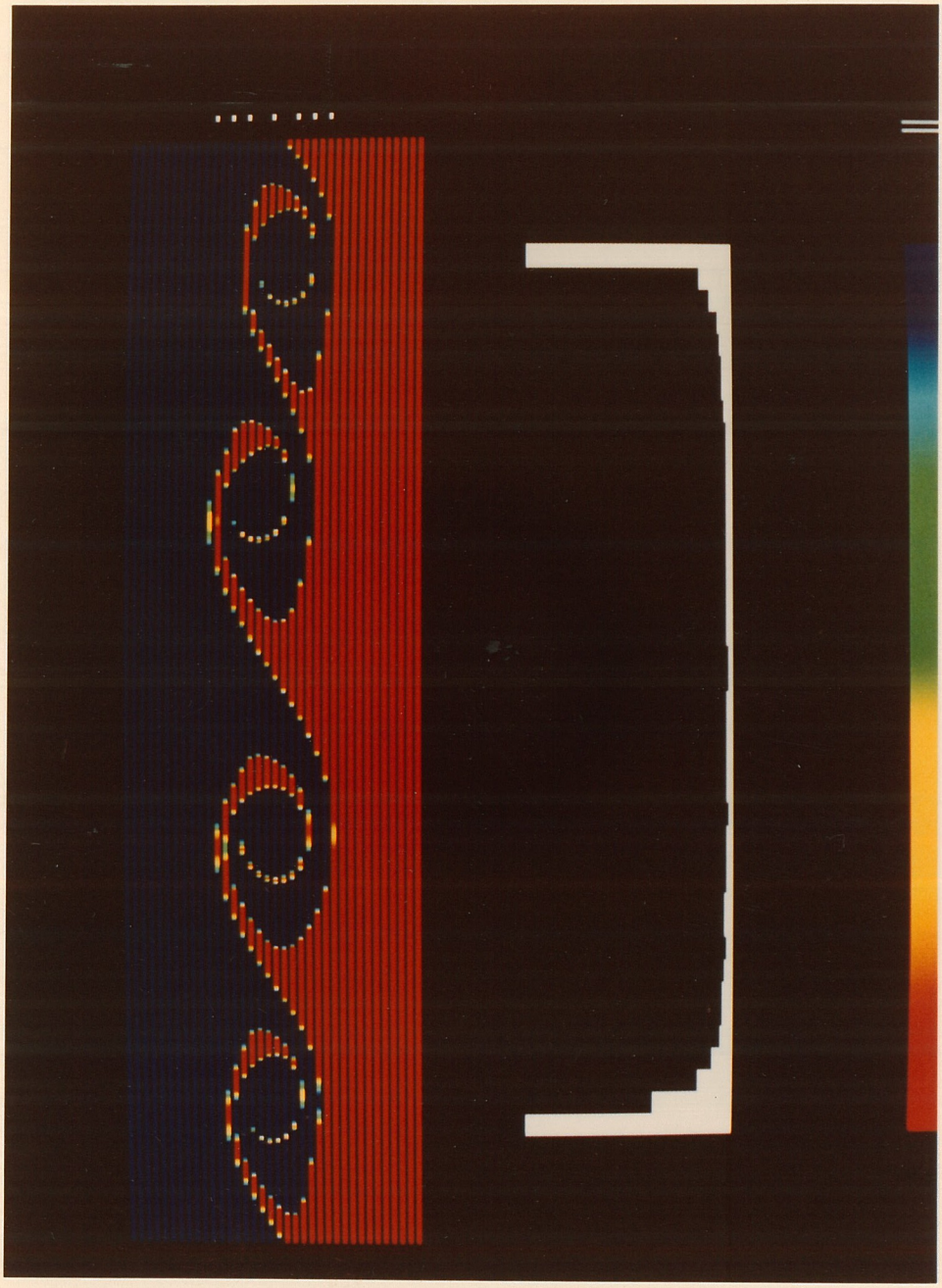

Figure 15 Flow Image of Figure 13

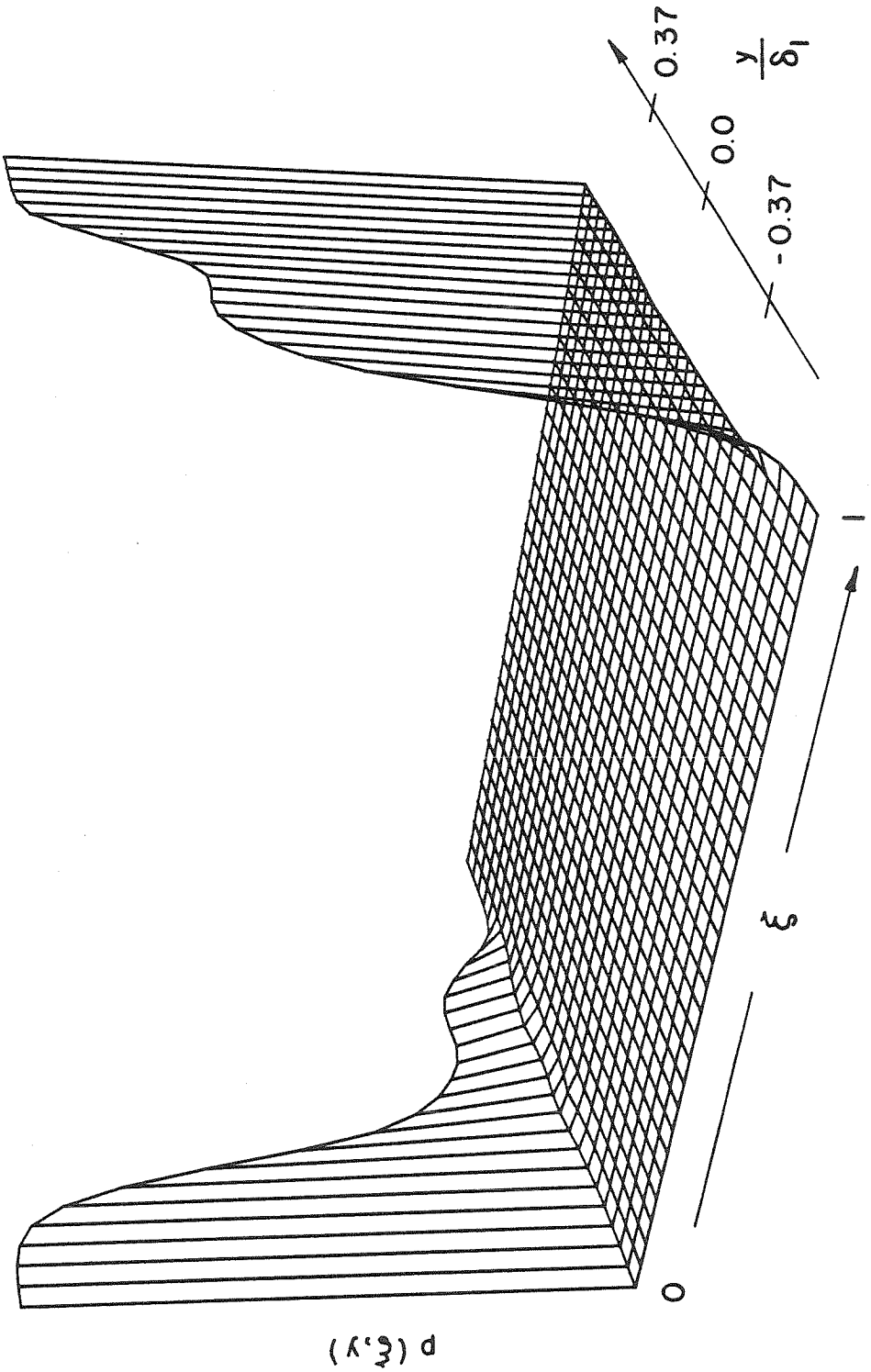

Figure 16 PDF of the Composition Field of the Entire Layer below the Mixing Transition

$r = 0.38$, $Re_{\delta_1} \simeq 2,800$

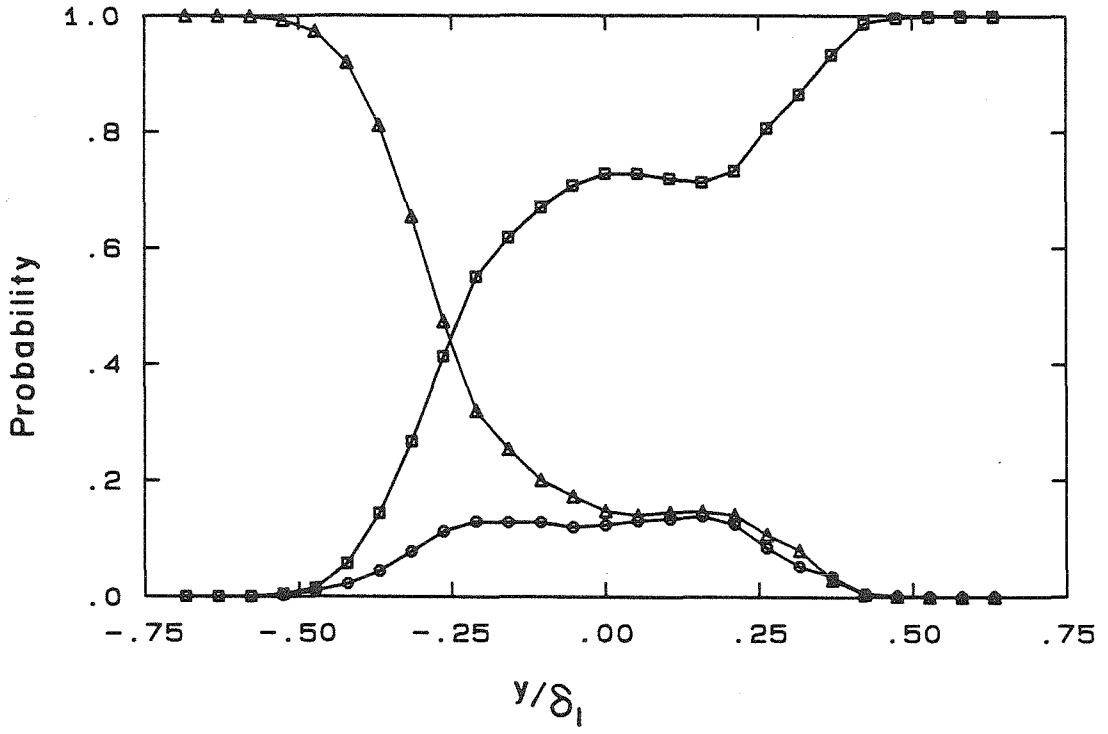

a) Probability of Finding Pure Low Speed Fluid △,
Pure High Speed Fluid □, and Total Mixed Fluid P ○

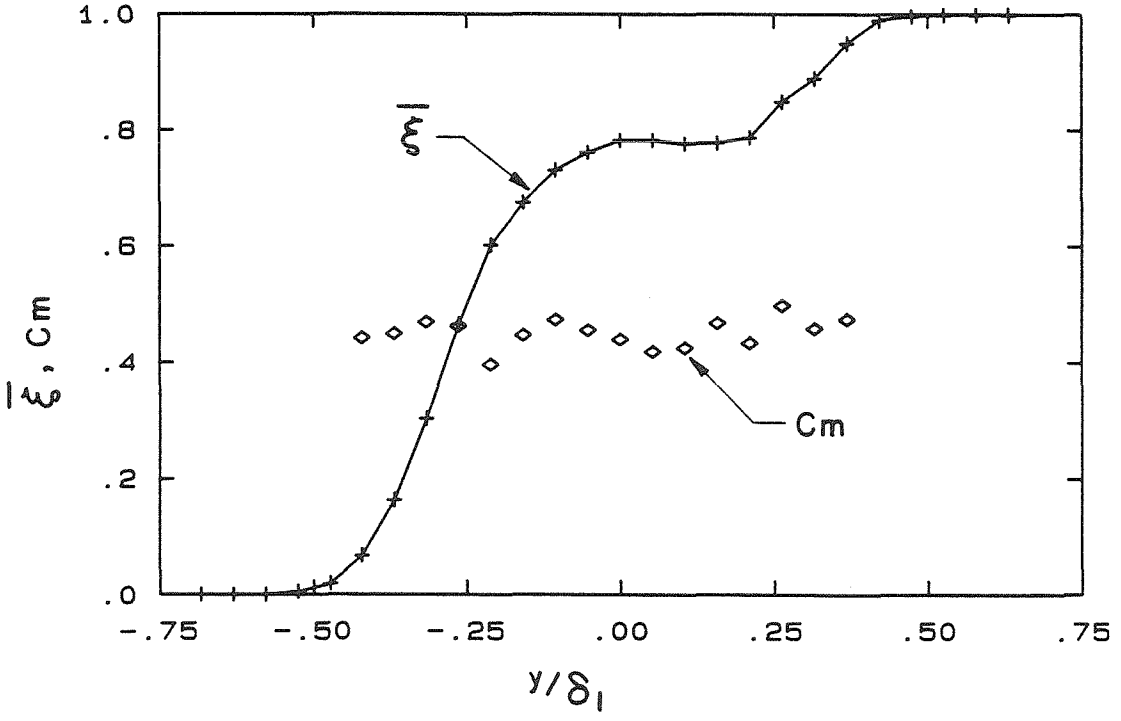

b) Average High Speed Fluid and Mixed Fluid Concentrations

Figure 17 Transverse Profiles below the Mixing Transition

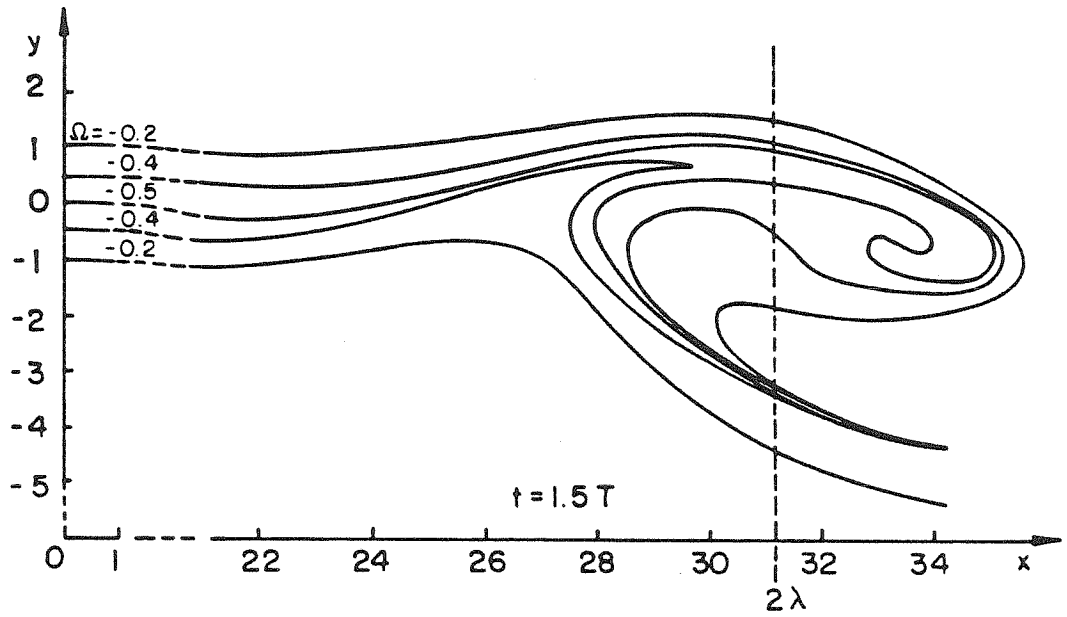

a) Streakline Pattern During Roll-Up

Michalke & Freymuth (1966)

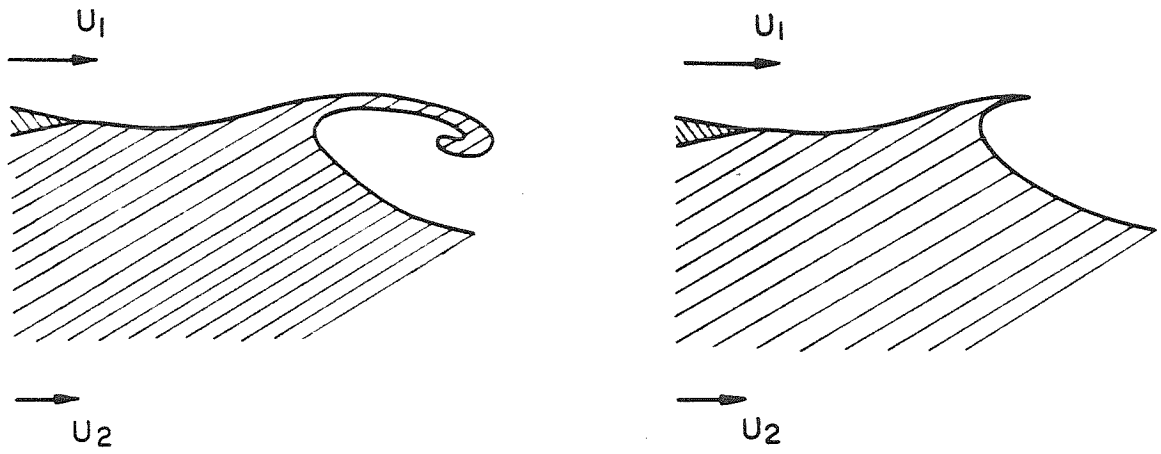

b) Two Possible Dividing Streaklines

Figure 18 Spatial Stability of the Mixing Layer

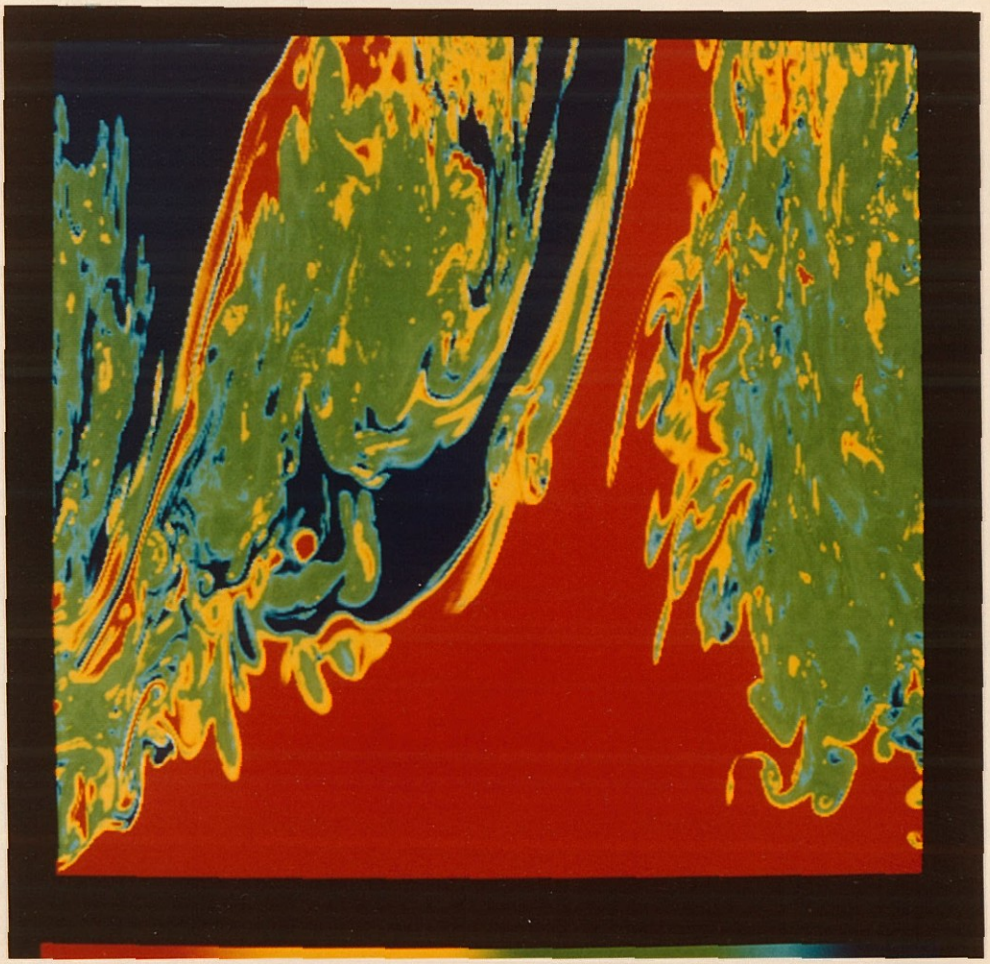

Figure 19 Flow Image above the Mixing Transition

$r = 0.38$, $Re_{\delta_1} \simeq 23{,}000$

Blue = Pure High Speed Fluid

Red = Pure Low Speed Fluid

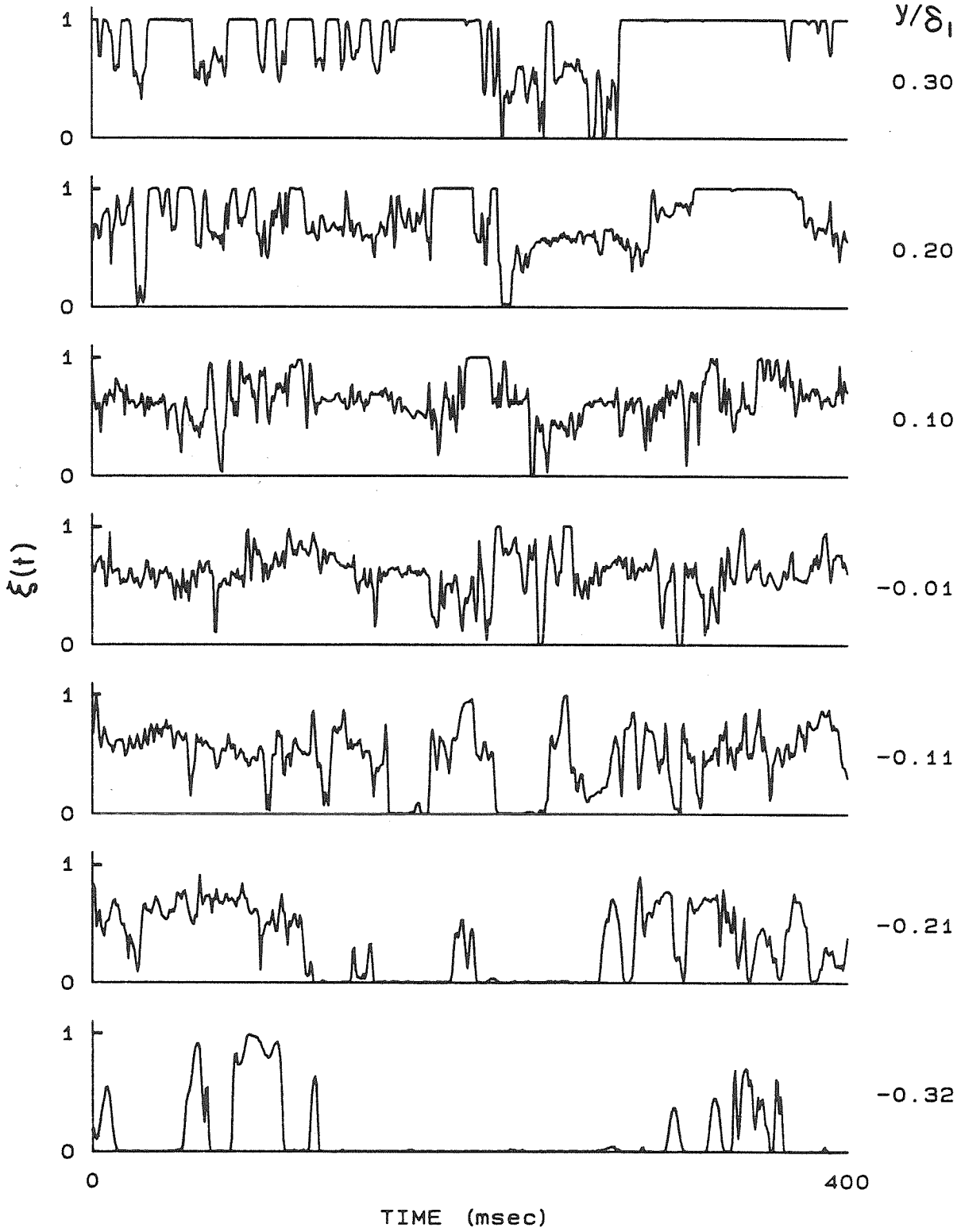

Figure 20 High Speed Fluid Concentration vs Time above the Mixing Transition, r = 0.38, $Re_{\delta_1} \simeq 23{,}000$

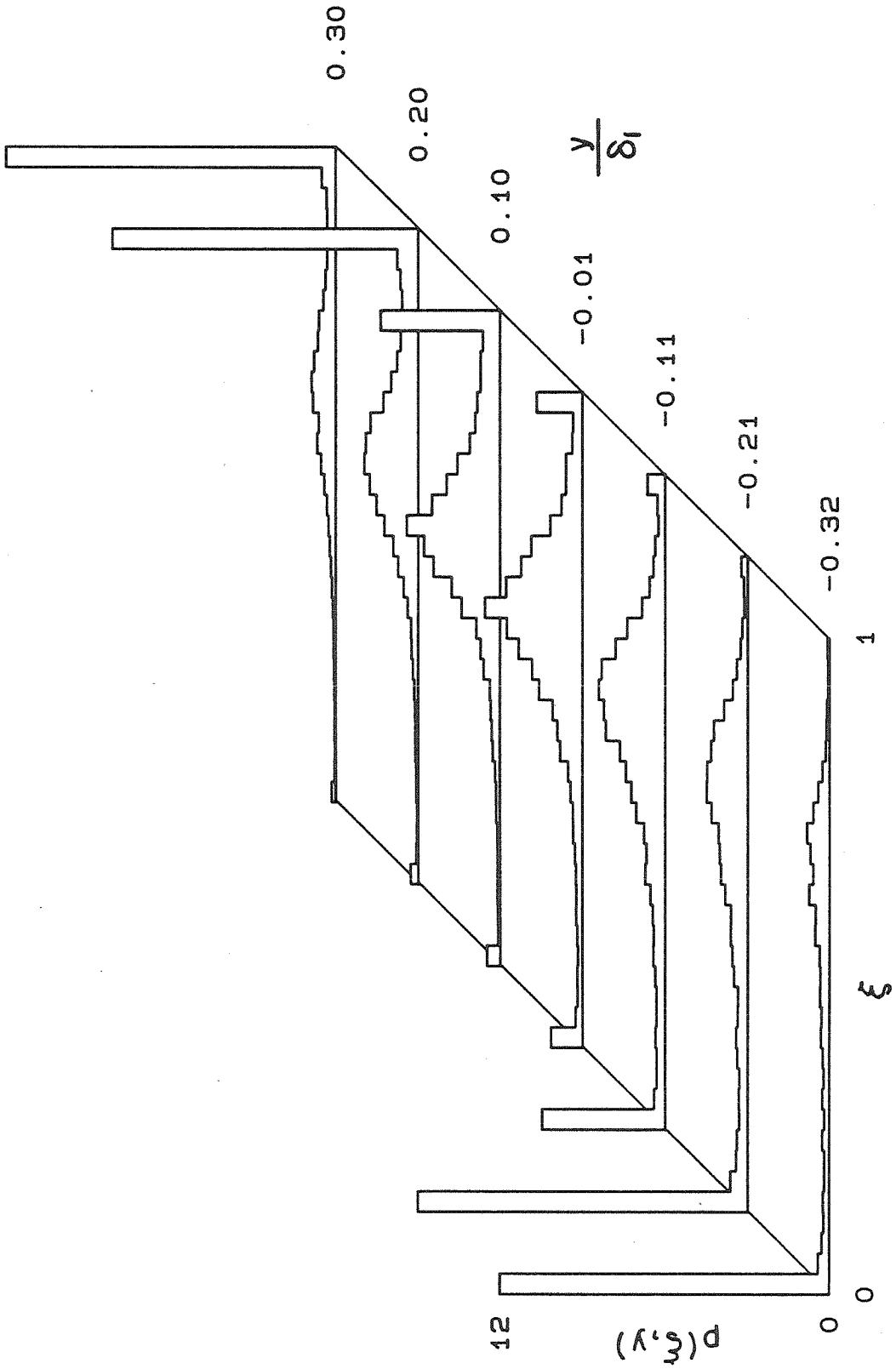

Figure 21 PDF above the Mixing Transition, r = 0.38, $Re_{\delta_1} \simeq 23{,}000$

Figure 22 Flow Image of Figure 20

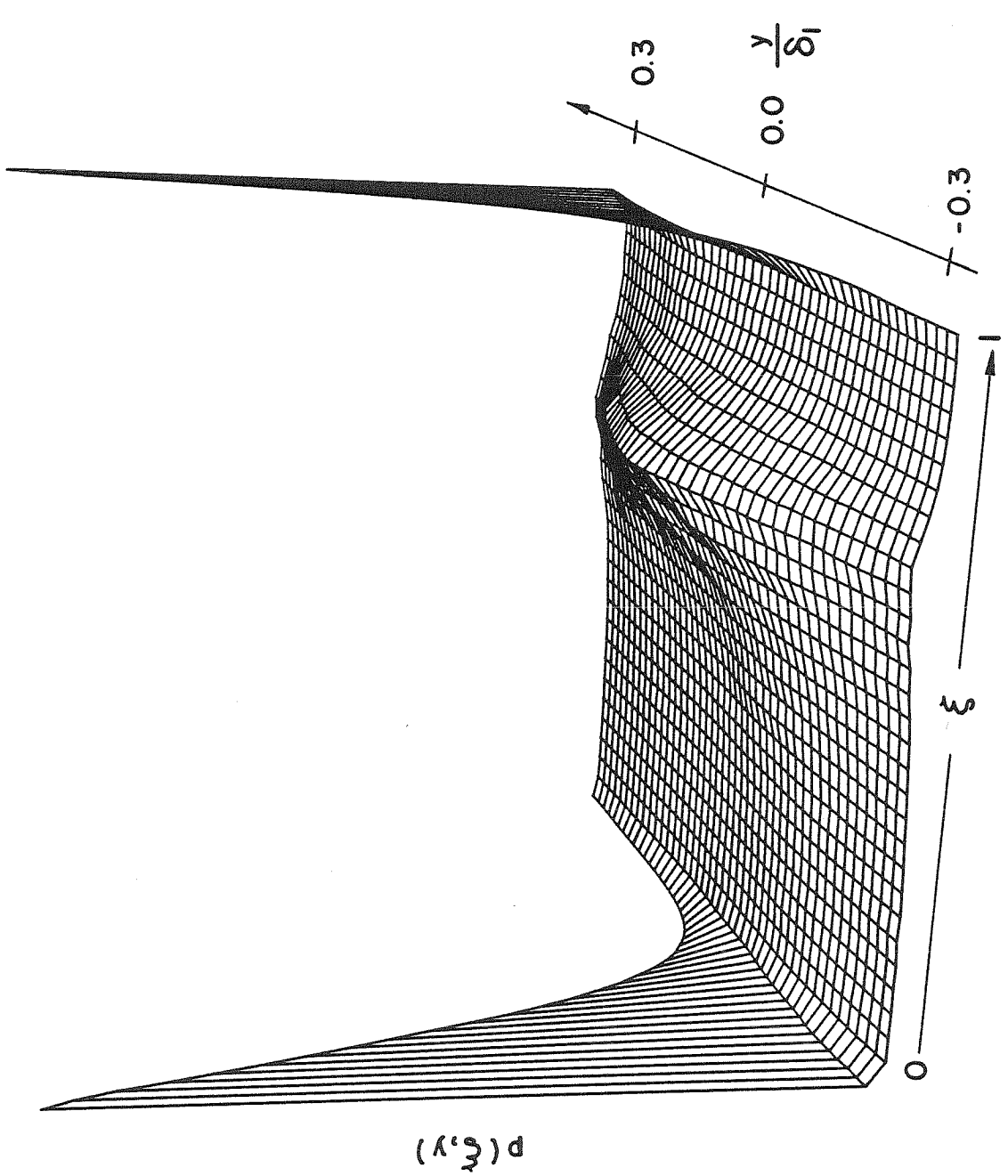

Figure 23 PDF of the Composition Field of the Entire Layer above the Mixing Transition
r = 0.38, $Re_{\delta_1} \simeq 23,000$

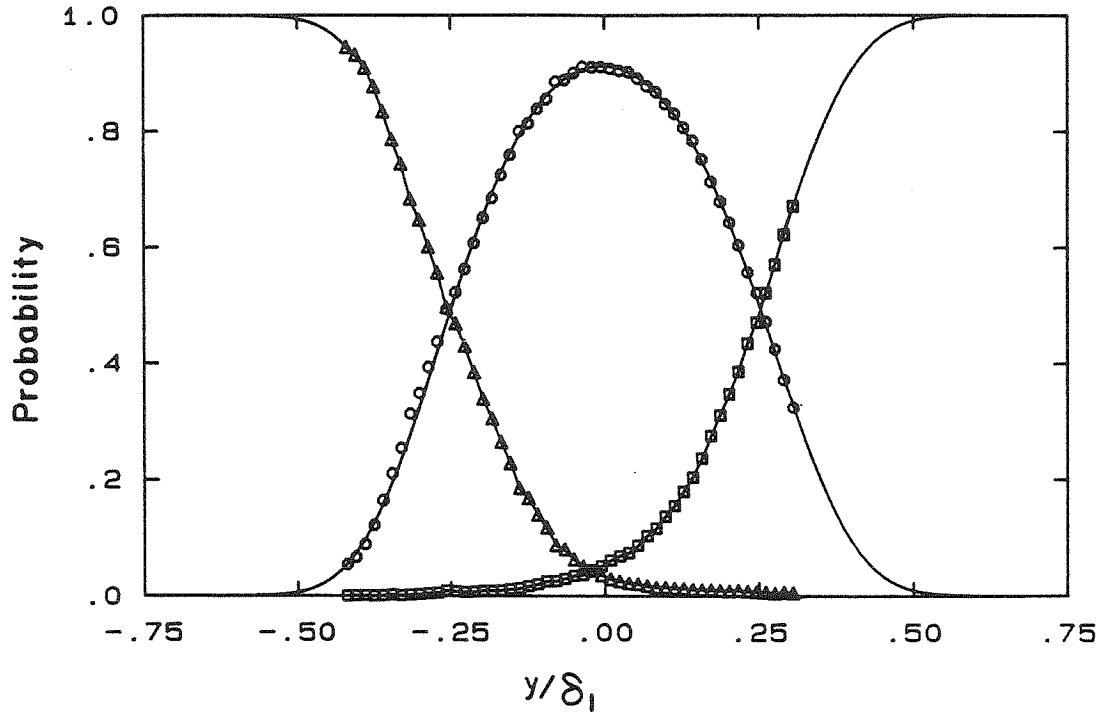

a) Probability of Finding Pure Low Speed Fluid △,
Pure High Speed Fluid □, and Total Mixed Fluid P ○

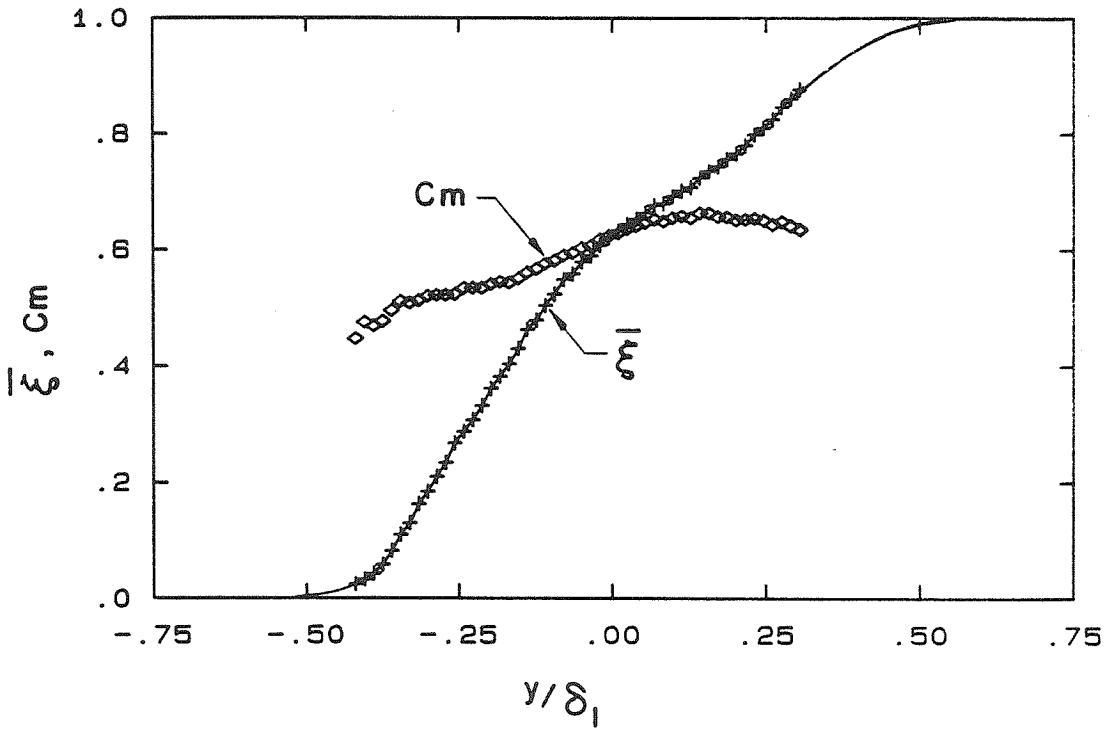

b) Average High Speed Fluid and Mixed Fluid Concentrations

Figure 24 Transverse Profiles above the Mixing Transition

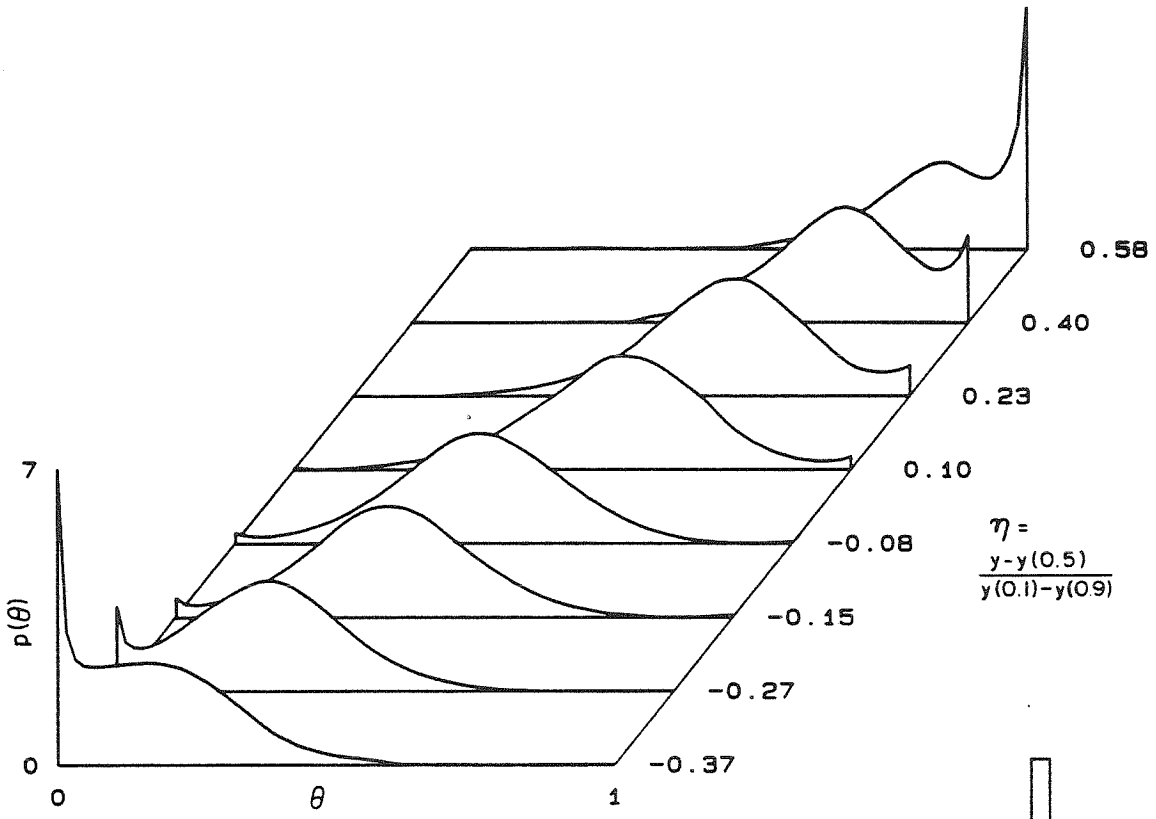

a) PDF from Kollmann (1982)

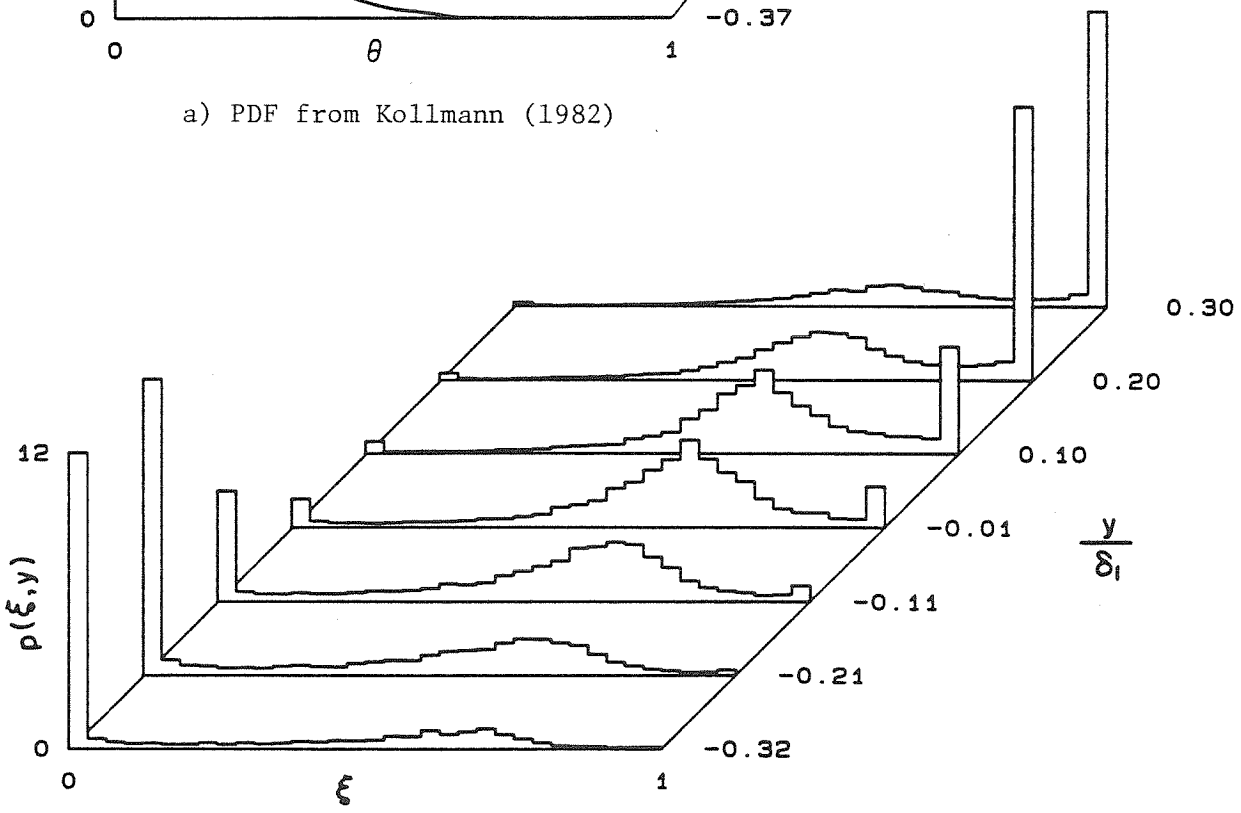

b) PDF, present results

Figure 25 Comparison of PDF with Kollmann

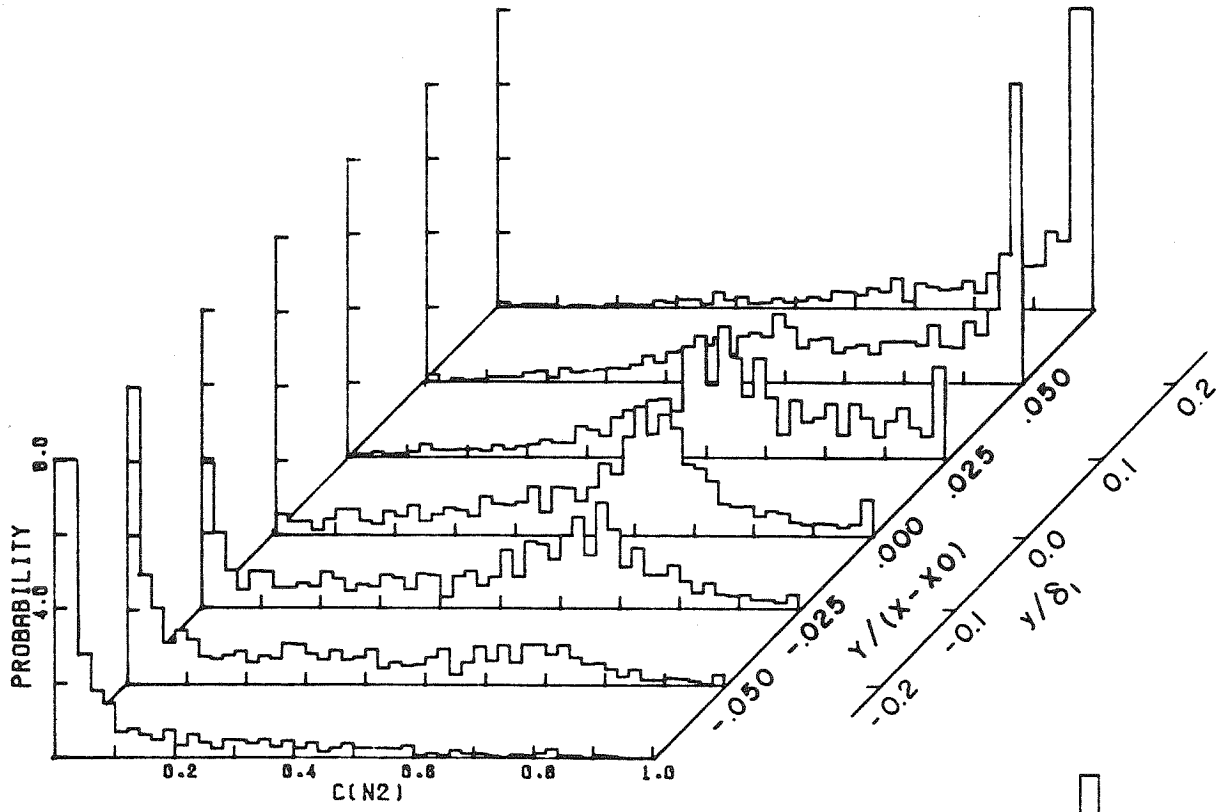

a) PDF from Konrad (1976)

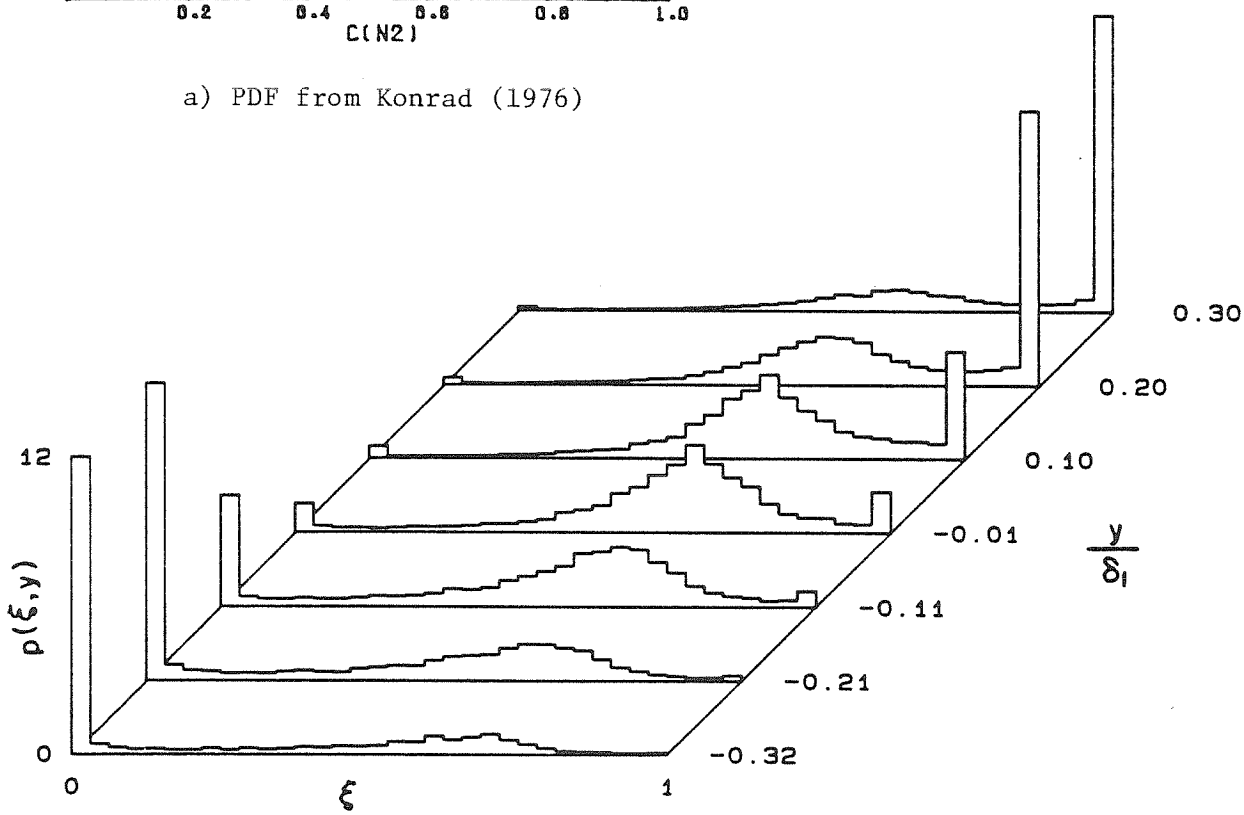

b) PDF, present results

Figure 26 Comparison of PDF with Konrad

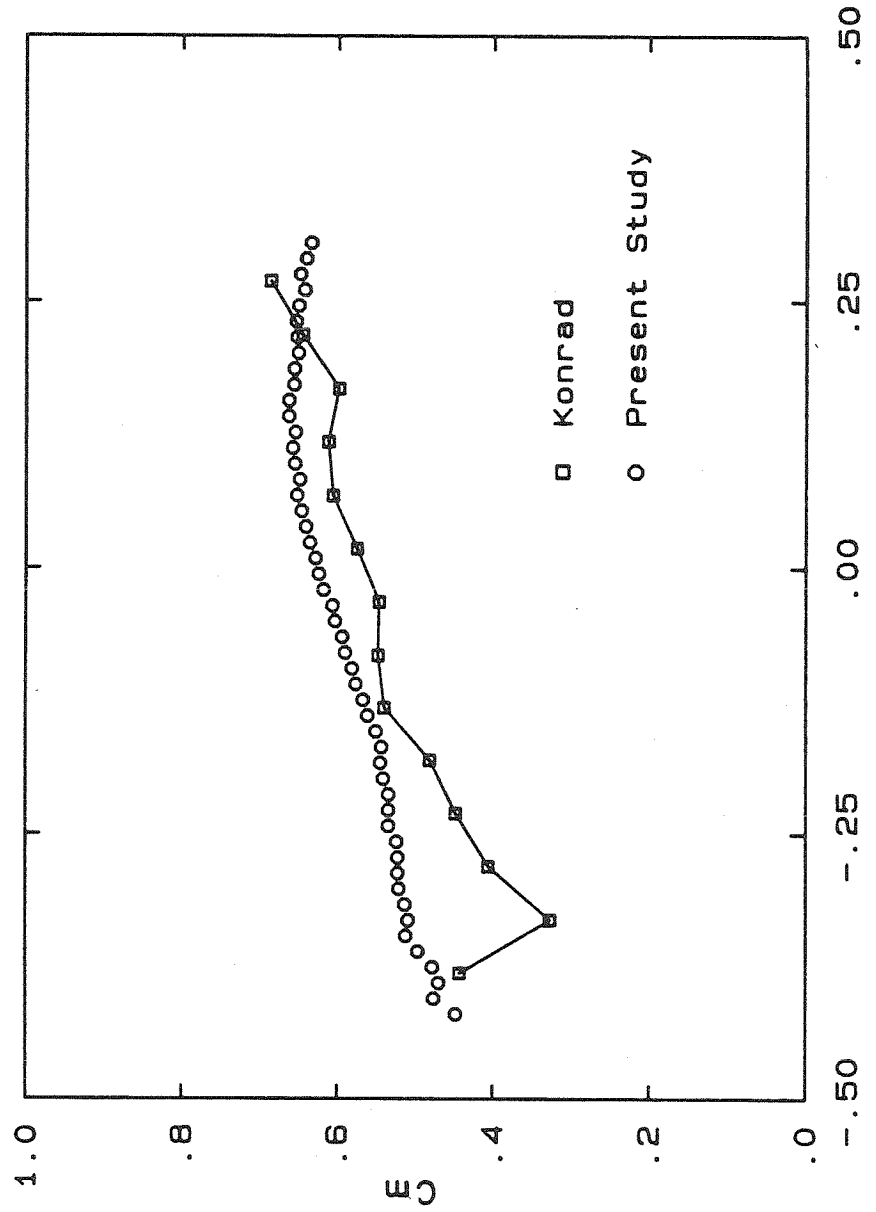

Figure 27 Comparison of Average Mixed Fluid Concentration with Konrad

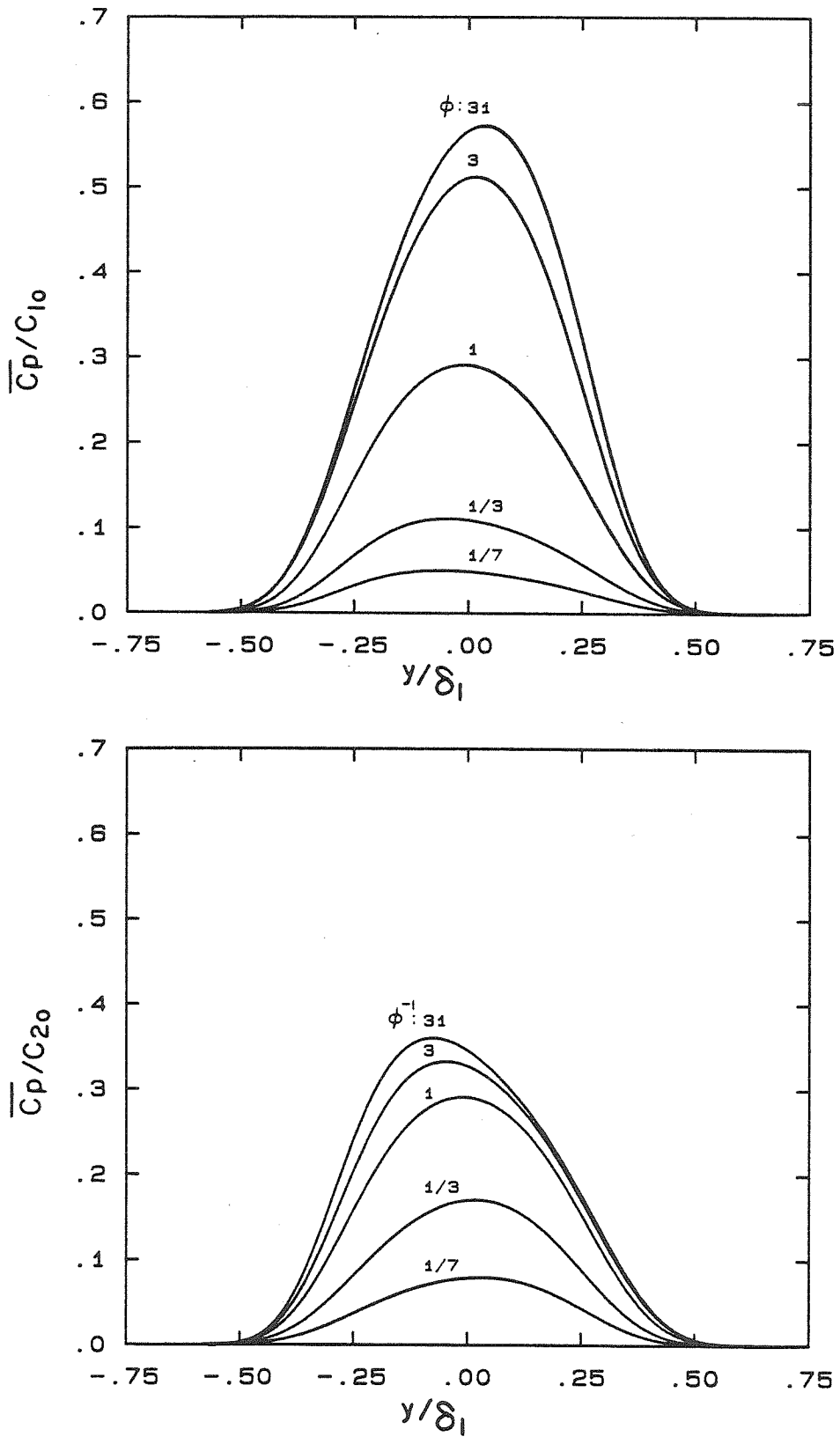

Figure 28 Average Product Concentration Profiles Calculated from Dilution Data

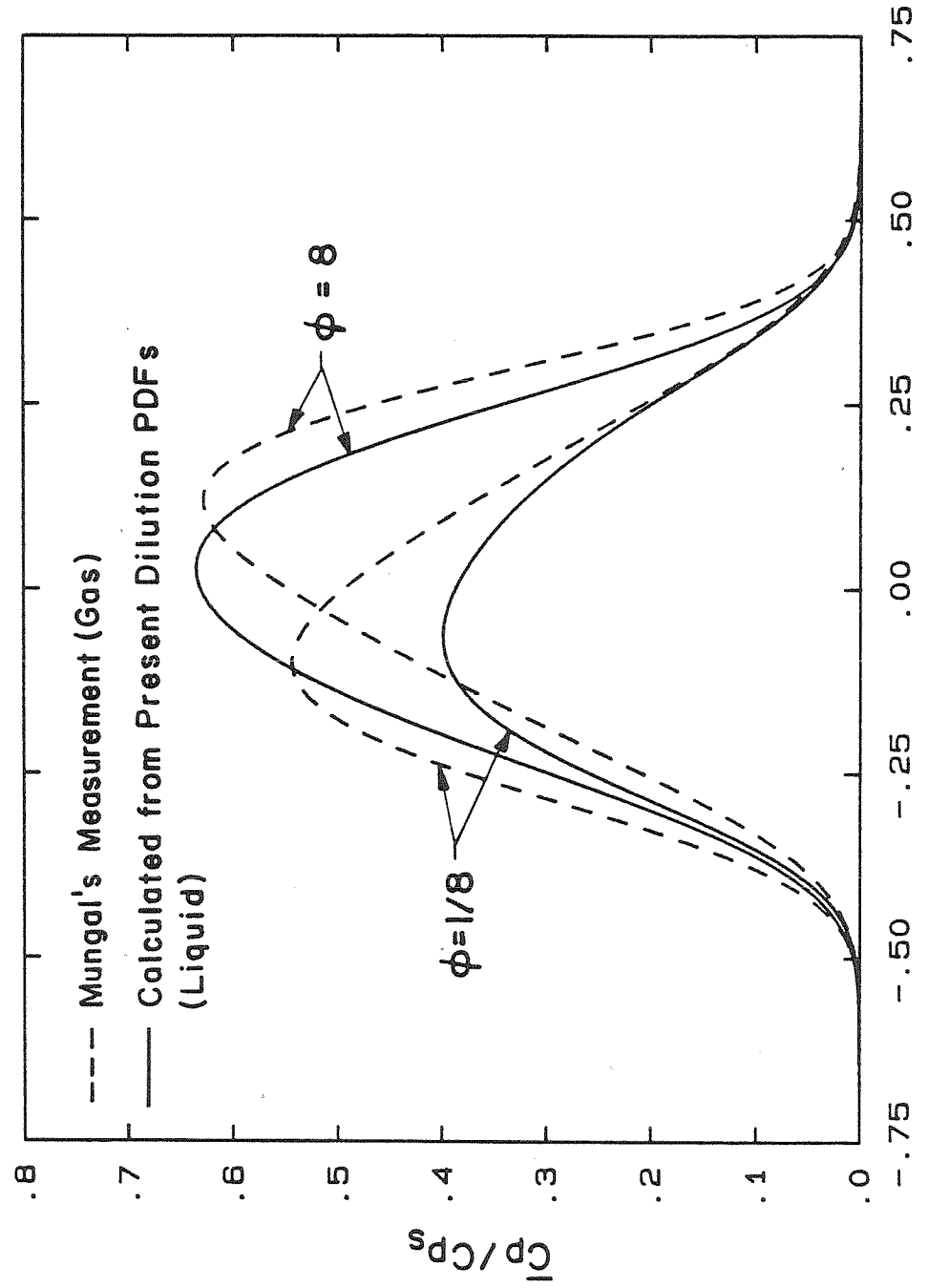

Figure 29 Comparison of Average Product Concentration Profiles of Gas and Liquid

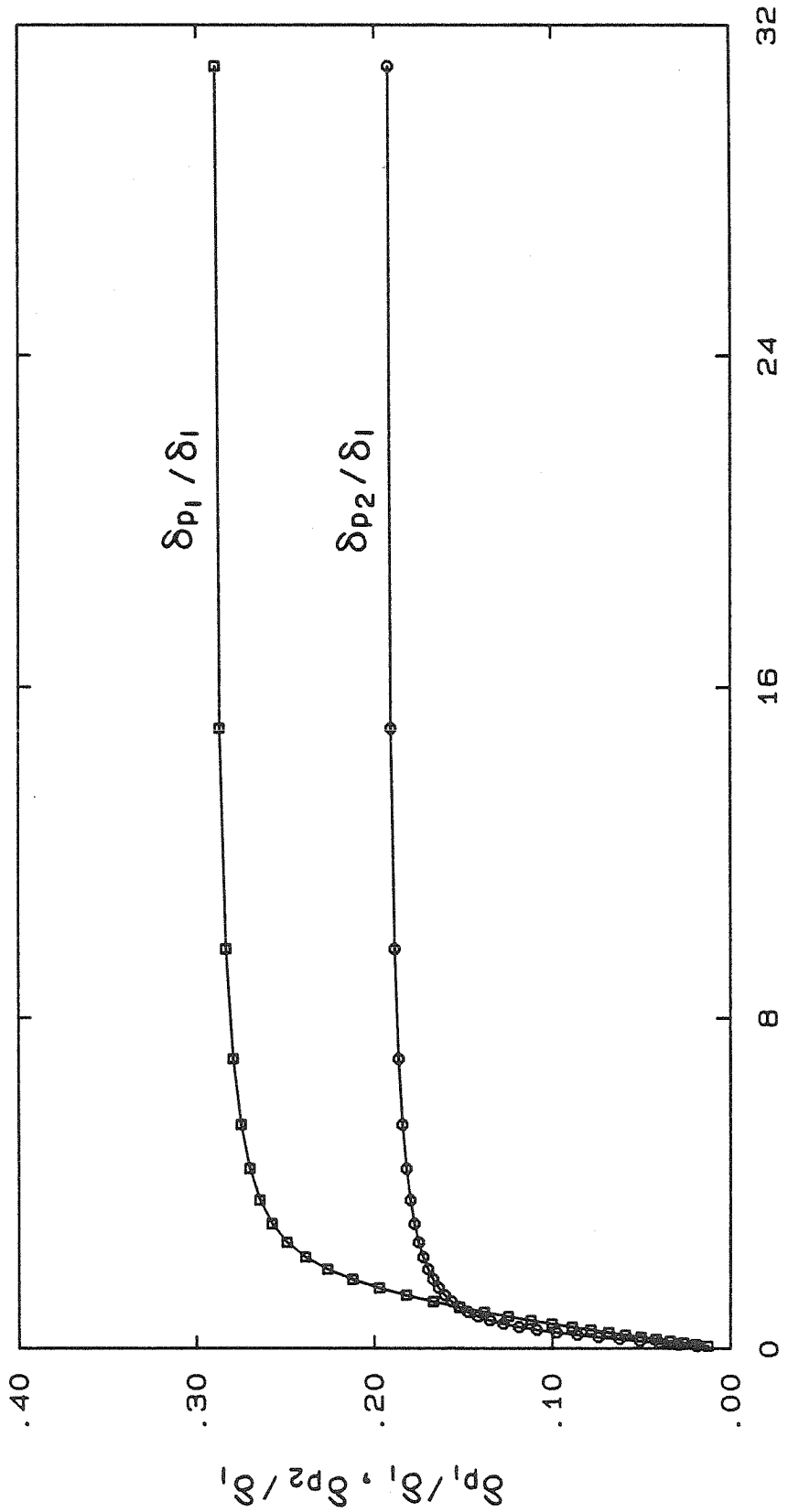

Figure 30 Product Thickness Calculated from Dilution Data

b) $\phi = 4$

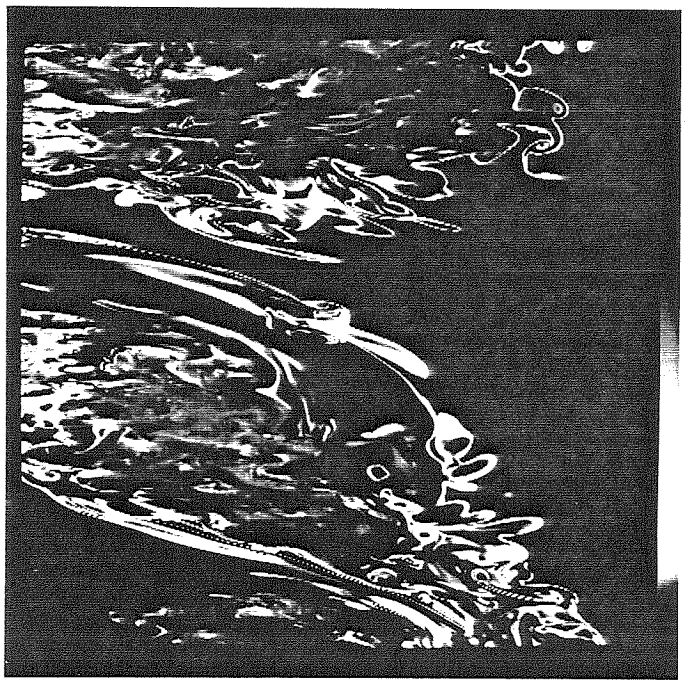

a) $\phi = 1/4$

Figure 31 Flow Images for a Flip Experiment

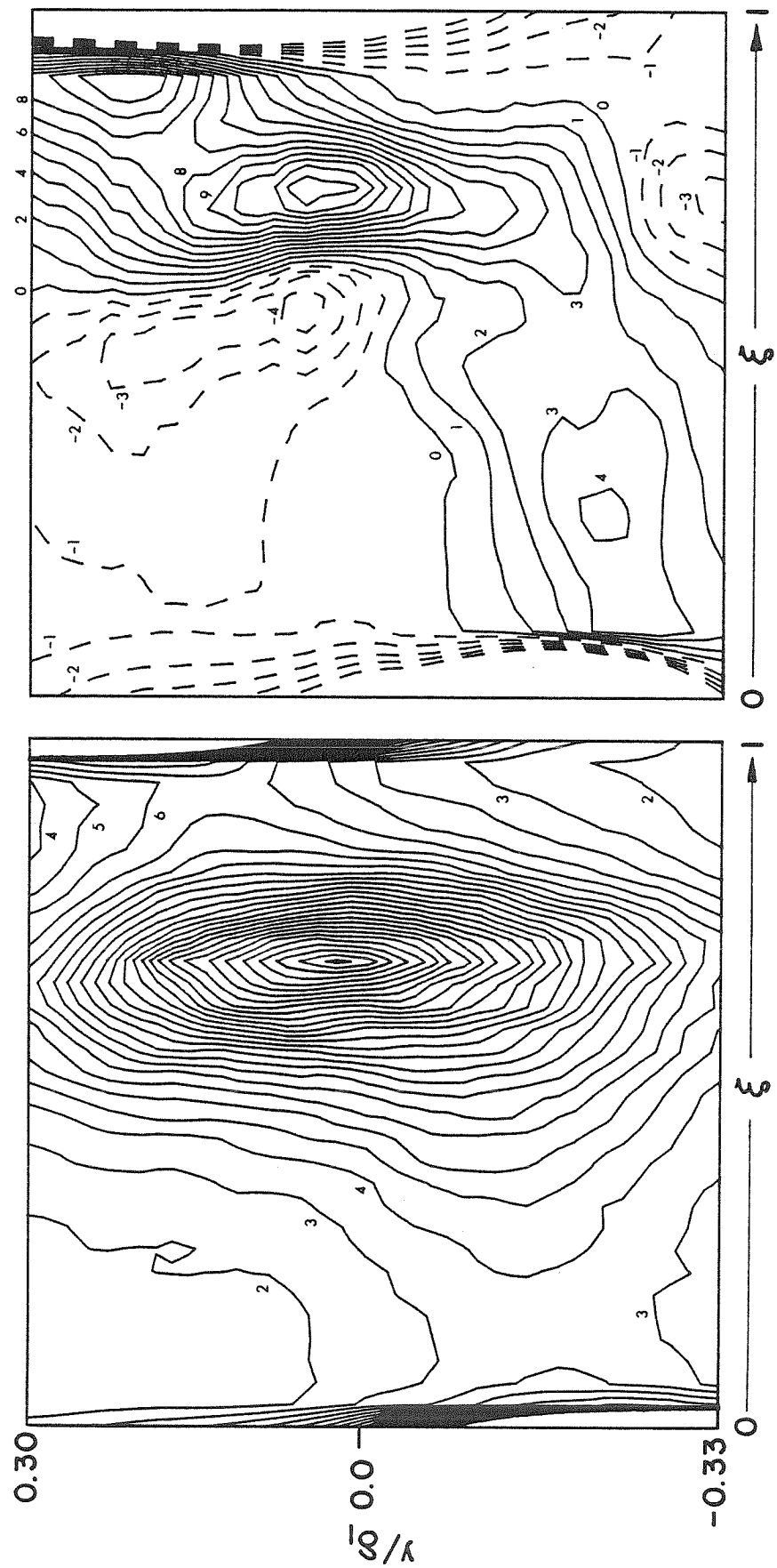

a) Contour Plot of Figure 23, 0.8 msec scan data
Contours are equispaced.
Contour Value = 0.004 x Contour Number

b) Contour Plot of the Difference between the PDFs of 8.0 and 0.8 msec scan data
Contours are equispaced.
Contour Value = 0.002 x Contour Number

Figure 32 Effect of Resolution on the PDF

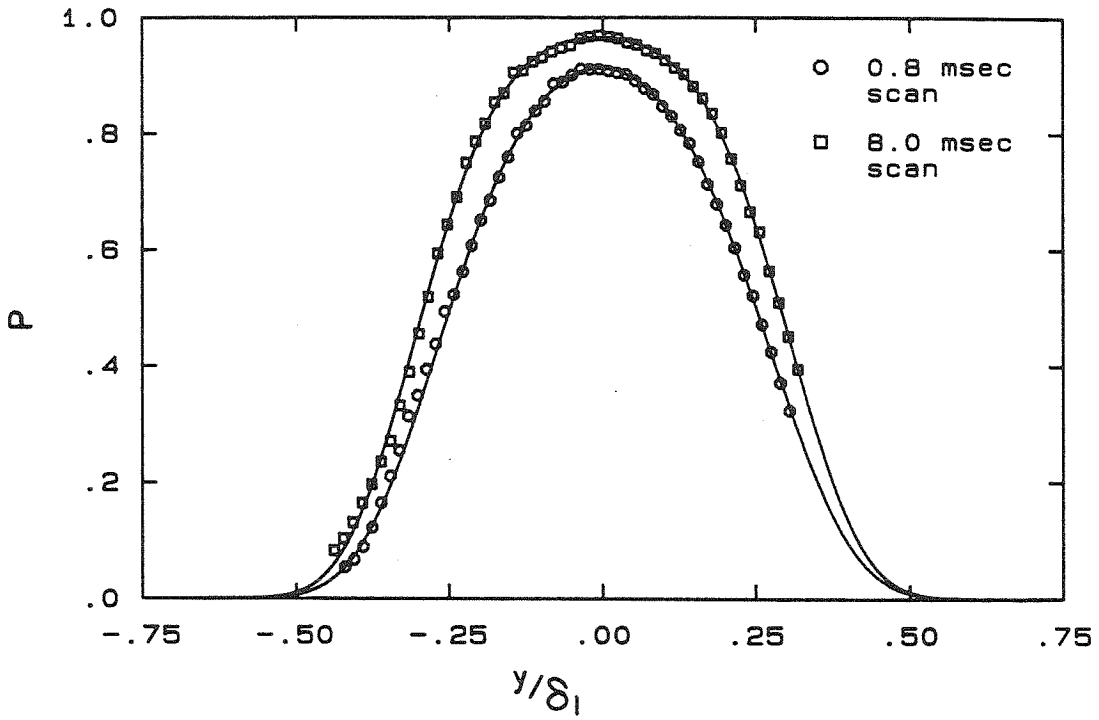

a) Total Mixed Fluid Probability

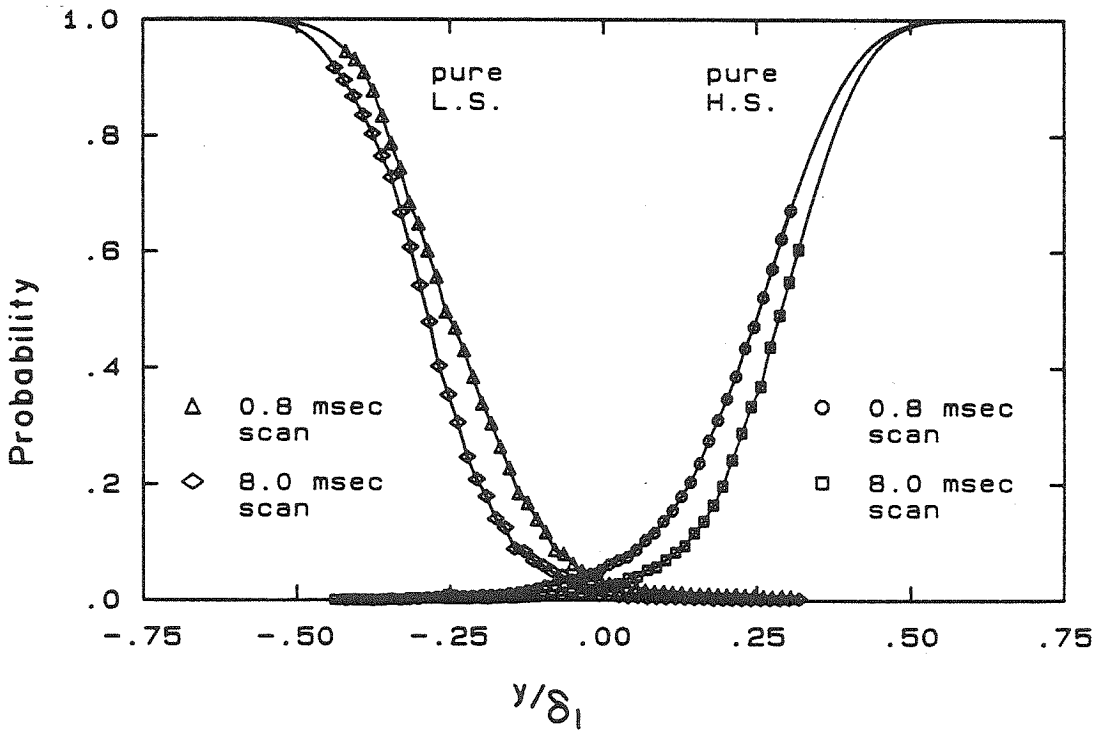

b) Probability of Finding Pure Low Speed and High Speed Fluids

Figure 33 Effect of Resulution on the Transverse Profiles

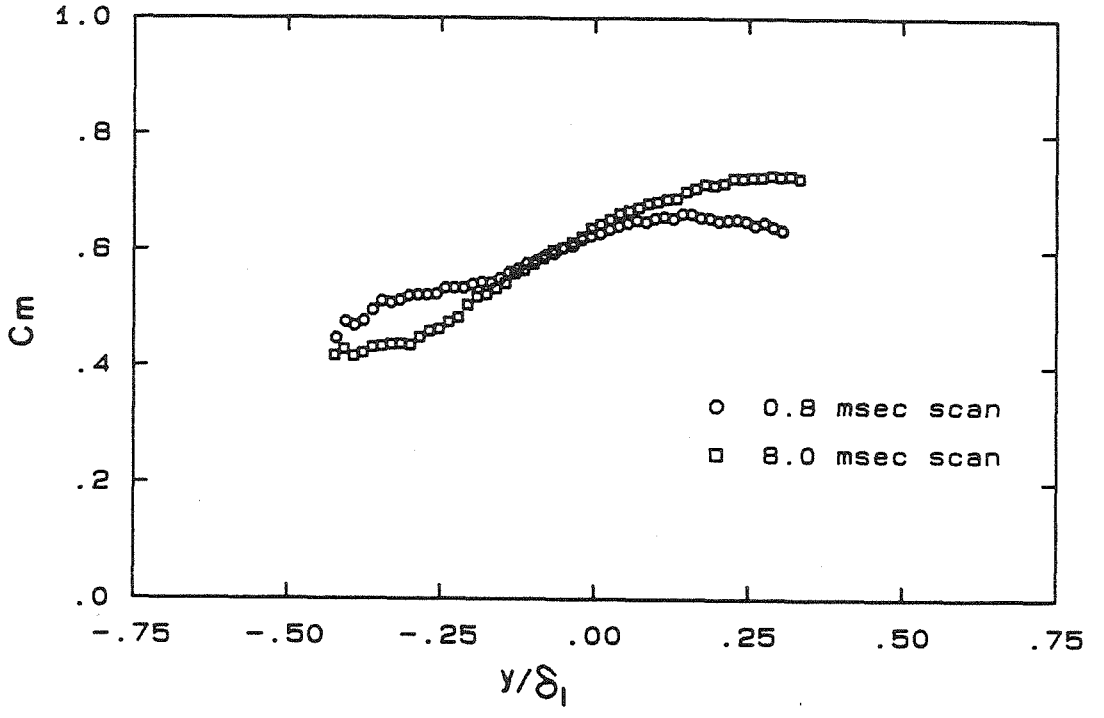

c) Average Mixed Fluid Concentration

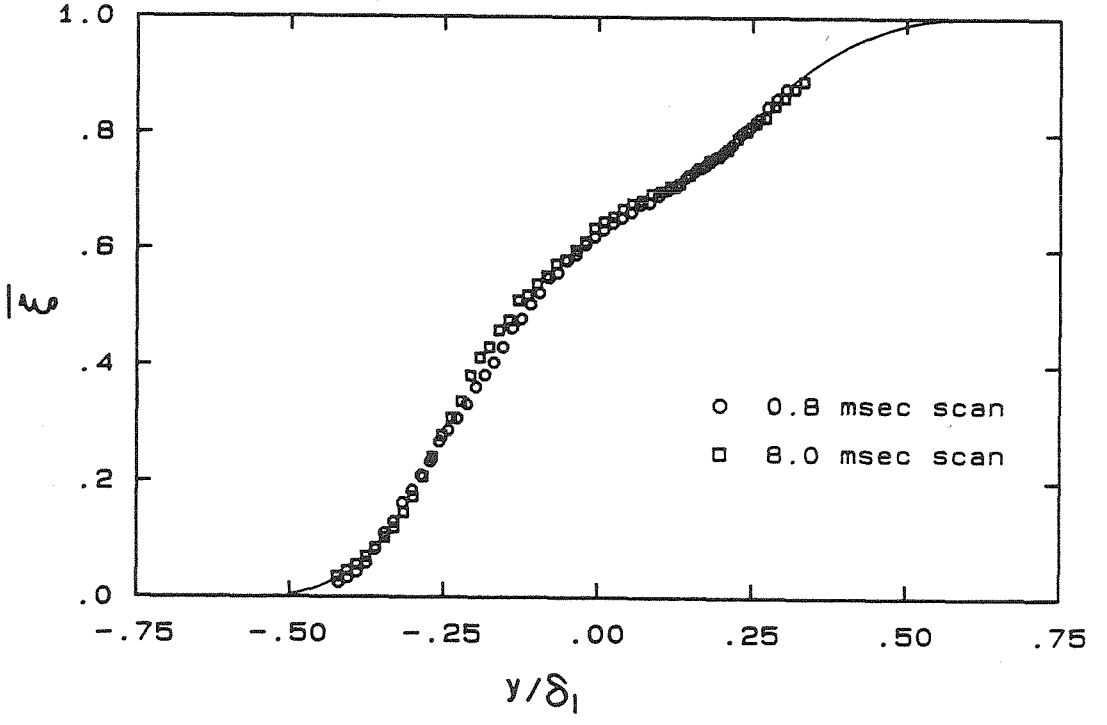

d) Average High Speed Fluid Concentration

Figure 33 Continued

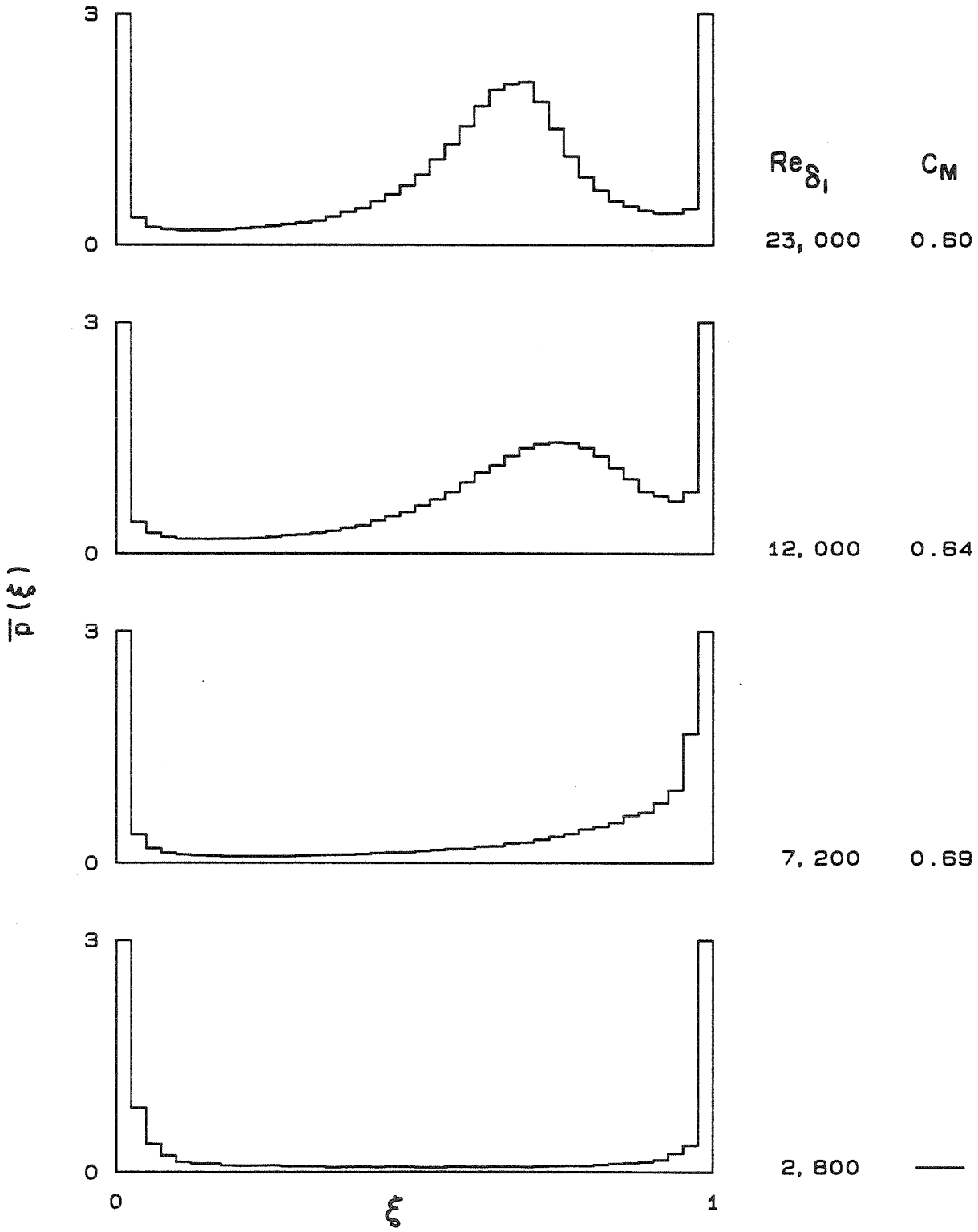

Figure 34 Evolution of the PDF in the Transition Region, r = 0.38

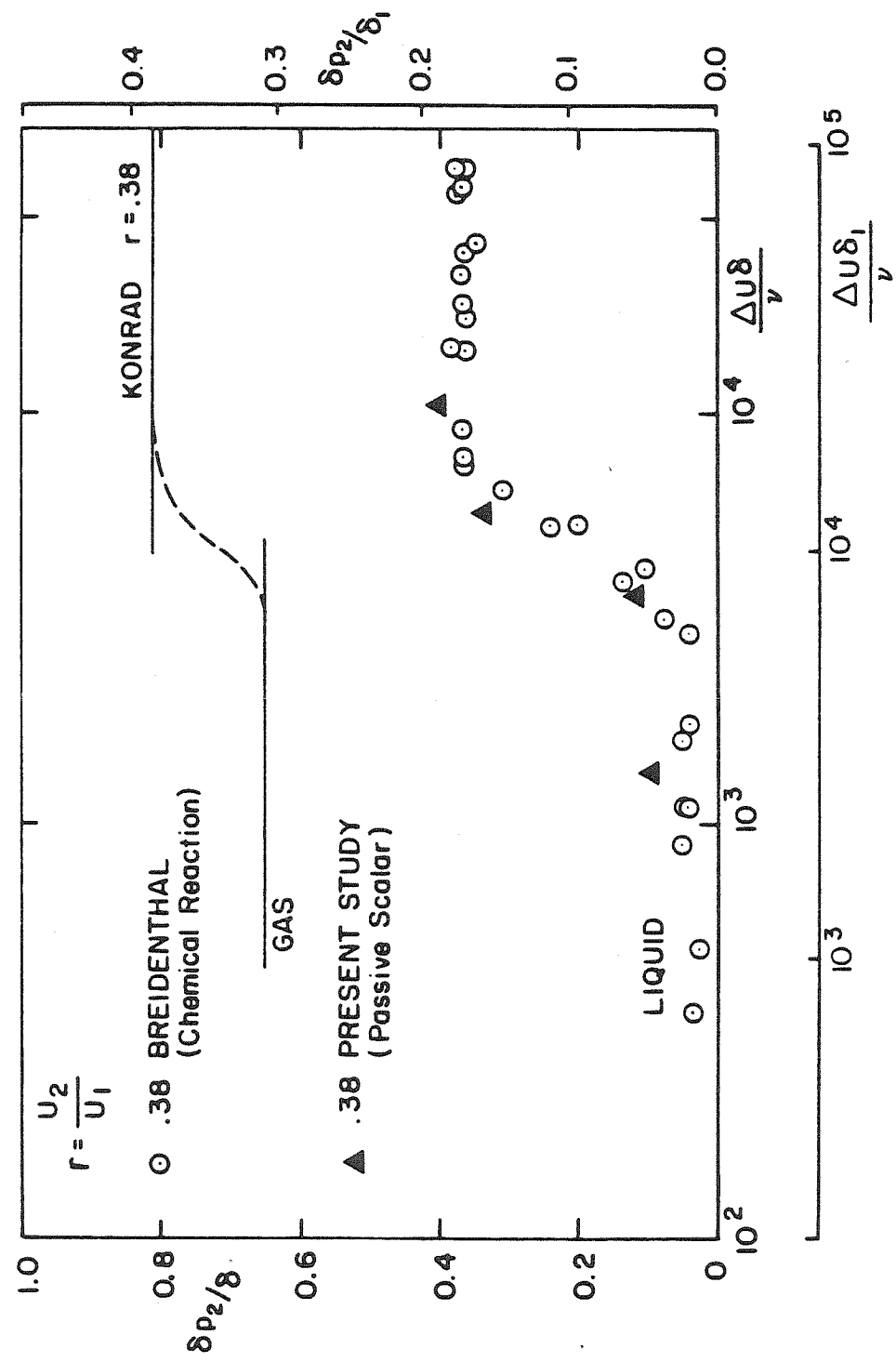

Figure 35 Comparison of Product Thickness with Breidenthal

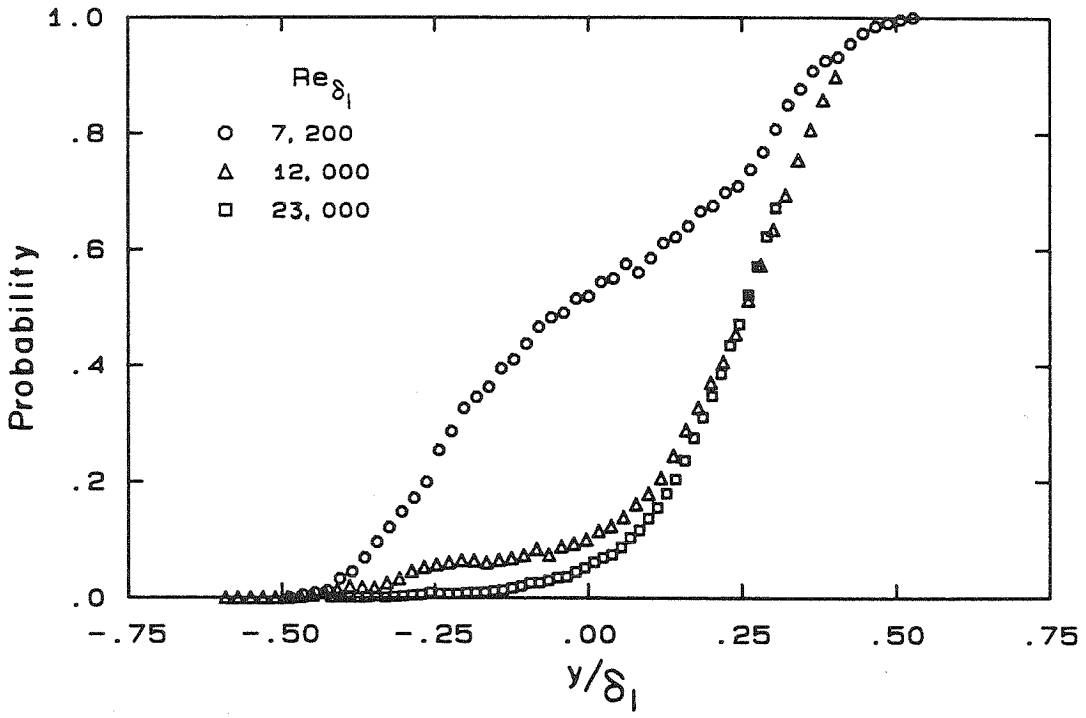

a) Probability of Finding Pure High Speed Fluid

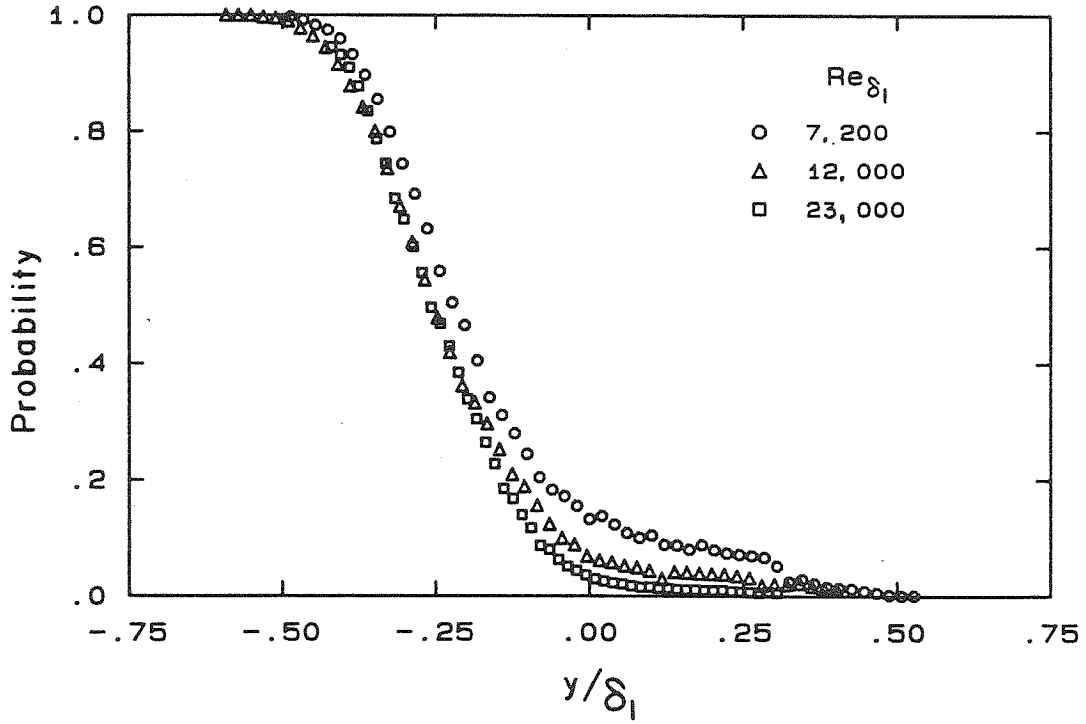

b) Probability of Finding Pure Low Speed Fluid

Figure 36 Transverse Profiles in the Transition Region

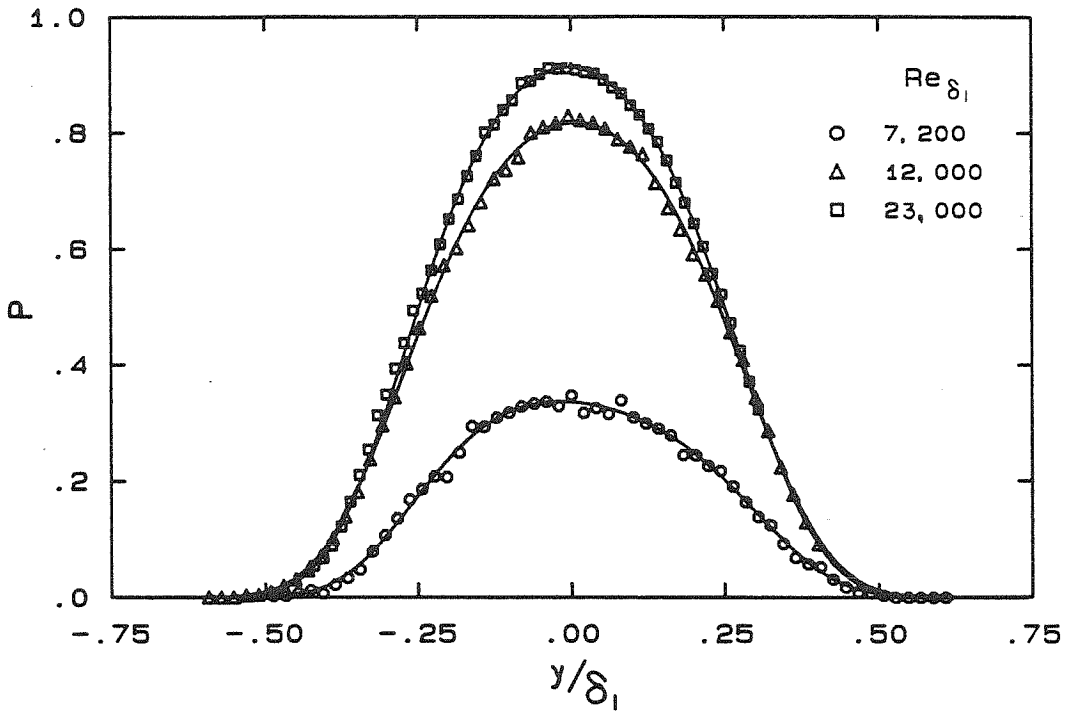

c) Total Mixed Fluid Probability

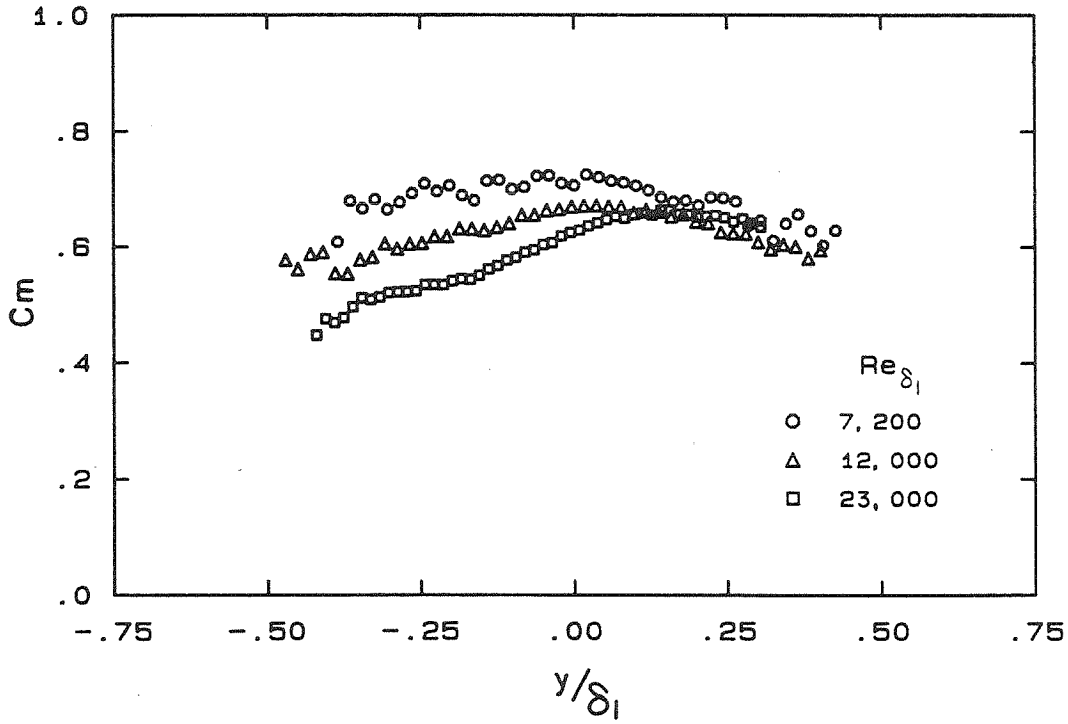

d) Average Mixed Fluid Concentration

Figure 36 Continued

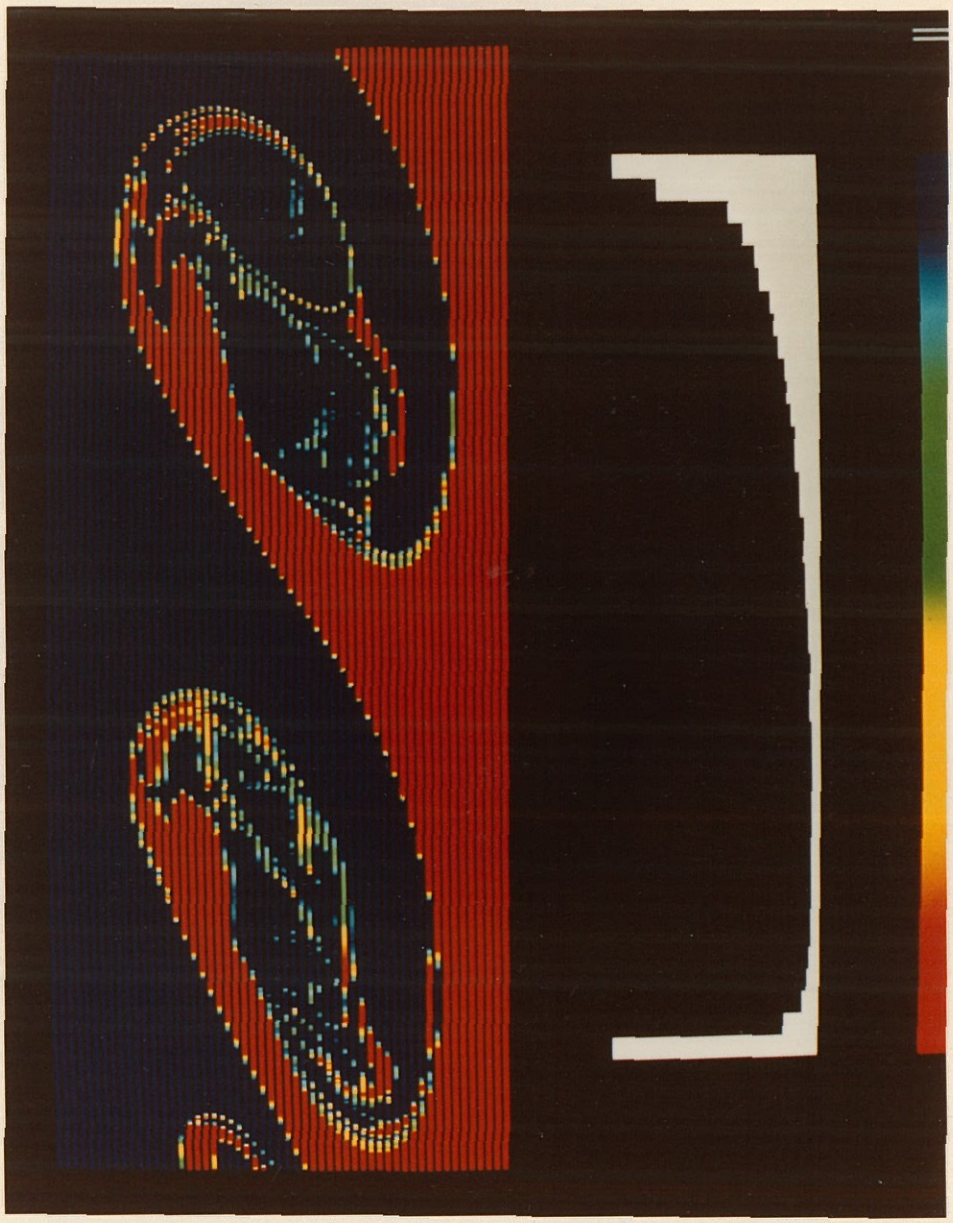

Figure 37a Flow Image in the Transition Region

$Re_{\delta_1} \simeq 7,200$

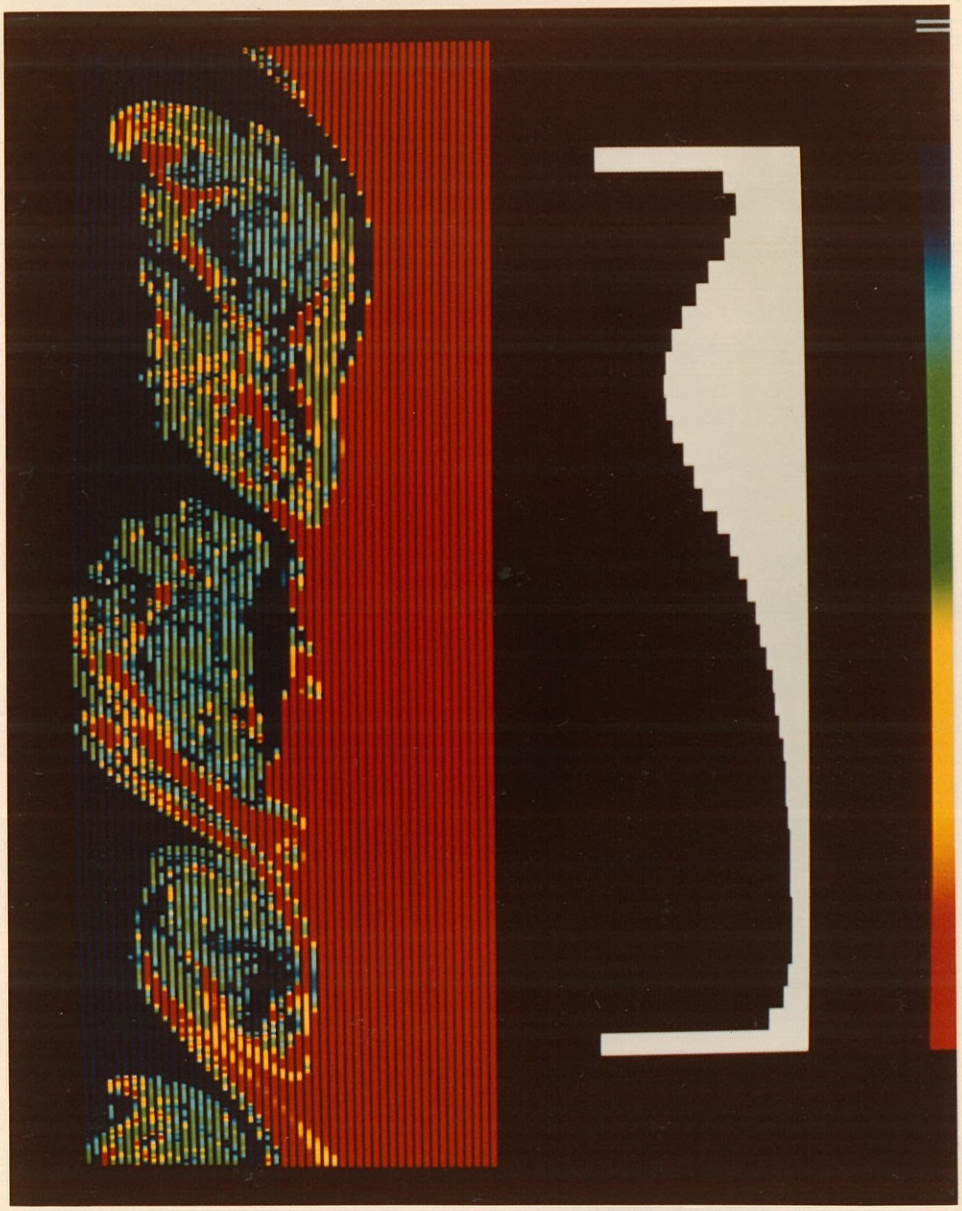

Figure 37b Flow Image in the Transition Region

$Re_{\delta_1} \simeq 12,000$

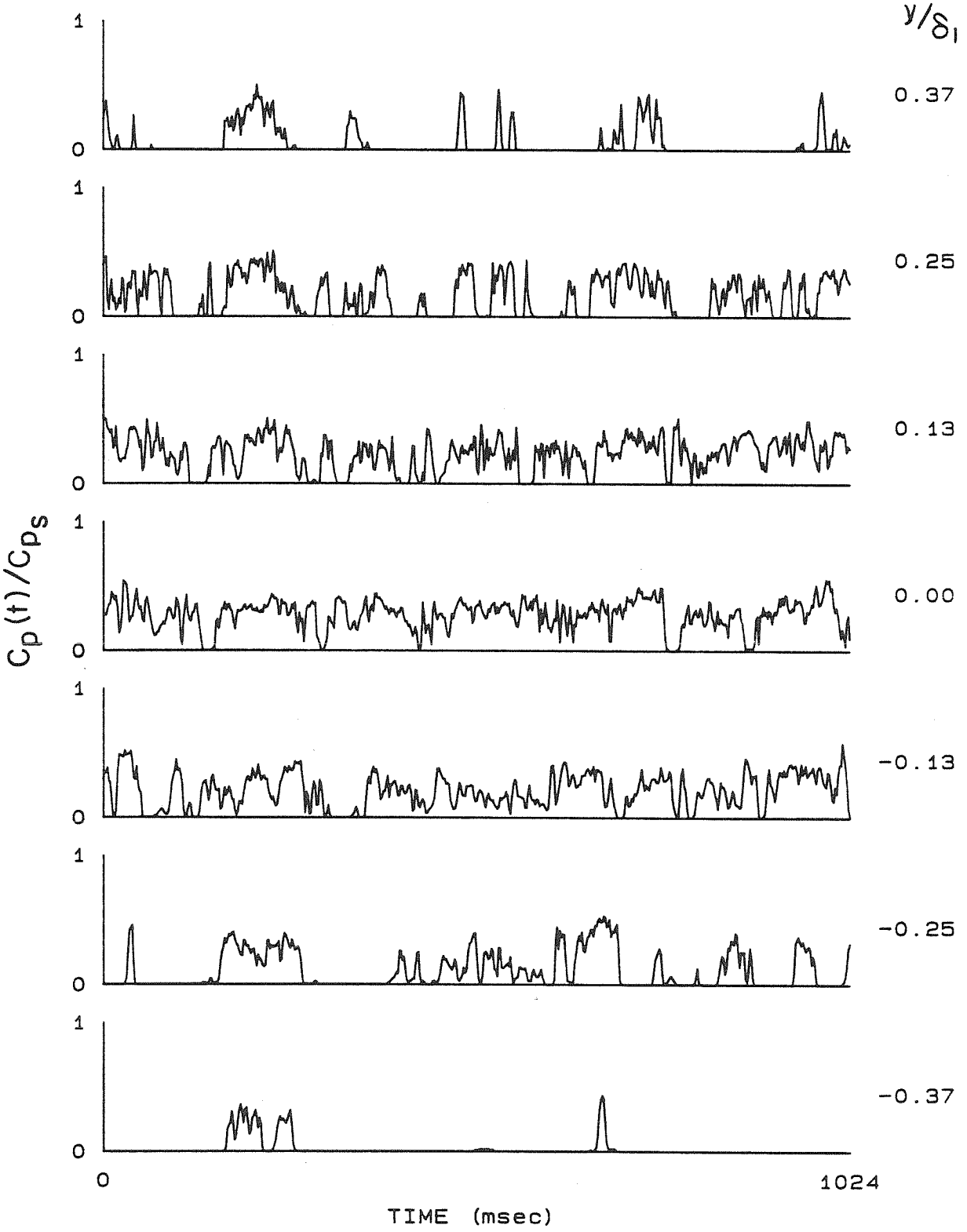

Figure 38 Product Concentration vs Time

$\phi = 1/10$, $r = 0.38$, $Re_{\delta_1} \simeq 22{,}200$

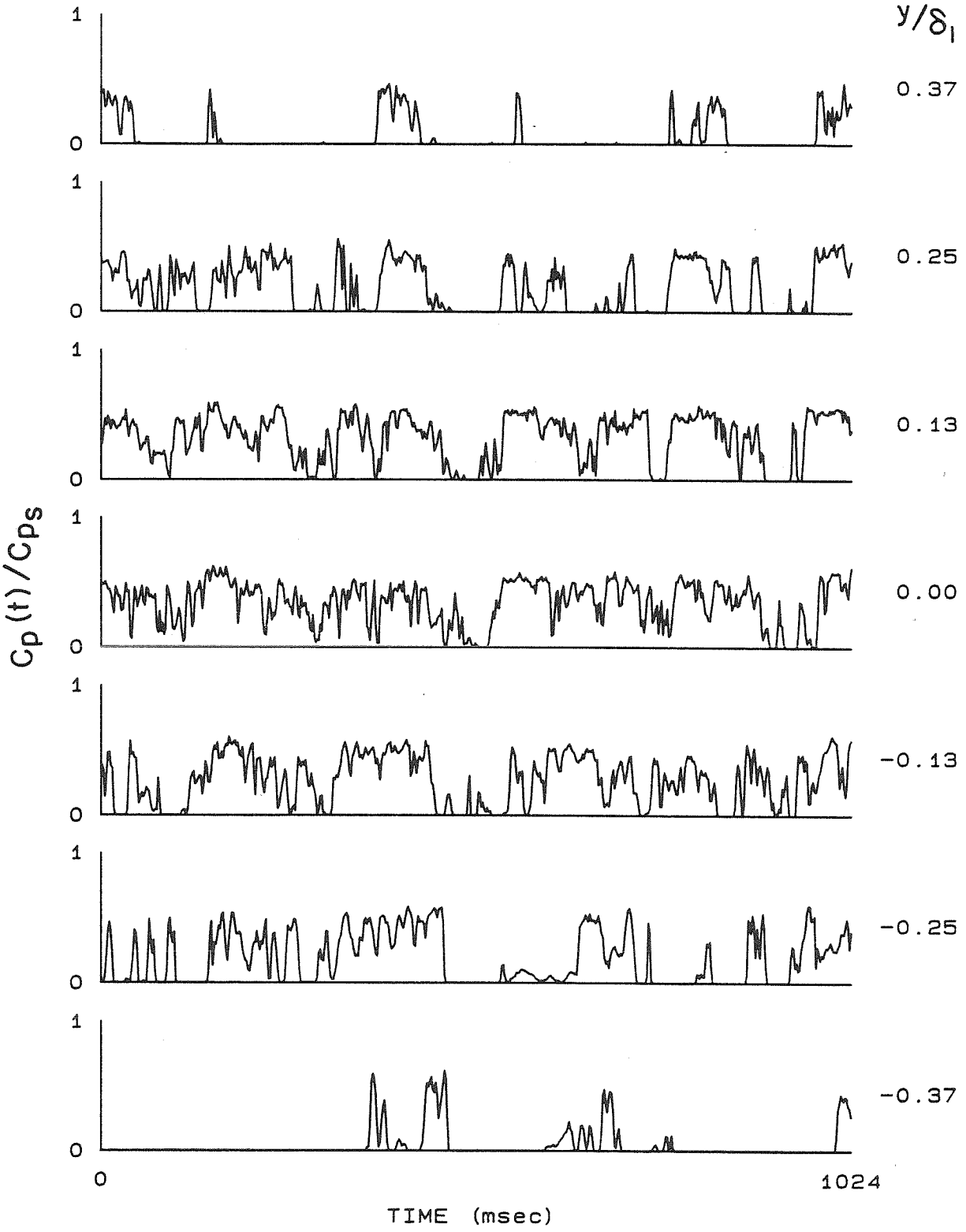

Figure 39 Product Concentration vs Time

$\phi = 10$, $r = 0.38$, $Re_{\delta_1} \simeq 22{,}200$

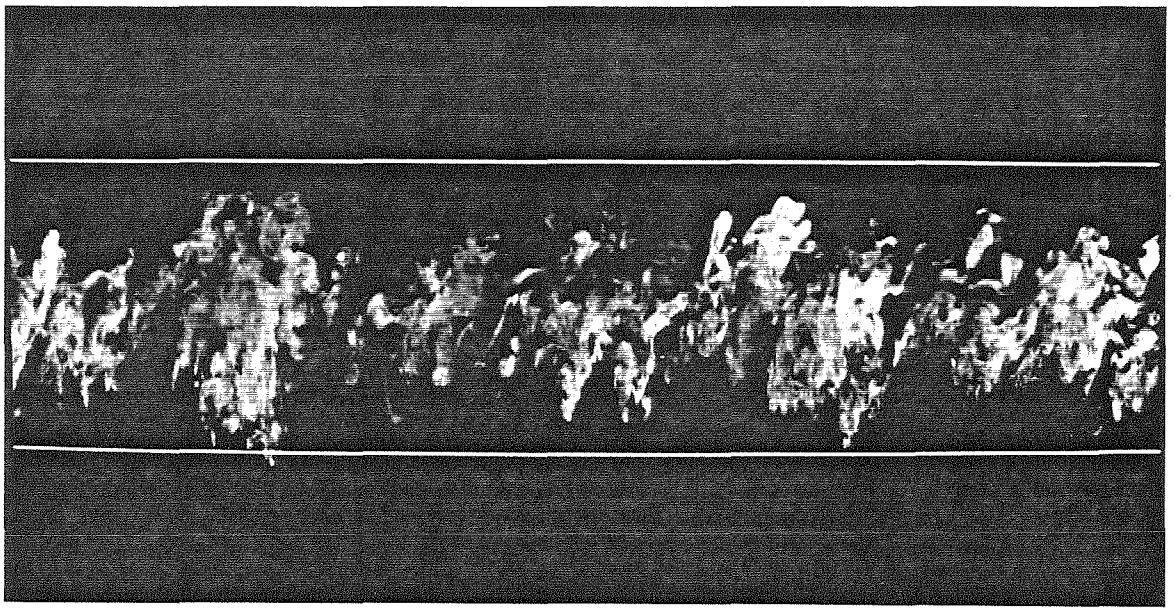

Figure 40a Flow Image of Figure 38, ϕ = 1/10

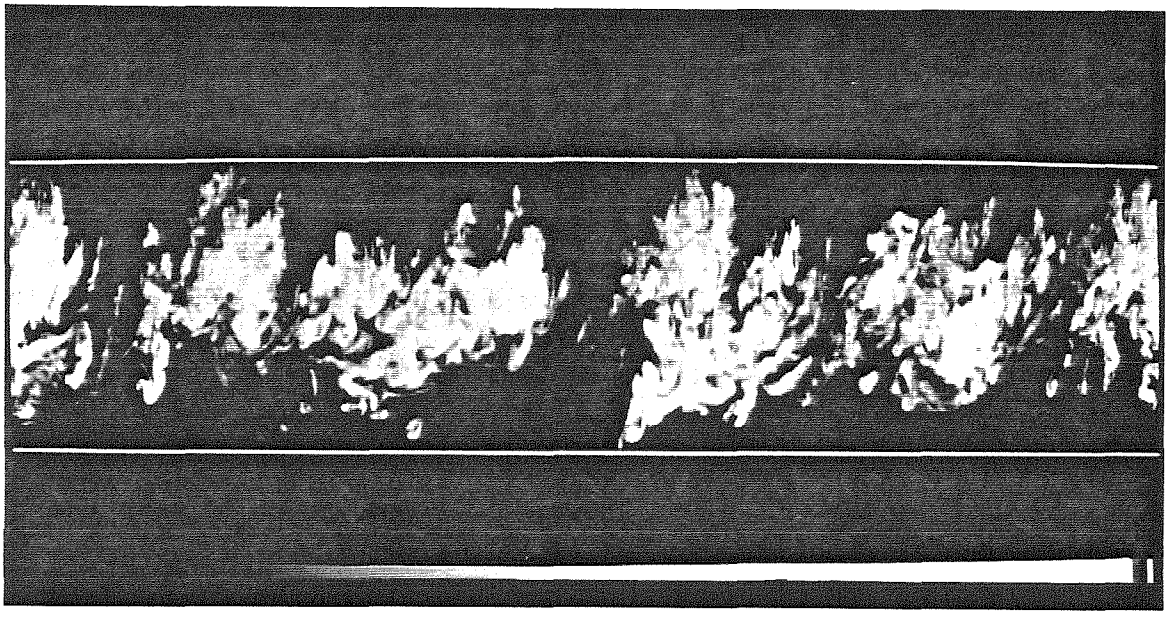

Figure 40b Flow Image of Figure 39, ϕ = 10

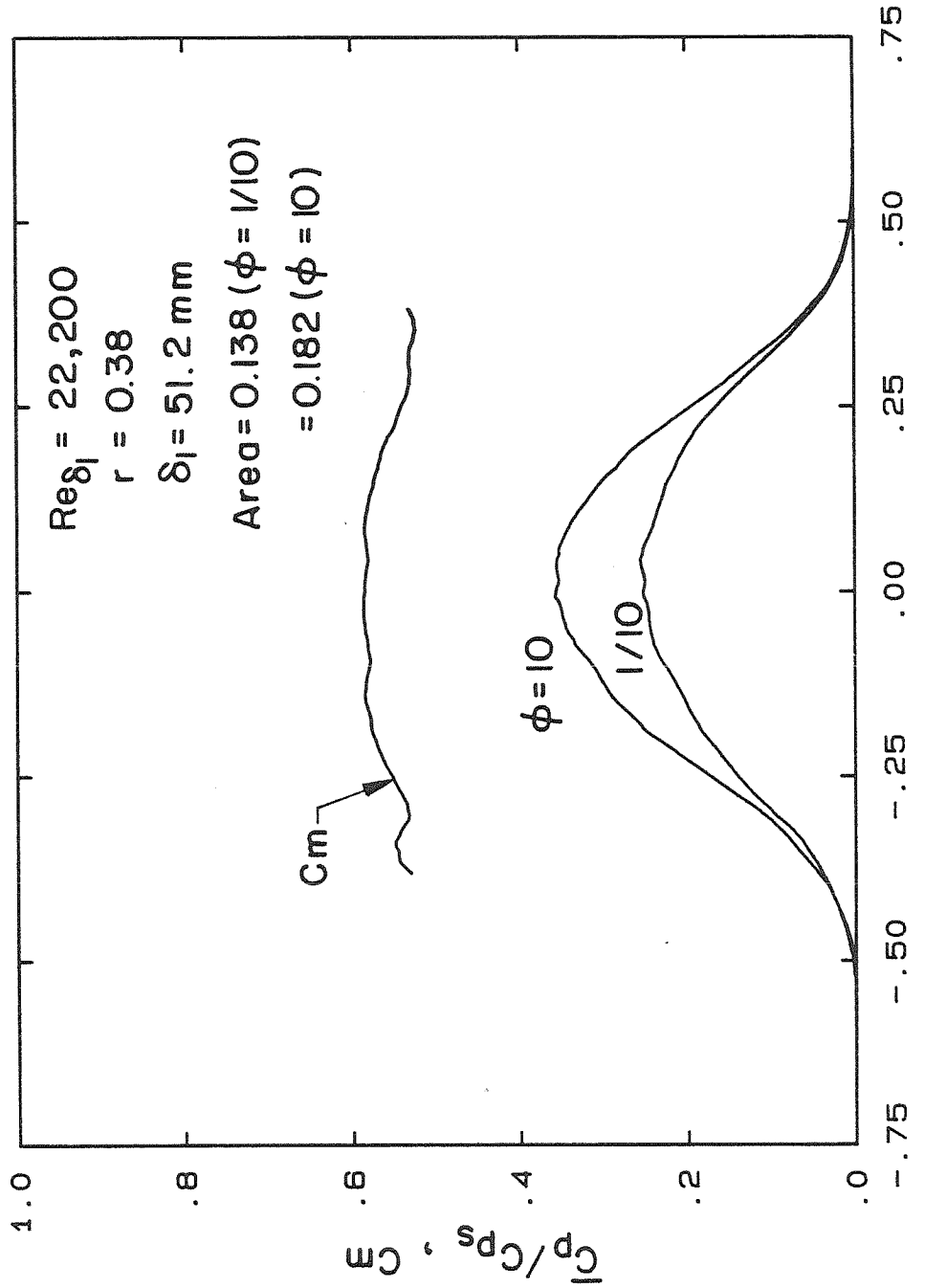

Figure 41 Average Product and Mixed Fluid Concentration Profiles
ϕ = 1/10 & 10, r = 0.38, $Re_{\delta_1} \simeq 22,200$

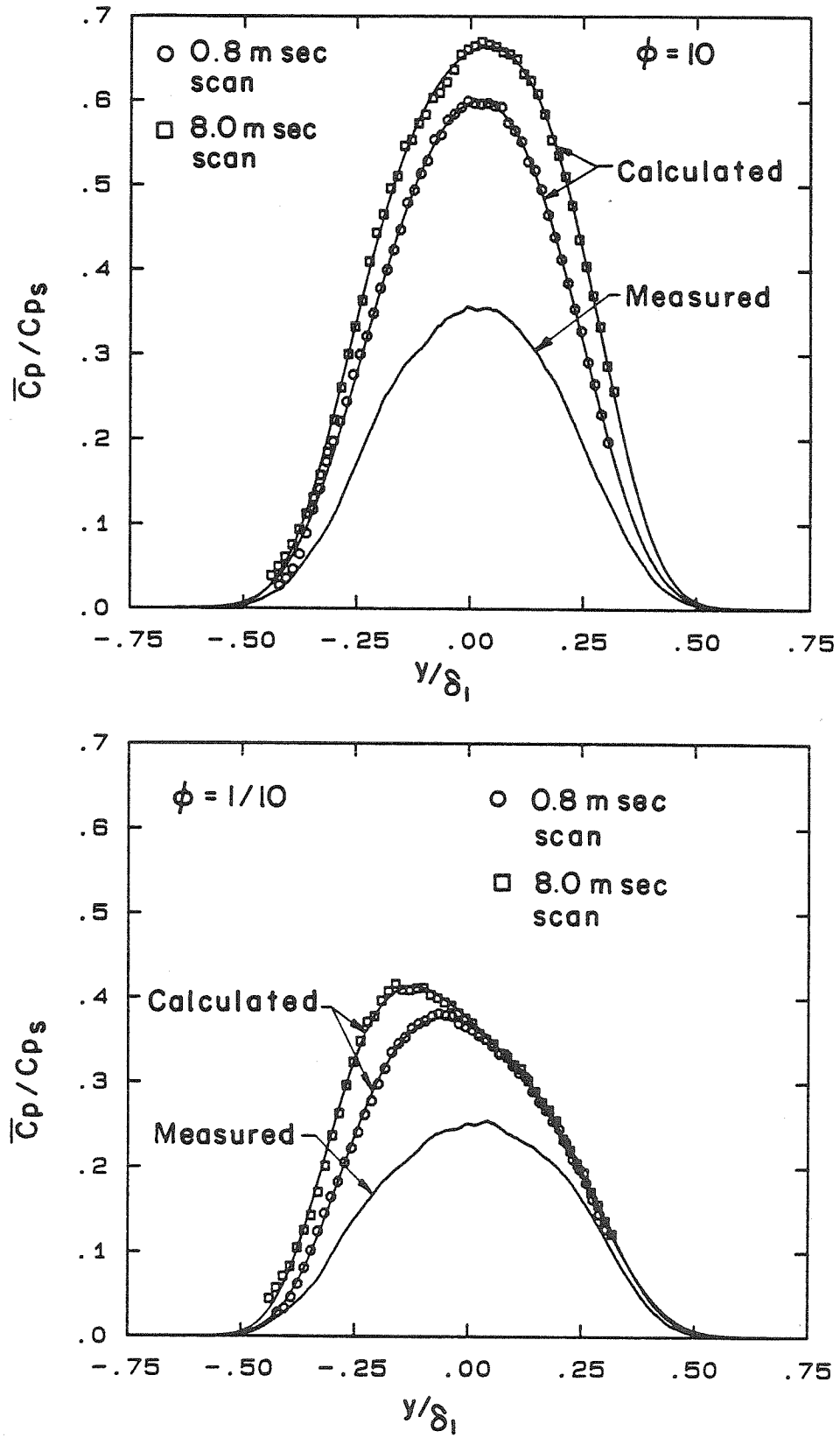

Figure 42 Comparison of Calculated (from Dilution PDFs) and Measured Average Product Concentration Profiles

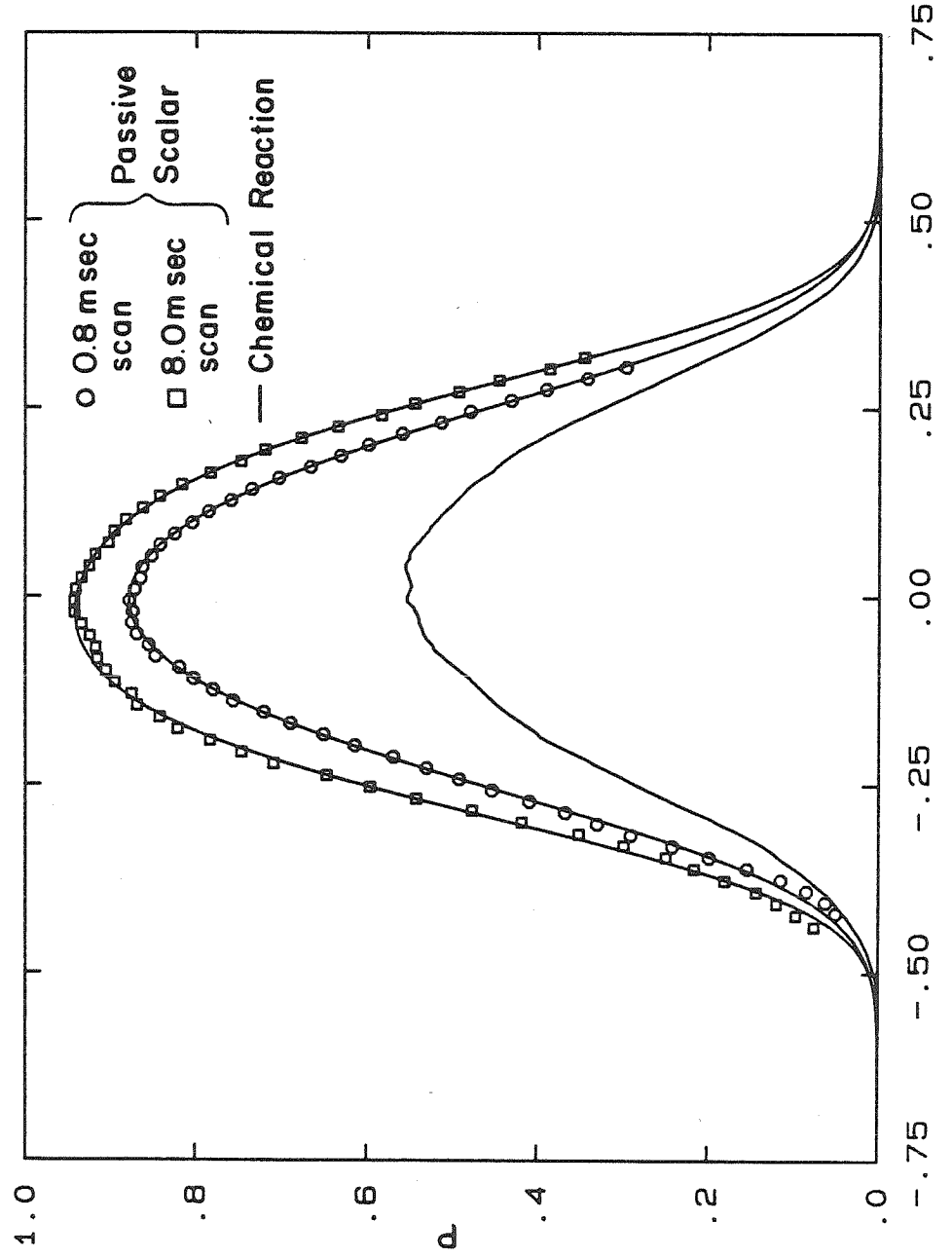

Figure 43 Comparison of Total Mixed Fluid Probability from Chemical Reaction and Dilution

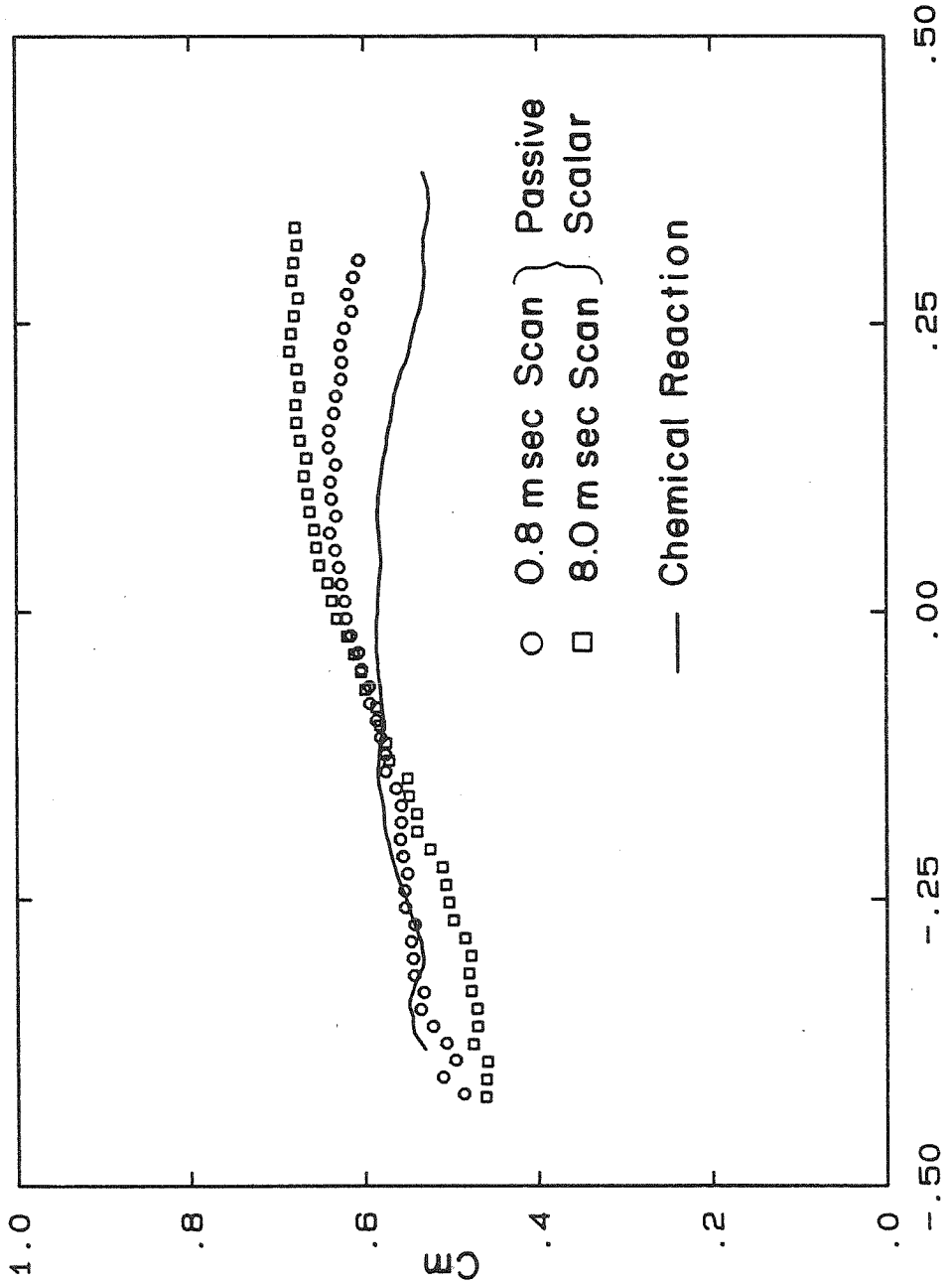

Figure 44 Comparison of Average Mixed Fluid Concentration from Chemical Reaction and Dilution

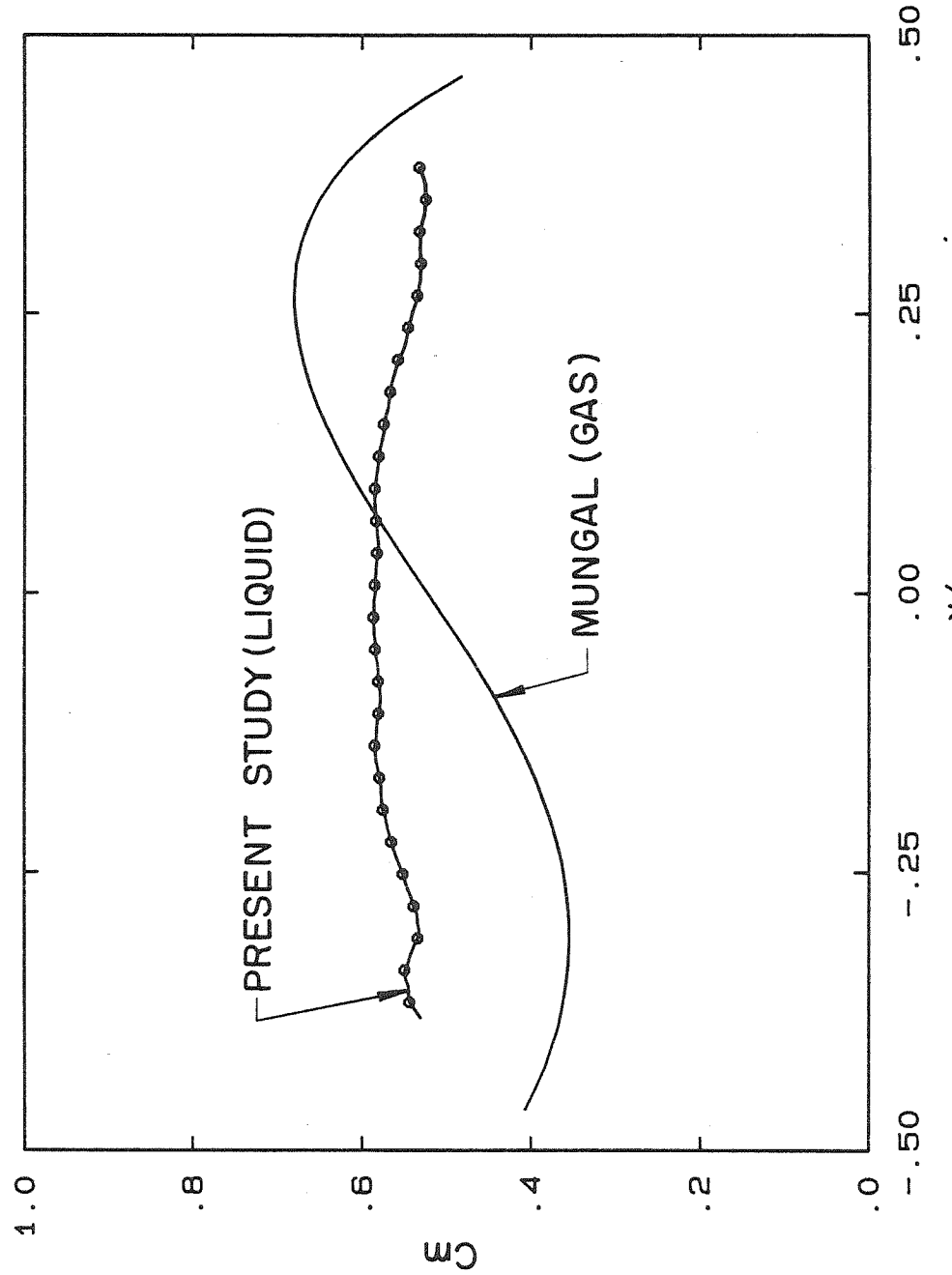

Figure 45 Comparison of Average Mixed Fluid Concentration of Gas and Liquid

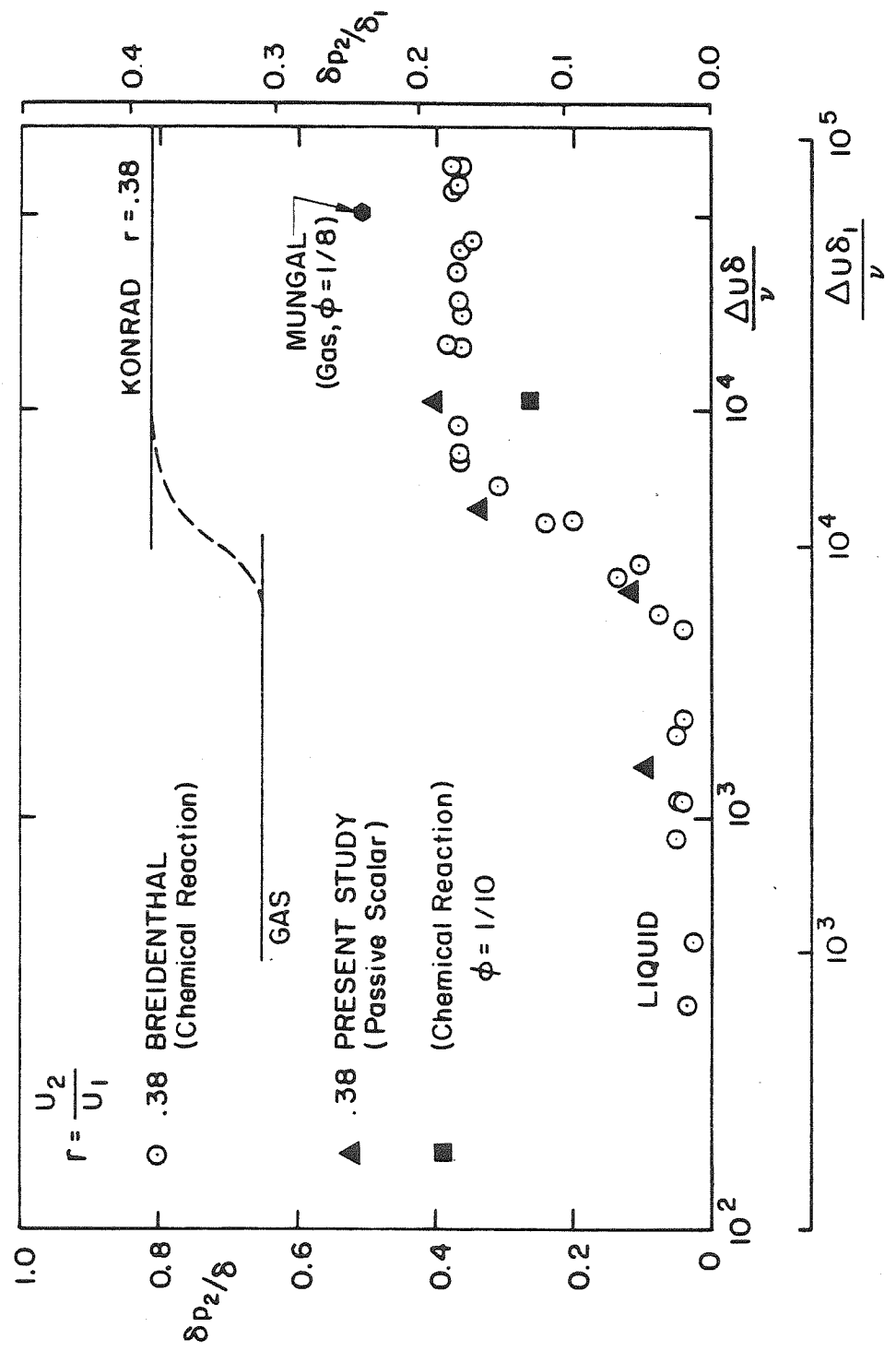

Figure 46 Comparison of Product Thickness with Breidenthal, Konrad and Mungal

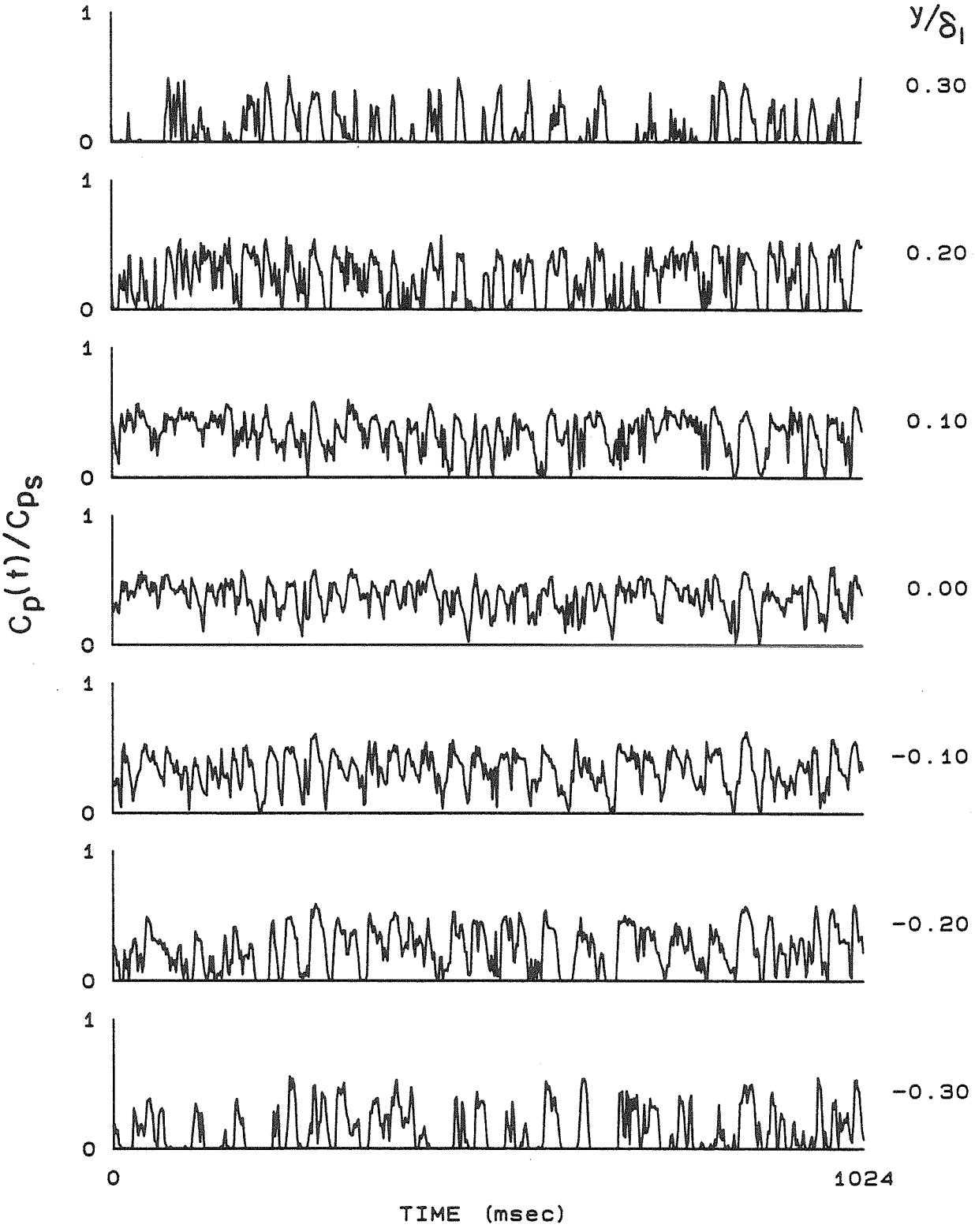

Figure 47 Product Concentration vs Time

$\phi = 10$, $r = 0.38$, $Re_{\delta_1} \simeq 78{,}300$

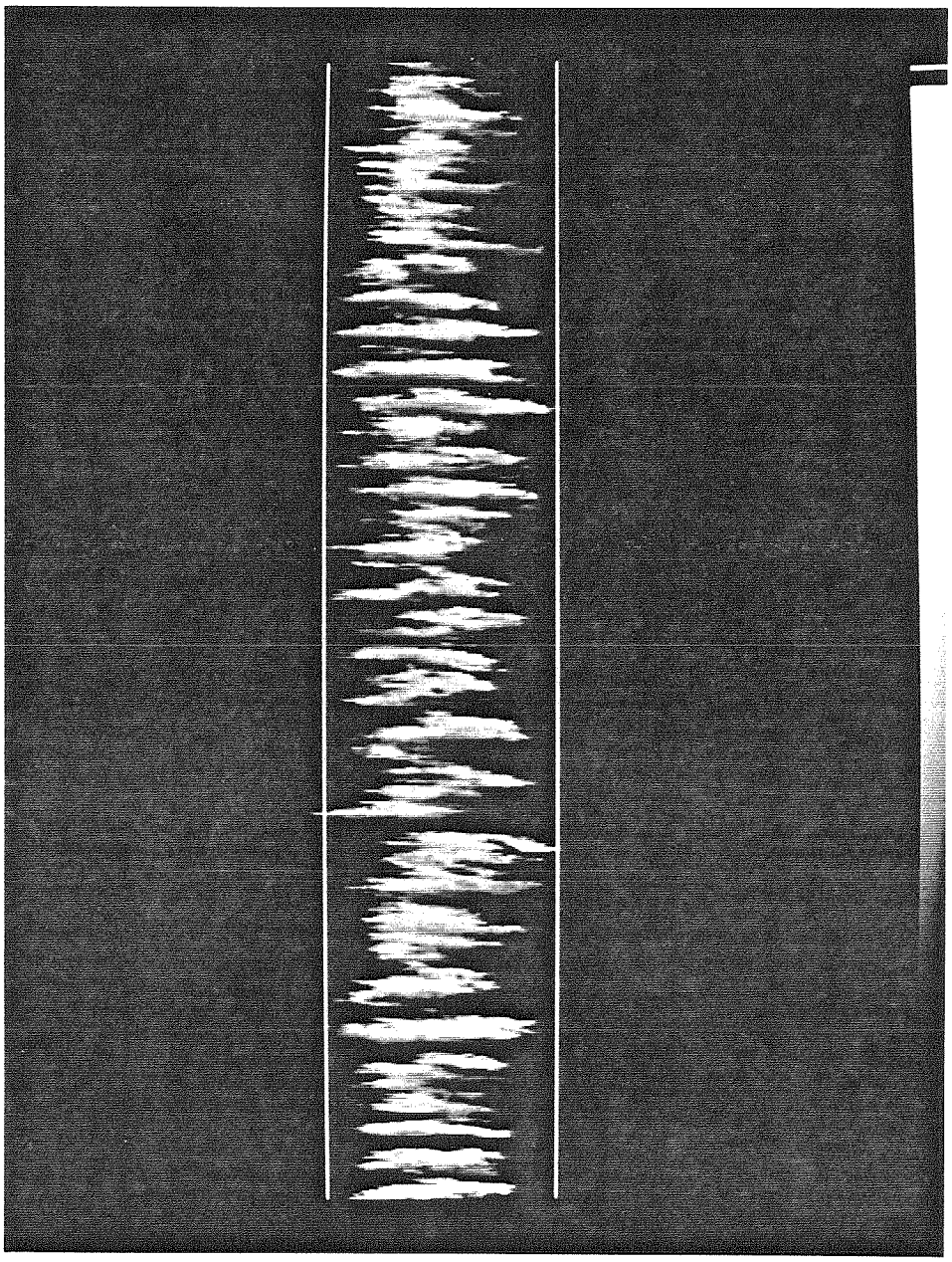

Figure 48 Flow Image of Figure 47

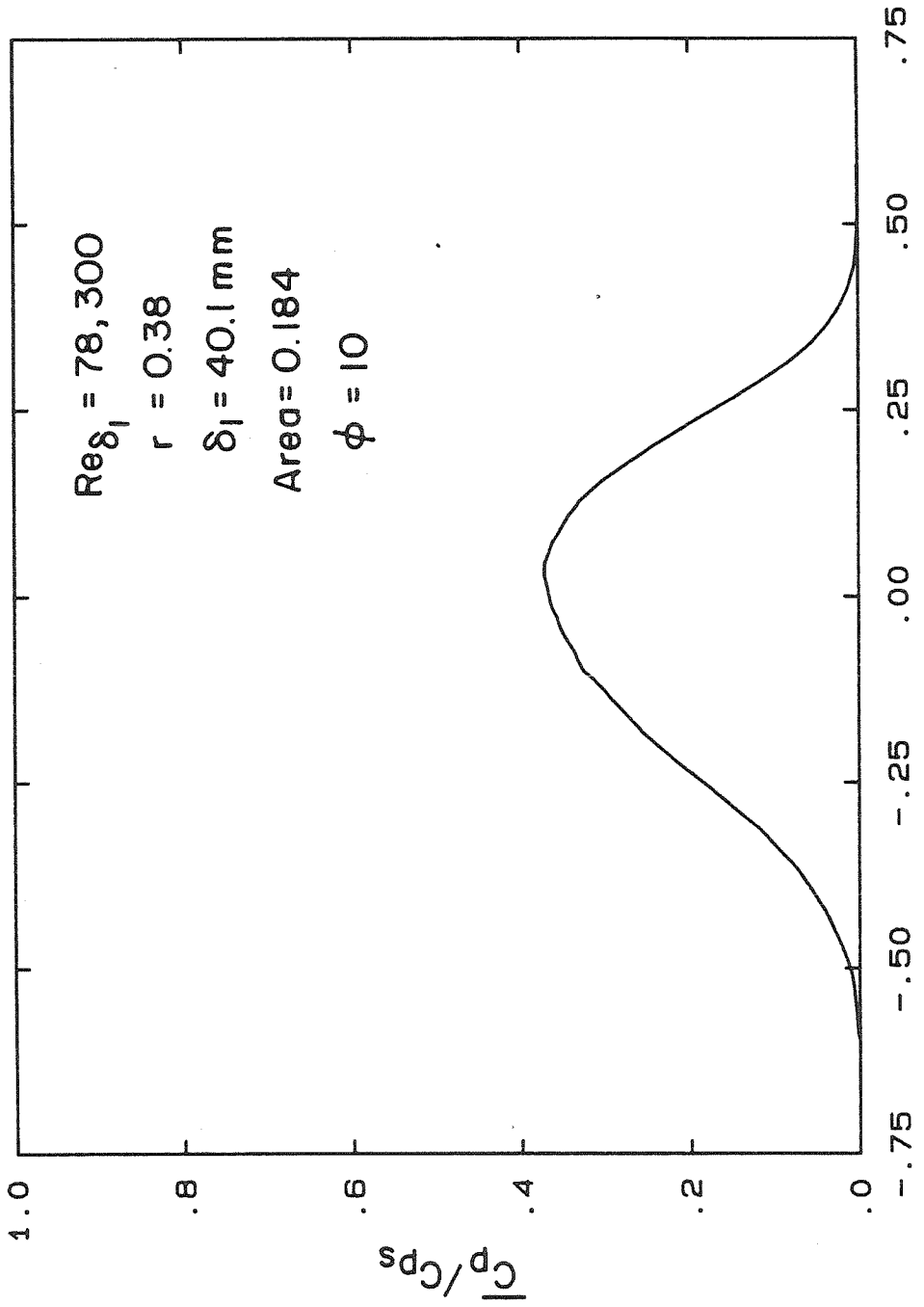

Figure 49 Average Product Concentration Profile, ϕ = 10, r = 0.38, $Re_{\delta_1} \simeq 78,300$

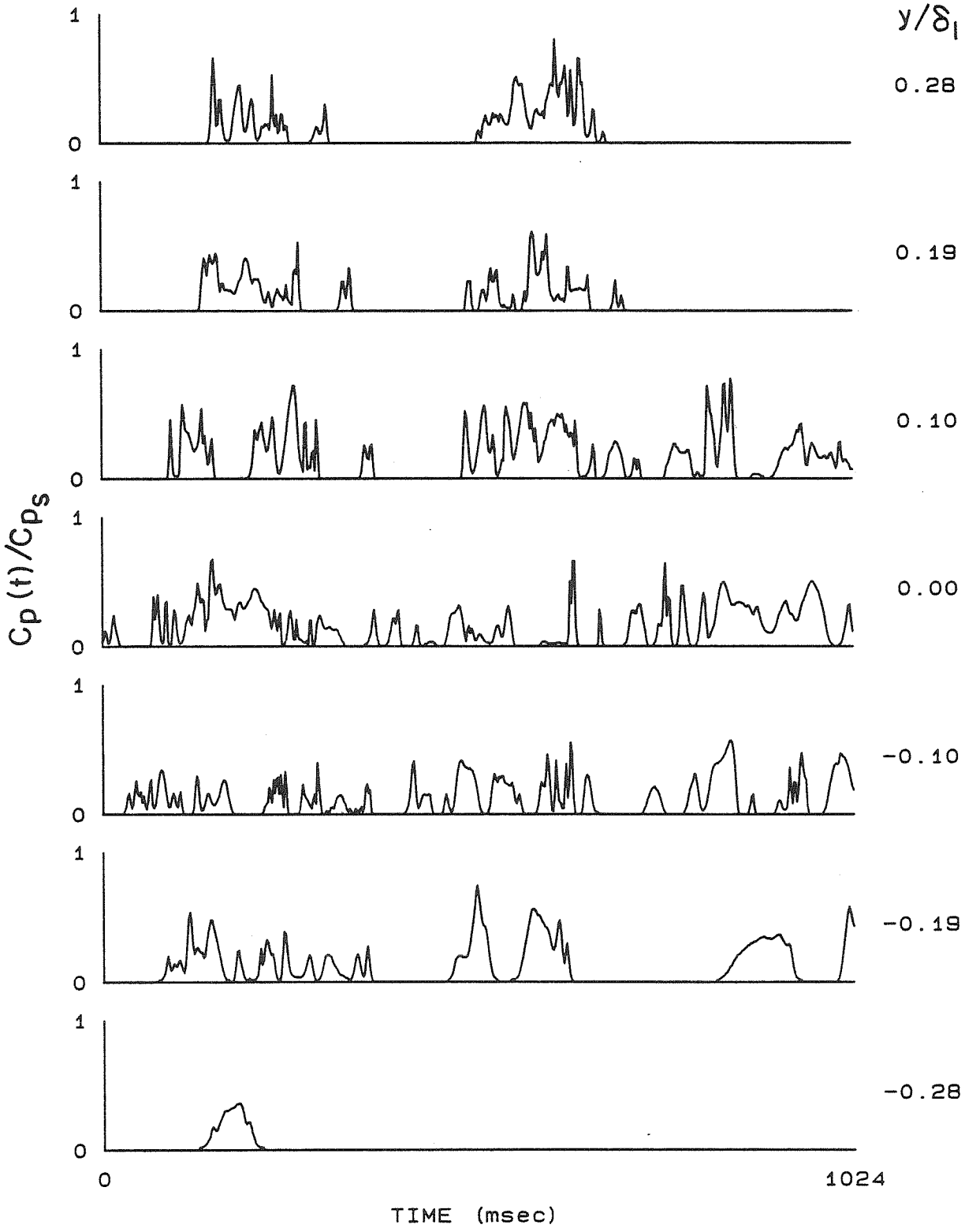

Figure 50 Product Concentration vs Time

$\phi = 1/10$, $r = 0.48$, $Re_{\delta_1} \simeq 3{,}800$

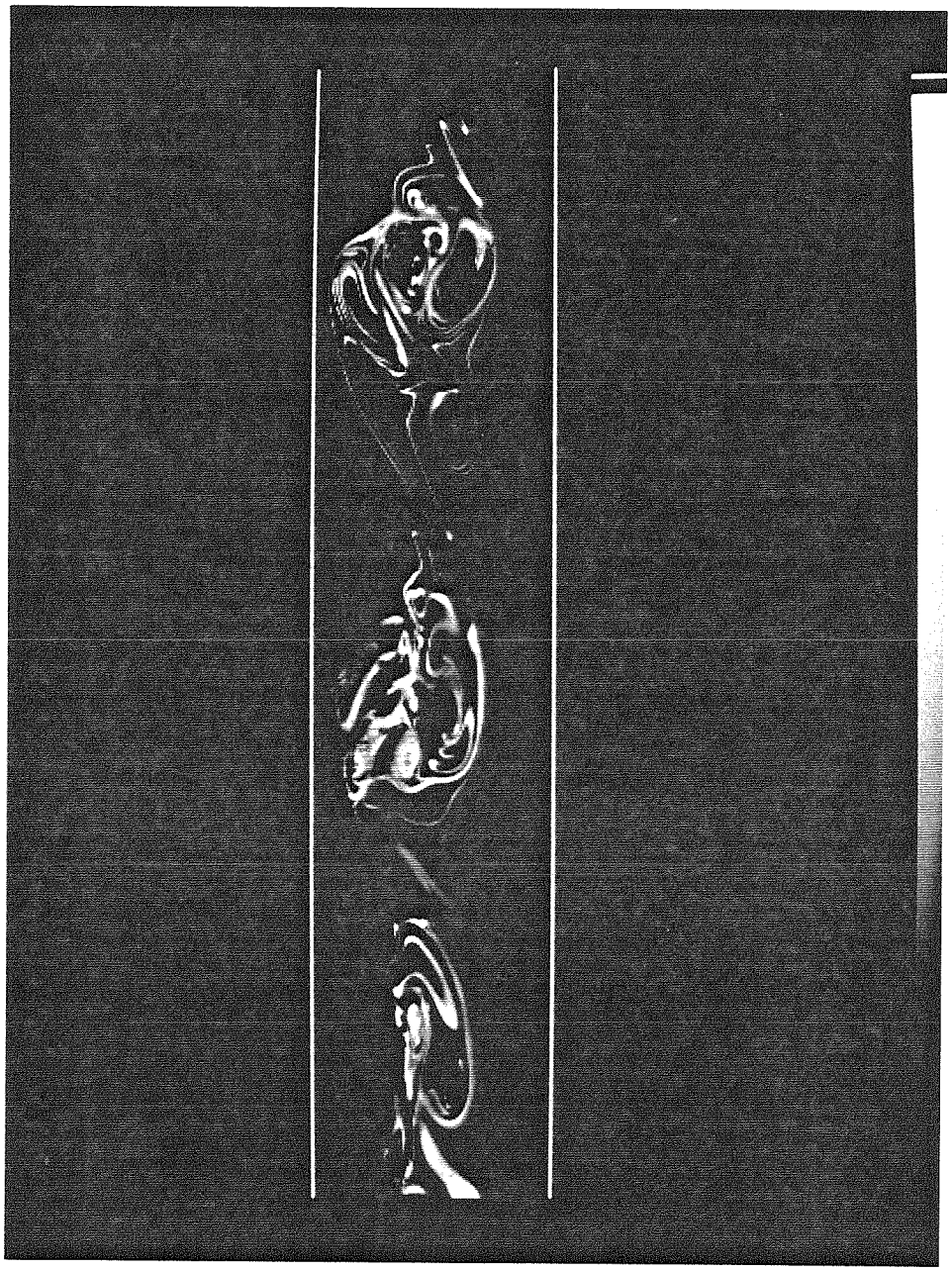

Figure 51 Flow Image of Figure 50

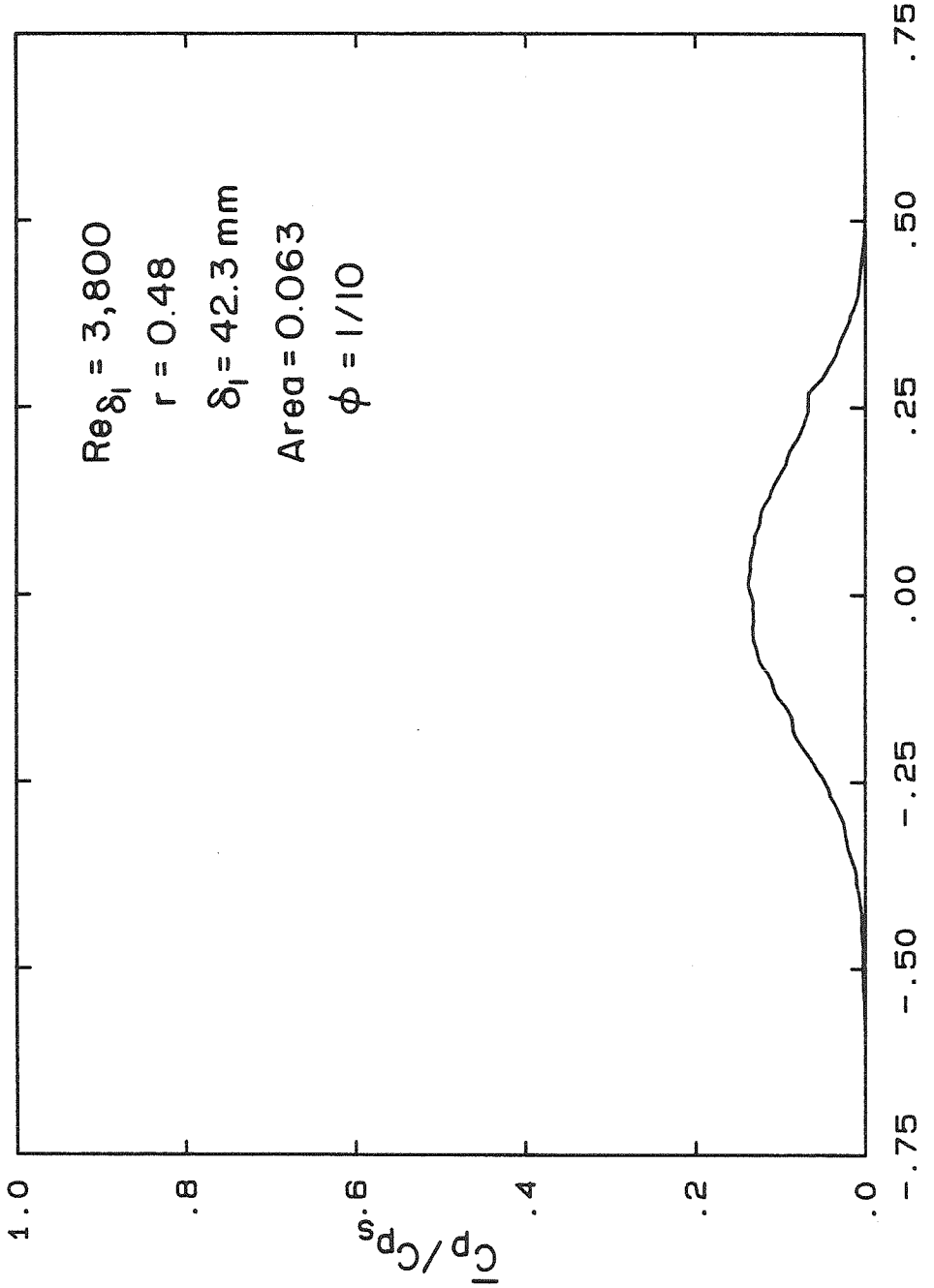

Figure 52 Average Product Concentration Profile, ϕ = 1/10, r = 0.48, $Re_{\delta_1} \simeq 3,800$